Systematic Artifacts in Current-Induced Magnetic Field Measurements by MRI

Gregersen, Frodi

Publication date:
2022

Document Version
Publisher's PDF, also known as Version of record

Doctor of Philosophy

Doctoral Thesis in Biomedical Engineering

DTU Health Tech
Department of Health Technology

Systematic Artifacts in Current-Induced Magnetic Field Measurements by MRI

Fróði Gregersen

DTU

Main supervisor:

Lars G. Hanson, Associate Professor, DTU Health Tech

Co-supervisors:

Axel Thielscher, Professor, DTU Health Tech

Rong Xue, Professor, Institute of Biophysics, University of Chinese Academy of Sciences

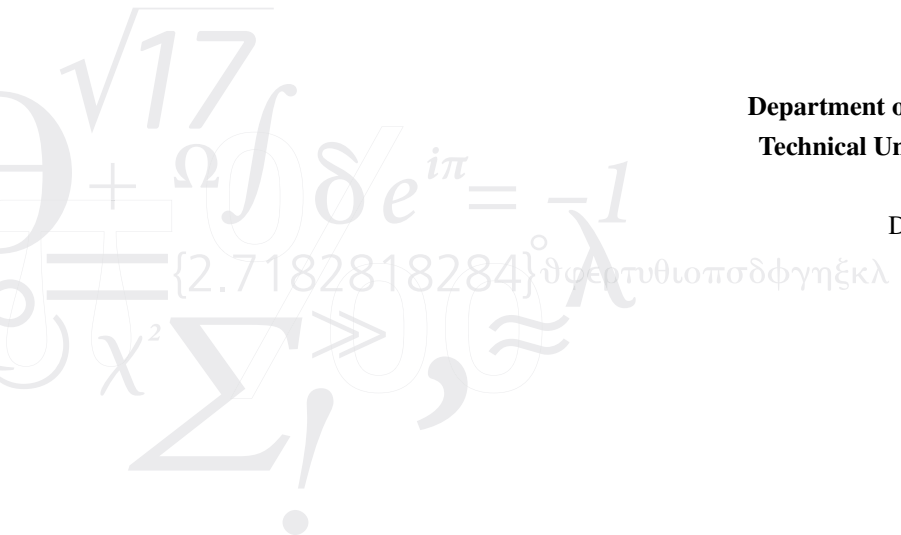

DTU Health Tech
Department of Health Technology
Technical University of Denmark
Ørsteds Plads 345C
DK-2800 Kgs. Lyngby
Denmark

Summary

Computational volume conductor models of the human head are increasingly used in neuroscientific research to estimate induced electric fields in non-invasive brain stimulation methods or for source localization in electro- and magnetoencephalography. However, the anatomical complexity of the human head makes accurate head modeling challenging. To create reliable head models it is important to validate their accuracy.

A good candidate for non-invasive validation is magnetic resonance current density imaging (MRCDI). MRCDI measures small perturbations of the phase caused by the magnetic field from injected currents. MRCDI methods that are sensitive enough to detect injected current as low a 1 mA in the human brain have recently been demonstrated.

The work presented in this thesis aimed at reducing systematic artifacts in MRCDI. Magnetic stray fields from the currents in the lead wires are detrimental in MRCDI. Although lead stray fields can be corrected, residual errors can still influence the data if the leads are too close to the brain. Due to safety risks when highly conductive materials are used in the MR scanner, strict guidelines for lead wire positioning have to be followed, making commercial leads impractical for MRCDI. To circumvent the impractical safety guidelines, new low-conductivity lead wires optimal for MRCDI were constructed and a safety study was performed using RF simulations and temperate measurements.

The second aim was to reduce physiological noise in MRCDI. Although the MR sequences used in human in-vivo MRCDI up to now have demonstrated good sensitivity to current-induced magnetic fields, low-frequency spatial noise patterns arising from physiological noise in the measurements have been prevalent in the measured magnetic fields.

Echo planar imaging (EPI), the fastest MR imaging method, was used to increase robustness to physiological noise. Physiological noise in MRCDI measurements acquired with EPI was analyzed and further physiological noise reduction was attempted with physiological noise correction techniques. However, due to the robustness of EPI-based MRCDI, physiological noise correction had a negligible impact.

Resumé

Computermodeller af det menneskelige hoved bruges i stigende grad i neurovidenskabelig forskning til at estimere inducerede elektriske felter i hjernestimuleringsmetoder eller til kildelokalisering i elektro- og magnetoencefalografi. Kompleksitetnen af det menneskelige hoveds anatomi gør nøjagtig hovedmodellering udfordrende. For at skabe pålidelige hovedmodeller er det vigtigt at validere deres nøjagtighed.
En god kandidat til validering er magnetisk resonans strømtæthedsbilleddannelse (MR-CDI). MRCDI måler små ændringer af fasen forårsaget af magnetfeltet fra inducerede strømme. MRCDI metoder, der er følsomme nok til at detektere inducerede strømme så lave som 1 mA i den menneskelige hjerne, er for nylig blevet demonstreret.
Formålet med denne afhandling var at reducere systematiske artefakter i MRCDI. Magnetiske felter fra strømmene i elektroderne påvirker MRCDI målingerne. Selvom felterne fra elektroderne kan rettes, kan resterende fejl stadig påvirke målingerne, hvis elektroderne er for tæt på hjernen. På grund af sikkerhedsrisici når stærkt ledende materialer bruges i MR scanneren, skal strenge retningslinjer for placering af ledningerne følges, hvilket gør kommercielle ledninger upraktiske for MRCDI. For at omgå de upraktiske sikkerhedsretningslinjer blev der konstrueret nye elektroder med lav ledningsevne, der var optimale til MRCDI, og en undersøgelse af sikkerheden blev udført ved brug af RF simuleringer og temperatur målinger.
Det andet mål var at reducere fysiologisk støj i MRCDI. Selvom de MR-sekvenser, der hidtil har været anvendt til MRCDI af menneskehjerner, har vist god følsomhed over for strøminducerede magnetfelter, har rumlige lavfrekvente støjmønstre, der skyldes fysiologisk støj i målingerne, været betydelige i de målte magnetfelter.
Echo planar imaging (EPI), som er den hurtigste MR billeddannelsesmetode, blev brugt til at øge robustheden over for fysiologisk støj. Fysiologisk støj i EPI-baserede MRCDI målinger blev analyseret, og yderligere fysiologisk støjreduktion blev forsøgt

med fysiologiske støjkorrektionsteknikker. På grund af robustheden af EPI-baseret MRCDI havde fysiologisk støjkorrektion ubetydelig påvirkning.

Preface

This thesis is submitted to the PhD school at the department of Health Technology at the Technical University of Denmark (DTU) in partial fulfillment of the requirement for obtaining a PhD degree. The project was supervised by associate professor Lars G. Hanson (DTU Health Tech) and co-supervised by professor Axel Thielscher (DTU Health Tech) and Rong Xue from the Institute of Biophysics (IBP) at the Chinese Academy of Sciences (CAS) in Beijing. The thesis contains research conducted during my employment at DTU from 1st of September 2018 to 30th of September 2021. The research took place at DTU and at the Danish Research Center for Magnetic Resonance (DRCMR) as well as one external research stay at CAS during the fall of 2019.

During the stay in Beijing teaching requirements were fulfilled at the Sino-Danish Center for Education and Research in the course Fundamental Biomedical Signal Processing. Teaching assistant work was also carried out in the course Medical Magnetic Resonance Imaging (22506) at DTU in spring 2019 and spring 2020.

The PhD study was funded by the Sino-Danish Center for Education and Research, DTU and indirectly through access to equipment at DRCMR.

Fróði Gregersen

Kongens Lyngby, 30th September 2021

Acknowledgements

I would like to express my gratitude to my supervisor Lars Hanson and co-supervisor Axel Thielscher, for their help and guidance and the invaluable scientific discussions. It has been a pleasure being supervised by you. I would also like to thank the rest of the MRCDI group for making the work so enjoyable.
Next, I would like to thank my co-supervisor Xue Rong, for her help and guidance during my external research stay in Beijing. And thank you Zuo Zhentao, for always being ready to help when I needed assistance with experiments at IBP.
I would also like to thank all my colleagues at DTU and DRCMR for making my last three years an enjoyable experience. And to my colleagues at IBP and SDC that I met in Beijing, thank you for making my external research stay a memorable time.
In addition, I would like to thank my family for their endless love and support. Without you, I would not have been where I am today. And last but not least, thank you Liz for your tremendous patient, support, and understanding during my thesis writing period.

Contributions

JOURNAL PAPERS

- Gregersen, Fróði; Eroğlu, Hasan H; Göksu, Cihan; Puonti, Oula; Xue, Rong; Thielscher, Axel; Hanson, Lars G. **Noise reduction in human in-vivo magnetic resonance current density (MRCDI) imaging using echo planar imaging.** *Manuscript in preparation, 2021*

- Gregersen, Fróði; Göksu, Cihan; Schaefers, Gregor; Xue, Rong; Thielscher, Axel; Hanson, Lars G. **Safety evaluation of a new setup for transcranial electric stimulation during magnetic resonance imaging.** *Published in Brain Stimulation, 2021*

CONFERENCE ABSTRACT

- Gregersen, Fróði; Göksu, Cihan; Schaefers, Gregor; Xue, Rong; Thielscher, Axel; Hanson, Lars G. **Safety evaluation with respect to RF-induced heating of a new setup for transcranial electric stimulation during MRI.** *Presented at ISMRM & SMRT Annual Meeting & Exhibition, 2021*

CO-AUTHORED JOURNAL PAPERS

- Göksu, Cihan; Scheffler, Klaus; Gregersen, Fróði; Eroğlu, Hasan H; Heule, Rahel; Siebner, Hartwig R; Hanson, Lars G; Thielscher, Axel. **Sensitivity and resolution improvement for in vivo magnetic resonance current-density imaging of the human brain.** *Published in Magnetic Resonance in Medicine, 2021*

- Eroğlu, Hasan H; Puonti, Oula; Göksu, Cihan; Gregersen, Fróði; Siebner, Hartwig R; Hanson, Lars G; Thielscher, Axel. **On the reconstruction of magnetic resonance current density images of the human brain: Pitfalls and perspectives.** *Published in NeuroImage, 2021*

CO-AUTHORED CONFERENCE ABSTRACTS

- Göksu, Cihan; Scheffler, Klaus; Gregersen, Fróði; Eroğlu, Hasan H; Heule, Rahel; Siebner, Hartwig R; Hanson, Lars G; Thielscher, Axel; **Sensitivity and resolution improvement for in-vivo magnetic resonance current density imaging (MRCDI) of the human brain.** *Presented at ISMRM & SMRT Annual Meeting & Exhibition, 2021*

- Göksu, Cihan; Hanson, Lars G; Gregersen, Fróði; Scheffler, Klaus; Thielscher, Axel; **Acquisition-weighted MR Current Density Imaging (AW-MRCDI) improves sensitivity and spatial resolution.** *presented at ISMRM & SMRT Virtual Conference & Exhibition, 2020*

Abbreviations

BOLD	Blood-Oxygenation-Level-Dependent
EEG	Electroencephalography
EIT	Electrical Impedance Tomography
EPI	Echo Planar Imaging
fMRI	Functional Magnetic Resonance Imaging
GRE	Gradient Echo
MGRE	Multi-Echo Gradient Echo
ICNE	Injection Current Nonlinear Encoding
MB	Multi-Band
MEG	Magnetoencephalography
MR	Magnetic Resonance
MRCDI	Magnetic Resonance Current Density Imaging
MREIT	Magnetic Resonance Electrical Impedance Tomography
MRI	Magnetic Resonance Imaging
RF	Radio Frequency
SE	Spin Echo
SFNR	Signal-to-Fluctuation-Noise Ratio

SNR	Signal-to-Noise Ratio
tDCS	Transcranial Direct Current Stimulation
TES	Transcranial Electric Stimulation

Contents

CHAPTER 1
Introduction

1.1 Motivation

Transcranial electrical stimulation (TES) has grown in popularity since the seminal paper by Nitsche and Paulus [1] in 2000 showed that weak injected currents can increase the excitability of cortical neurons underlying the scalp electrodes. The interest is both in using it as a neuroscientific tool to study brain function and cognition as well as a diagnostic tool for various brain disorders [2]. However, the reliability of the technique has been questioned as systematic reviews have shown the lack of reproducibility of the physiological effect [3] and questioned the ability to localize brain function without guided stimulation strategies [4]. The complex anatomy of the human head calls for numerical methods to estimate the electric field induced by the applied currents. Head models can be created from MRI scans and used for subject-specific electric field calculations [5]. However, it has been shown that the uncertainty of tissue conductivities impedes the accuracy of the electric field estimates for TES [6]. Gaining knowledge about tissue conductivities is therefore necessary to improve target localization and dose control with computational head modeling.

Apart from being beneficial for neurostimulation methods such as TES and transcranial magnetic stimulation (TMS), computational head models can also benefit source localization in electroencephalography (EEG) and magnetoencephalography (MEG). Tissue conductivities can be obtained using electrical impedance tomography (EIT) [7]. In EIT, currents are injected via surface electrodes, and conductivity images are reconstructed from voltage measurements on the surface. However, EIT suffers from low resolution, spatially varying imaging quality, and poor quantification, especially for structures further away from the electrodes. In 1989, Joy et al. [8] used MRI to measure magnetic flux density caused by injected currents and reconstructed the current density. The technique is called magnetic resonance current density imag-

ing (MRCDI). Shortly after, Zhang [9] proposed to use MRCDI to reconstruct tissue conductivities, giving rise to the technique called magnetic resonance electrical impedance tomography (MREIT). MREIT improves the poor image quality observed in EIT by using current-induced magnetic field measurements or reconstructed current densities obtained from inside the object. It can be considered a dual-modality technique as it needs both the current-induced magnetic field measurements and the surface voltage measurements to quantify the tissue conductivities. Without the voltage measurements, it can only provide a conductivity contrast. The MR acquisition theory and methods for MRCDI and MREIT are identical and discussed in more detail in chapter 2. For simplicity, when discussing MR acquisition theory and methods in this thesis, the current-induced magnetic field measurements will be referred to as MRCDI, while MREIT is reserved for discussions on conductivity reconstruction algorithms.

Apart from providing tissue conductivities for computational head models MRCDI and MREIT also have other potentially useful applications. Since pathological tissue can have electrical tissue properties different from surrounding healthy tissue, MREIT can be used to diagnose and monitor treatment of, for example, tumors [10]. It can also be used to assess the electric fields and conductivity changes during electroporation [11]. A recent study investigated the possibility of using MREIT to directly measure neuronal activity, using the fact that the low-frequency impedance changes when neurons fire [12].

1.2 Pulse sequences for MRCDI

The main objective of MR sequence design for MRCDI is to improve the phase sensitivity to enable the detection of small current-induced magnetic field changes, while simultaneously maintaining a high SNR. This is especially important for human in-vivo brain MRCDI, where only very small current strengths can be safely and comfortably applied. The MRCDI theory is discussed in more detail in chapter 2. Here, an overview will be given of the sequences that have been used for MRCDI up till now. Although MRCDI has been attempted with injected currents at the 100 Hz to

1 kHz range and at the excitation frequency of the MR system, the focus will only be on the more popular MRCDI method using sub 20 Hz frequencies, as this is the frequency relevant for computational head models used for TES. This is not an exhaustive review of MRCDI and MREIT history, but rather an overview of the sequence development during the past 3 decades that has been crucial to render human in-vivo brain MRCDI possible. The order is not strictly chronological but rather grouped into sequence types.

Most of the early MRCDI studies, including the first study by Joy et al. [8], used a spin-echo (SE) sequence where the currents were injected before and after the spin refocusing pulse followed by a readout period with no current injection. Scott et al. [13] studied the sensitivity of the SE sequence to current-induced phase changes. They considered both the shorter current injection in between RF excitation and readout as well as an extended period where currents are applied during readout as well. They demonstrated that there is a trade-off between reducing random noise or systematic errors. Random noise dominates for small currents and/or short application times (small current-time product), while a large current-time product results in systematic artifacts.

In 2007, Park et al. [14] invented the injection current nonlinear encoding (ICNE) method, which allowed for currents to be applied during readout. The ICNE method can reconstruct current-induced images from nonlinear gradients caused by the currents without systematic artifacts. This increases the phase sensitivity by increasing the current-time product. It should be noted that currents applied during in-vivo human brain imaging are much lower than for phantom studies to ensure subject comfort and safety. Therefore, currents can be applied during the readout gradients without applying the ICNE method for reconstruction.

In 2010, Han et al. [15] employed a multi-echo spin-echo (MESE) sequence combined with the ICNE method and compared it to the standard SE sequence. Nam and Kwon [16] extended this method by using multiple gradient echoes in between each refocusing RF pulse, a gradient and spin-echo sequence (GRASE). Both studies found that the multi-echo methods obtained a higher SNR from measuring multiple echoes and higher phase sensitivity due to the longer current injection times.

Gradient echo (GRE) sequences have also been used for MRCDI. Sequences without a refocusing pulse, like GRE, are affected by main field inhomogeneities to a higher degree and have a lower SNR due to T_2^* decay but are generally faster than SE sequences. In 2005 Oh et al. [17] used a single-echo GRE sequence to increase the spatial resolution compared to previous studies. In 2012 Kim et al. [18] studied the effect of using a multi-echo gradient echo (MGRE) sequence while employing the ICNE method. They suggested a method to optimally combine the echoes to reduce magnetic field measurement noise based on the signal strength of the magnitude image.

The use of GRE sequences is not limited to spoiled sequences. steady-state free precession (SSFP) sequences have also been studied. In 2009 Minhas et al. [19] suggested the use of a balanced SSFP (bSSFP) sequence due to its high SNR and off-resonance phase sensitivity and performed a simulation study. However, to my knowledge, bSSFP has not been tested experimentally to date. Quantification of the current-induced magnetic fields may also be challenging due to the spatially varying steady state condition depending on T_1, T_2 and the local B_0 field. In 2016, Lee et al. [20] performed an SSFP study where they used both SSFP-FID and SSFP-ECHO with current injection before or after readout. They concluded that SSFP-FID with current injection before readout had the highest sensitivity to currents. Göksu et al. [21] extended the current injection time to also be applied during readout to increase the phase sensitivity. They also compared the efficiency of the SSFP-FID sequence to a MESE sequence. They found that efficiency of SSFP-FID was three times higher when one slice was acquired due to the long dead time needed for MESE to recover the longitudinal magnetization. However, for MESE it is possible to acquire additional slices during the dead time.

Echo planar imaging (EPI) techniques have been suggested for MRCDI to reduce imaging time or increase temporal resolution. Hamamura and Muftuler [22] demonstrated in a phantom that it was possible to use single-shot, spin echo, EPI for MRCDI, after performing ghost and distortion correction. Seo et al. [23] mentioned the possibility of using GRE-based EPI with current injection during the whole readout time to increase the temporal resolution in MRCDI but did not perform the experiments.

1.3 Human in-vivo brain MRCDI

Only six human in-vivo brain MRCDI studies have been reported to date. In 2016, Jog et al. [24] used a standard gradient-echo field mapping technique to map current-induced magnetic fields during a transcranial direct current stimulation (tDCS) session. With the wish to concurrently assess neurophysiological response to tDCS with functional MRI (fMRI) and image current-induced magnetic fields Jog et al. [25] performed a second study where they used a dual-echo EPI sequence. The first echo was used to estimate the current-induced perturbation of the phase images, while the second echo was used for blood-oxygenation-level-dependent (BOLD) contrast. All previously mentioned MRCDI methods use alternating current directions for each excitation and subtract phase images to estimate the influence of the currents. This makes the methods relatively robust to main field fluctuations. Since the interest is in measuring the effect of tDCS where the currents are constant in the range of minutes it is not possible to measure the field changes of alternating current directions, rendering this method very sensitive to field fluctuations from for example physiological noise or system instabilities. Therefore, their methods were not sensitive enough to reliably detected current-induced field changes in individual subjects.

In 2017, Kasinadhuni et al. [26] used a MGRE sequence to image three brain slices. They reported 0.2 nT noise levels but did not obtain a good correspondence between simulated and measured magnetic fields. Additionally the inter-subject magnetic fields measurements were inconsistent and randomly distributed zero-mean noise for zero current was not demonstrated. In 2018, Chauhan et al. [27] performed a human in-vivo brain diffusion tensor MREIT (DT-MREIT) study. DT-MREIT is used to estimate the anisotropic conductivity by assuming a linear relationship between the conductivity tensor and diffusion tensor. The current-induced magnetic fields were acquired with the same MGRE sequence as in the previous study [26]. However, also in this study, the measured magnetic fields were higher than expected from simulations. The errors in the measured magnetic fields in the two previously mentioned studies were very likely caused by magnetic fields from the currents flowing in the lead wires. The necessity for cable current stray field correction was first described by Göksu et al. [28] in their human in-vivo brain study in 2018. They used the op-

timized MESE and SSFP-FID sequence from their previous phantom study [21] and obtained a noise level of 0.1 nT with the SSFP-FID sequence. This was the first human in-vivo brain study to produce reliable current-induced magnetic field measurements that were largely in agreement with simulations. Later Göksu et al. [29] optimized their acquisition strategy by using acquisition weighting to reduce ringing artifacts. Instead of the previously used SSFP-FID sequence, a MGRE sequence with RF spoiling and extended gradient spoiling was used. The extended gradient spoiling reduces flow artifacts in CSF, while the RF spoiling eliminates the error-prone steady-state modeling needed to calculate an accurate magnetic field from phase images in SSFP sequences.
The previously mentioned studies obtained data from only one [28], two [29], or three slices [26, 27]. To increase volume coverage Chauhan et al. [30] used a multi-band (MB) MGRE sequence to acquire 24 slices with a MB factor of 8. However, measurements without current were not performed to asses the measurement quality. Therefore the noise level increase due to the use of a high multi-band factor was not described.

1.4 Objectives

The first main objective of this thesis came about from the necessity to correct lead wire stray magnetic fields influencing the current-induced magnetic field measurements. Although stray field correction methods can be used [31], they are not perfect and stray fields are best also reduced in the first place. Due to the safety hazard that arises when highly conductive materials are used in an MR scanner, and especially when attached to the subject, safety precautions have to be taken by the manufacturer of the MR compatible neurostimulators. Usually, the manufacturers require a certain lead path to be used, to reduce the risk of adverse heating. This excludes the possibility to position the leads optimally for MRCDI to reduce the influence of lead wire stray fields. Additionally, 5 kΩ safety resistors are placed in each lead wire to reduce the pickup of RF energy. With commercial limited voltage neurostimulators, this limits the amount of current that can be applied during MRI. The aim was therefore to

design new lead wires without the presented limitations while having safety in focus. The noise in MRCDI can be measured by acquiring data without injected currents, which results in noise floor images. In previous studies where the noise floor images have been presented [28, 29], it has been clear that the noise is not spatially uniform and low-frequency spatial patterns, not present in phantom data, exist. This noise is believed to arise from physiological effects such as movement, respiration, and heartbeat.

The second main objective of this thesis was to test faster imaging sequences for MRCDI to improve robustness to physiological noise sources. Additionally, sequences with a higher temporal resolution also open the possibility to perform physiological noise correction in post-processing.

1.5 Outline

In **chapter 2** the MR acquisition theory for MRCDI is presented followed by a noise analysis of magnetic field measurements. Finally, the post-processing of magnetic field measurements, with the aim of obtaining current densities or tissue conductivities, is briefly discussed.

In **chapter 3** the noise analysis given in chapter 2 is studied experimentally for EPI-based MRCDI. An introduction to physiological noise correction in MRI is also given followed by an evaluation of the effect it has on MRCDI using an EPI sequence.

In **chapter 4** an introduction to the manuscript presented in Appendix A where EPI-based MRCDI was compared to MGRE-based MRCDI is given.

In **chapter 5** MR safety of external leads is discussed and the article in Appendix B and the conference abstract in Appendix C on the safety study of new MRI-TES leads is introduced.

In **chapter 6** the topics presented in this thesis and future perspectives are discussed.

CHAPTER 2

MRCDI Theory

In this chapter, an introduction to the MR acquisition theory for MRCDI is given, followed by a noise analysis linking the noise in the magnetic field measurements to the noise in the magnitude images. Finally, the topic of reconstruction of magnetic field measurements into either current density or tissue conductivity is discussed briefly.

2.1 Measurements of current-induced magnetic fields by MRI

The standard GRE sequence is used in this description to give a simple theoretical example of current-induced magnetic field measurements by MRI. The sequence is presented in figure 2.1. For a detailed description on MR signal generation the reader is refereed to other literature [32]. Ignoring relaxation during sampling, the acquired signal is

$$S(k_x, k_y) \propto \int\int M(x, y) e^{j\delta(x,y)} e^{j(xk_x + yk_y)} dx\, dy \tag{2.1}$$

where k_x and k_y are locations in k-space, x and y are locations in image space, M is the spatially varying transverse magnetization vector expressed as a complex number, and δ is the phase caused by main field inhomogeneity at the time of acquisition. For the purpose of understanding how the current-induced magnetic field is detectable by MRI, it is here sufficient to assume that all data points in k-space are sample instantaneously, thus leaving out the time dependence of k_x, k_y and S. Injecting currents in synchrony with the sequence as presented in figure 2.1 results in an additional phase accumulation proportional to the strength of the z-component of the spatially varying magnetic field (B_{zc}) and current injection time (T_c). This was presented as the

current-time product in the introduction. The equation above then becomes

$$S^{\pm}(k_x, k_y) \propto \int\int M(x,y) e^{j\delta(x,y)} e^{\pm j\gamma B_{zc}(x,y)T_c} e^{j(xk_x+yk_y)} dx\, dy\,. \tag{2.2}$$

Sampling each k-space line twice with the opposite current direction gives the complex signal $S^{\pm}$ with opposite phase perturbations. Reconstructing the images with two-dimensional Fourier transform gives

$$I^{\pm}(x,y) \propto M(x,y) e^{j\delta(x,y)} e^{\pm j\gamma B_{zc}(x,y)T_c}\,, \tag{2.3}$$

where $I^{\pm}$ are the two sets of reconstructed complex images. The phase difference ($\Delta\varphi$) of the two images is obtained by taking the argument of the divided complex images

$$\Delta\varphi(x,y) = arg\left(\frac{I^{+}(x,y)}{I^{-}(x,y)}\right) = 2\gamma\Delta B_{zc}(x,y)T_c\,, \tag{2.4}$$

where ΔB_{zc} is the difference in the magnetic field from negative and positive currents. Since δ is assumed to be constant over time it disappears in the division of the complex images. Finally to obtain the current induced magnetic field in each voxel we have

$$\Delta B_{zc}(x,y) = \frac{\Delta\varphi(x,y)}{2\gamma T_c}, \tag{2.5}$$

where $2\gamma T_c$ is the phase sensitivity to the current-induced magnetic fields.

2.1.1 Noise in current-induced magnetic field measurements

For high signal to noise ratio (SNR), the standard deviation of the phase images (σ_φ) is equal to the inverse of the local SNR of the magnitude images [33].

$$\sigma_\varphi = \frac{1}{\mathrm{SNR}}\,. \tag{2.6}$$

For subtracted phase images, as used in MRCDI, the noise variance adds leading to a standard deviation of subtracted phase images being

$$\sigma_{\Delta\varphi} = \frac{\sqrt{2}}{\mathrm{SNR}}\,. \tag{2.7}$$

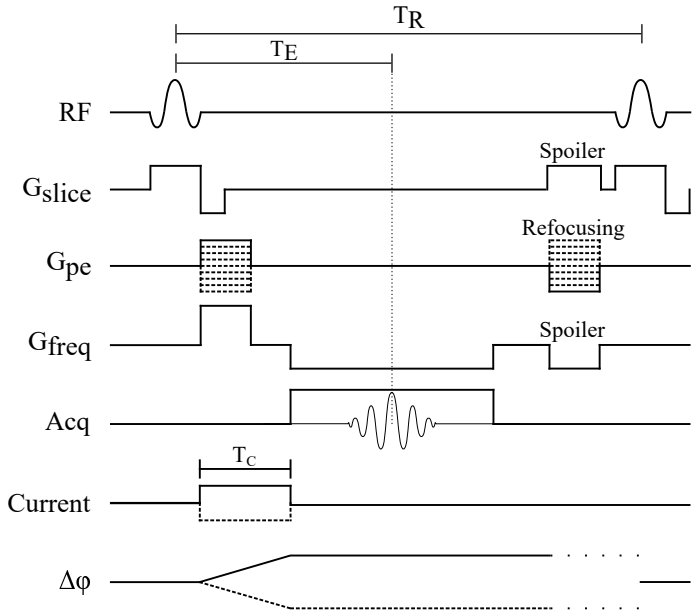

Figure 2.1. Gradient echo sequence used to provide a theoretical example of current-induced magnetic field measurements by MRI.

Combining equation 2.5 and 2.7 gives the standard deviation of the magnetic field measurements

$$\sigma_{\Delta B_{zc}} = \frac{\sqrt{2}}{2\gamma T_c \mathrm{SNR}} = \frac{1}{\sqrt{2}\gamma T_c \mathrm{SNR}}\,. \tag{2.8}$$

To improve the current-induced magnetic field estimates, $\sigma_{\Delta B_{zc}}$ has to be reduced. From equation 2.8 this can be achieved by either increasing the current injection time or improving the SNR of the magnitude image, assuming constant γ. SNR of the magnitude image is highly sequence-dependent. However, generally higher T_E, allowing for higher T_C, leads to lower SNR due to T_2 or T_2^* decay. Therefore there is a trade-off between long T_C and high SNR to achieve the optimal $\sigma_{\Delta B_{zc}}$. The employed MRCDI sequence should therefore be optimized to achieve the best possible ΔB_{zc} estimate by reducing $\sigma_{\Delta B_{zc}}$.

It should be noted that the relationship between the noise in the magnitude and phase image given in equation 2.6 only holds for independent and identically distributed (iid)

random noise such as thermal noise from the subject or from the MR scanner electronics. If main field variations occur, e.g. drifts in the B_0 field or field fluctuations caused by respiration or heartbeat, the relative phase noise may be much stronger than the relative magnitude noise. The influence this has on MRCDI is studied in chapter 4.

2.2 Post-processing of current-induced magnetic field measurements

The current-induced magnetic field measurements are not very useful without further post-processing. The magnetic field measurements have previously either been used to reconstruct current density images (MRCDI) or conductivity images (MREIT). Using Ampère's law, and ignoring displacement currents and tissue permeability, current densities can be related to the magnetic field as

$$\boldsymbol{J} = \frac{\nabla \times \boldsymbol{B}}{\mu_o}, \tag{2.9}$$

where $\nabla\times$ is the curl operator and μ_0 is the permeability of free space. To reconstruct each current density component the two orthogonal magnetic field components have to be available. This is clear if equation 2.9 is decomposed into each current density component as

$$J_x = \frac{1}{\mu_o}\left[\frac{\partial B_z}{\partial y} - \frac{\partial B_y}{\partial z}\right], \tag{2.10}$$

$$J_y = \frac{1}{\mu_o}\left[\frac{\partial B_x}{\partial z} - \frac{\partial B_z}{\partial x}\right], \tag{2.11}$$

$$J_z = \frac{1}{\mu_o}\left[\frac{\partial B_y}{\partial x} - \frac{\partial B_x}{\partial y}\right]. \tag{2.12}$$

However, only the magnetic field component parallel to the B_0 field can by imaged by MRI, denoted B_{zc} in equation 2.2. In phantom studies, the phantom can be rotated to image all three components with the same current injection, and the full current density can be reconstructed. In human studies, rotating the subject in the scanner is effectively impossible. Therefore, in human MRCDI, J_x and J_y can only be partially reconstructed while J_z is fully invisible.

In MREIT, surface voltage measurements are needed as well as two independent current injection directions. Various conductivity reconstruction algorithms have been developed for MREIT. These algorithms can generally be split into J-based and B_z-based algorithms. J-based algorithms need the full current density and therefore suffer from the same problems as MRCDI, where only one component of the current-induced magnetic field is measured. B_z-based algorithms were invented to get around this problem. However, a detailed description of MREIT reconstruction algorithms is outside the scope of this thesis. The reader is referred to detailed reviews on the subject [34, 35].

Apart from only having one magnetic field component available, reconstructing the current density or conductivity from magnetic field measurements also has other shortcomings. To obtain a sufficient sensitivity to current-induced magnetic fields, the scan time for human in-vivo scans is relatively long limiting the number of slices. This limits the brain volume where current or conductivity is reconstructed. Additionally, only sufficient data quality is obtained from gray matter, white matter, and CSF, with data missing from structures such as the skull and scalp. Without data from these tissues, their conductivities cannot be obtained. When the aim is to improve computational head models for TES, it is crucial to determine the conductivities for the skull and scalp as well. The ratio between scalp conductivity, which is relatively high, and skull conductivity being relatively low, determines how much current enters the brain and how much is shunted in the scalp.

Our group has recently suggested an alternative way of dealing with the magnetic field measurements [36]. Instead of directly reconstructing current density or conductivities from the magnetic field measurements, a subject-specific head model with separate tissue types is created. With literature conductivities assigned to each tissue type, the current density and magnetic fields can be calculated. An optimization problem is then formulated where the error between the measured and simulated magnetic fields are minimized by updating the tissue conductivities in the simulated volume conductor model. For more details on this method see the full paper [36]. This method is also used in the manuscript in Appendix A presented in chapter 4.

CHAPTER 3
Physiological Noise in MRCDI

In the previous chapter, a simplified theoretical noise analysis relating $\sigma_{\Delta B_{zc}}$ to the SNR of the magnitude image was presented. Only sources creating iid noise were considered while other noise sources where the relationship between the noise in the magnitude and phase images is less predictable were ignored. In this chapter, the effect of physiological noise from respiration and heartbeat on the magnitude and phase images is analyzed and how it translates to noise in ΔB_{zc} measurements when an EPI sequence is used. Physiological noise reduction will also be applied to assess whether it can improve the quality of measured current-induced magnetic fields.

3.1 Introduction

Movement of the abdomen and thorax during breathing results in magnetic field fluctuations observable in the brain. Magnitude images are weakly affected by these changes, while the fluctuations are much more severe for the phase images [37]. If a volume is sampled multiple times to create a time series of data, the changes of the phase in a given voxel over time is directly proportional to the local B_0 field variations, assuming imaging parameters are kept constant. The sensitivity of the phase images to variations of the main magnetic field over time makes it possible to measure current-induced magnetic fields, but is also the reason the phase images are more susceptible to respiration-induced noise. Cardiac-induced physiological noise in MR is mainly caused by the movement of the brain as well as flow effects close to vessels. Cardiac effects are therefore often more localized, while respiration effects can be observed globally.

In fMRI physiological noise correction methods are commonly used to increase the sensitivity to BOLD signal changes. A physiological denoising method was first introduced by Hu el al. in 1995 [38]. They measured the cardiac signal with a pulse

oximeter on the finger and the respiration with a pressure-sensitive belt around the abdomen. The timing of the acquired image was determined relative to the previous and following peak of the cardiac and respiratory signal. Assuming quasi-periodic signal fluctuations, a low-order Fourier series was created and fitted to measurements. The physiological noise was corrected in k-space and the technique was later termed RETROKCOR. The most common physiological noise correction method used in fMRI today is called RETROICOR and was introduced in 2000 by Glover et al. [39]. The method mainly differs from RETROKCOR by performing the correction in image space instead of k-space. RETROICOR benefits from fitting each voxel of the images independently, which is especially an advantage where the noise is localized in image space, for example around vessels for cardiac induced noise. RETROKCOR can only correct spatial frequencies where the SNR in k-space is adequate [39]. It is also computationally cheaper to perform the correction in image space after coil combination since RETROKCOR has to be performed on each coil element.
Other physiological noise correction methods addressing specific issues have been developed but are not relevant for the analysis performed in this chapter. For more details on noise correction, the reader is referred to other literature such as a detailed review on fMRI noise correction methods by Caballero-Gaudes et al. [40].

3.2 Methods

The noise in the magnitude images (I_m), phase images (φ), and subtracted phase images ($\Delta\varphi$) will be studied and related to the theoretical relationship given in section 2.1.1 (eq. 2.6 and 2.7). Since the relationship between $\Delta\varphi$ and ΔB_{zc} is direct proportionality (eq. 2.5) and only scaled by the phase sensitivity of the sequence, ΔB_{zc} can be ignored in this analysis.

Data acquisition

A human volunteer was scanned with an EPI sequence. A single slice was acquired to obtain a high temporal resolution. The sequence parameters were TR = 100 ms, TE = 50 ms, FOV = 182×223 mm^2, matrix size = 62×76 and flip angle = 30°. A thousand images were acquired resulting in a total acquisition time of 100 seconds.

The noise level of the magnetic field measurements is evaluated as the spatial standard deviation of the current-free ΔB_{zc} images. Therefore no currents were applied in this experiment.
Respiration measurements were performed with a pneumatic belt around the upper abdomen of the subject and the pulse was measured with a pulse oximeter on the index finger.

Analysis

The SNR in the magnitude images is evaluated using the temporal mean signal and temporal fluctuations in each voxel. This is usually referred to as the signal to fluctuation noise ratio (SFNR) and is given as:

$$\mathrm{SFNR}(\boldsymbol{r}) = \frac{\overline{I_m(\boldsymbol{r})}}{\sigma_{I_m}(\boldsymbol{r})}\,, \tag{3.1}$$

where $\overline{I_m(\boldsymbol{r})}$ denotes the temporal mean and $\sigma_{I_m}(\boldsymbol{r})$ is the temporal standard deviation of the signal in a voxel at position $\boldsymbol{r}$. The standard deviation of φ and $\Delta\varphi$ are also evaluated as the temporal fluctuation of the signal in each voxel. A second-order polynomial detrending was performed for both the magnitude and phase images to remove slow signal drifts.
To evaluate whether the relationships between the SNR of I_m and noise in φ or $\Delta\varphi$ images are as given in the previous chapter (eq. 2.6 and 2.7), the standard deviation of the measured φ and $\Delta\varphi$ is used to calculate the expected SNR of the magnitude image and compared to the experimentally measured SFNR. Equation 2.6 and 2.7 then become:

$$\mathrm{SFNR}_{\varphi}(\boldsymbol{r}) = \frac{1}{\sigma_{\varphi}(\boldsymbol{r})}\,, \quad \mathrm{SFNR}_{\Delta\varphi}(\boldsymbol{r}) = \frac{\sqrt{2}}{\sigma_{\Delta\varphi}(\boldsymbol{r})}\,, \tag{3.2}$$

where $\mathrm{SFNR}_{\varphi}(\boldsymbol{r})$ and $\mathrm{SFNR}_{\Delta\varphi}(\boldsymbol{r})$ denote the expected SNR from the phase and subtracted phase variation in each voxel. If $\mathrm{SFNR}_{\varphi}(\boldsymbol{r})$ or $\mathrm{SFNR}_{\Delta\varphi}(\boldsymbol{r})$ is lower than SFNR there is less relative noise in the magnitude image than in φ and $\Delta\varphi$ and vice versa.
The SNR evaluations using these methods are not the combined SNR of the whole time series, but instead, represent the average SNR of each voxel for one acquisition.

In MRCDI, when multiple measurements are performed they are combined by temporally averaging the signal in each voxel, after consecutive images are subtracted, to reduce the noise. The thermal noise is then theoretically reduced by the square root of the number of sets of subtracted images. After averaging, the noise cannot be evaluated in the same way as the methods above since the temporal dimension is removed. The noise level in MRCDI is instead evaluated from the spatial standard deviation, either over a region of interest (ROI) or the whole slice, for an acquisition without current injection. However, since iid noise is identical in the spatial and temporal dimensions, taking the temporal standard deviation followed by a spatial average is equivalent to temporally averaging and then taking the spatial standard deviation, except for the reduction of the noise obtained by averaging multiple measurements. This can be expressed as

$$\frac{\sigma_{\Delta\varphi}(\mathbf{\Omega})}{\sqrt{N}} = \sigma_{\Delta\varphi_{mean}}(\mathbf{\Omega}), \tag{3.3}$$

where $\mathbf{\Omega}$ denotes a ROI and $\sigma_{\Delta\varphi}(\mathbf{\Omega})$ is spatially averaged in the ROI. $\sigma_{\Delta\varphi_{mean}}(\mathbf{\Omega})$ is instead temporally averaged to reduce noise, while the noise is estimated from the spatial standard deviation in the ROI. Combining equation 3.2 and 3.3 the estimated SNR from the temporally averaged subtracted phase images $\Delta\varphi_{mean}$ is then

$$\mathrm{SFNR}_{\Delta\varphi_{mean}}(\mathbf{\Omega}) = \frac{\sqrt{2}}{\sigma_{\Delta\varphi_{mean}}(\mathbf{\Omega})\sqrt{N}}, \tag{3.4}$$

Noise correction

The noise correction method was implemented in the python programming language following the RETROICOR theory [39]. The physiological noise $y_\delta(t)$ is modeled as a Fourier series

$$y_\delta(t) = \sum_{m=1}^{M} a_m^c \cos\left(m\varphi_c\right) + b_m^c \sin\left(m\varphi_c\right) + a_m^r \cos\left(m\varphi_r\right) + b_m^r \sin\left(m\varphi_r\right), \tag{3.5}$$

where φ_r and φ_c are the phases of the respiratory and cardiac cycle at the time of acquisition, M is the order of the Fourier series and a and b are the weighting factors to be determined for each voxel. The phase of the cardiac signal is

$$\varphi_c(t) = 2\pi(t - t_1)/(t_2 - t_1), \tag{3.6}$$

where t is the time of image acquisition and t_1 and t_2 are the times of the preceding and following peak of the cardiac signal.
The magnetic field changes in the brain caused by respiration are not only dependent on the phase of the respiration cycle, but also on the depth of the breathing. φ_r is therefore related to the respiratory amplitude with a histogram-equalized transfer function as

$$\varphi_r(t) = \pi \frac{\sum_{b=1}^{\mathrm{rnd}[R(t)/R_{max}]} H(b)}{\sum_{b=1}^{100} H(b)} \mathrm{sgn}(dR_f/dt)\,. \tag{3.7}$$

R is the measured respiration signal, H is a histogram with 100 bins (b) created from all values of R, and rnd is an integer round-off operator. The sign of the phase is positive for inhalation and negative for exhalation. The sgn operator determines the sign from the derivative of the measured respiration signal after filtering (R_f). To avoid jumps in the sign of the phase, caused by noise in the respiration signal, the measured signal is first low-pass filtered with a kernel length corresponding to approximately 1 second.
To determine the coefficients of the Fourier series (a and b) a general linear model (GLM) can be used. Equation 3.5 can be expressed in matrix form as

$$\boldsymbol{Y} = \boldsymbol{X}\boldsymbol{\beta} + \boldsymbol{\epsilon}\,, \tag{3.8}$$

where $\boldsymbol{Y}$ is the temporal signal in each voxel, $\boldsymbol{X}$ is the design matrix containing the sine and cosine functions from equation 3.5, $\boldsymbol{\beta}$ components are the a and b coefficients from 3.5 and $\boldsymbol{\epsilon}$ is the residuals. Solving the GLM gives the $\boldsymbol{\beta}$ values for each regressor in each voxel, or in other words, how much of the signal fluctuations in a voxel can be explained by a given physiological noise regressor.

3.3 Results

The effect of the respiration and cardiac pulsation on the phase data is presented in figure 3.1. The average phase in a region of interest (denoted in figure 3.2) is plotted against the respiratory and cardiac phases at the time of acquisition. There is a very clear correspondence between the phase signal and the whole respiration cycle,

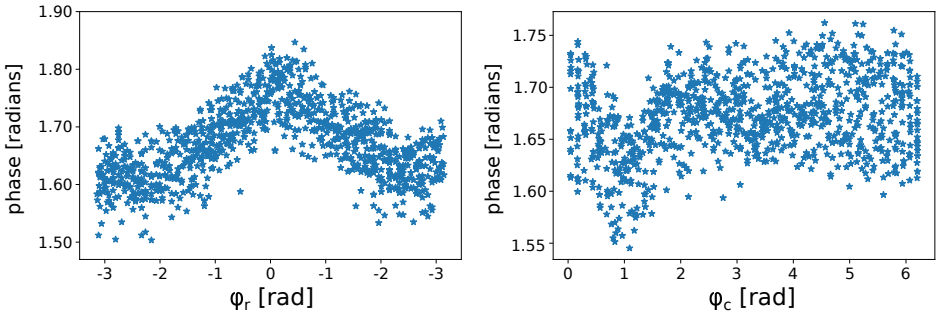

Figure 3.1. The average phase in a ROI versus the respiratory (left) and cardiac (right) cycle at the time of data acquisition. The respiratory effect was removed before plotting the effect of the cardiac noise to better visualize the effect. The ROI is denoted in figure 3.2a.

whereas the cardiac effect on the phase signal is stronger right after a heart beat and then fades away.

The SFNR in I_m and temporal noise in φ, and $\Delta\varphi$ before and after correction is presented in figure 3.2. In agreement with previous studies [41], physiological noise has much more influence on the phase data than on the magnitude data. This is evident from the percentage improvement presented in the last column. Subtracting two consecutive phase images acts as a high-pass filter, which is clear from the $\Delta\varphi$ ROI time series.

The time-averaged subtracted phase image $\Delta\varphi_{mean}$ is not presented in figure 3.2 since the temporal dimension is removed. Instead $\text{SFNR}_{\Delta\varphi_{mean}}$ in a ROI (same ROI as given in top left image in figure 3.2) is presented together with SFNR from I_m, σ_φ, and $\sigma_{\Delta\varphi}$ in table 3.1. As expected from figure 3.2, the effect of correction on SFNR_φ and $\text{SFNR}_{\Delta\varphi}$ is greater than the effect on SFNR. However, interestingly the physiological correction has a limited effect on $\Delta\varphi_{mean}$, and $\text{SFNR}_{\Delta\varphi_{mean}}$ is close to SFNR. In table 3.1 the noise is only presented for a ROI. However, the spatial variation of the noise is different for each of the images. In figure 3.3 the ratio between $\text{SFNR}_{\Delta\varphi_{mean}}$ and SFNR is presented as images before and after correction. SFNR and $\text{SFNR}_{\Delta\varphi_{mean}}$ were computed with a 5x5 spatial kernel before obtaining the ratio. For values above one, $\Delta\varphi_{mean}$ has lower noise than theoretically expected from SFNR of

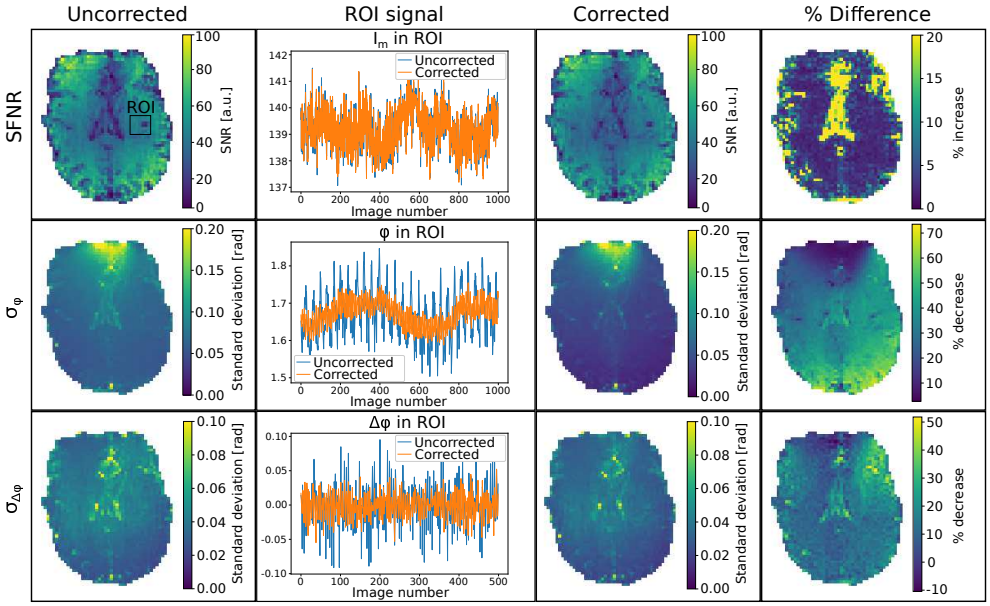

Figure 3.2. Voxelwise SFNR, σ_{φ}, and $\sigma_{\Delta\varphi}$ images are presented in each row. The first column is the uncorrected SFNR and noise images. Column two shows the average time series in a ROI (denoted in the upper left image) before and after correction. The third column is the SFNR and noise images after correction, while the last column is the percentage voxelwise improvement after correction.

	SFNR(Ω)	SFNR$_{\varphi}$(Ω)	SFNR$_{\Delta\varphi}$(Ω)	SFNR$_{\Delta\varphi_{mean}}$(Ω)
Uncorrected	43.84	14.96	33.42	48.10
Corrected	44.97	24.85	40.67	48.21

Table 3.1. Presenting SFNR, SFNR$_{\varphi}$, SFNR$_{\Delta\varphi}$, and SFNR$_{\Delta\varphi_{mean}}$ in a ROI before and after physiological correction. Note that correction has the most influence on SFNR$_{\varphi}$ and SFNR$_{\Delta\varphi}$, while SFNR$_{\Delta\varphi_{mean}}$ is close to the values for SFNR.

the magnitude images. After correction, the peak of the distribution moves closer to one indicating that the magnitude images are corrected more than the $\Delta\varphi_{mean}$ images, especially present in the ventricles.

So far, the noise in the $\Delta\varphi_{mean}$ images has only been evaluated as the standard deviation in a small ROI and compared to SFNR of the magnitude image. This does not capture spatial low-frequency noise patterns in the image, which would influence the mean in a small ROI and not the standard deviation. The low-frequency spatial patterns in $\Delta\varphi_{mean}$ are best evaluated qualitatively. ΔB_{zc} noise floor images are created from measurements without injected currents. As previously mentioned, ΔB_{zc} is directly proportional to $\Delta\varphi_{mean}$ and therefore also the noise in the images. In figure 3.4, ΔB_{zc} is used instead of $\Delta\varphi_{mean}$ to relate the noise floor to magnetic field measurements. The bottom row shows the histogram of voxel intensities and a fitted Gaussian distribution indicating the standard deviation (σ) and the mean (μ) of the distribution over the whole brain slice. Interestingly, a 4th order cardiac noise correction has no noticeable influence on the data, while a 5th order correction slightly reduces σ over the whole brain. Especially noticeable is the blue patch on the upper right of the images, which disappears with the 5th order correction. Additionally, adding respiratory

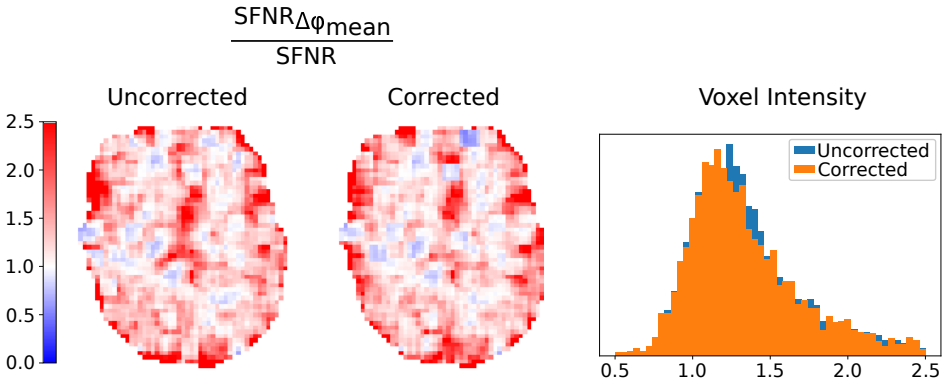

Figure 3.3. Uncorrected (left) and physiological noise corrected (middle) images presenting the ratio between $\mathrm{SFNR}_{\Delta\varphi_{mean}}$ and SFNR. A 5x5 kernel was used to calculate SFNR and $\mathrm{SFNR}_{\Delta}\varphi_{mean}$ in each voxel before taking the ratio. With only iid noise present, the ratio should be one. A histogram of the voxel intensities before and after correction is presented to the right.

correction has no effect on the noise floor images.

3.4 Discussion and conclusion

In this chapter, the theoretical noise analysis given in chapter 2 linking ΔB_{zc} to the SNR of the magnitude image via the noise in phase images was studied. As expected from previous studies [37] the theoretical analysis assuming iid noise does not hold for human measurements where physiological noise plays a substantial role. The phase images are more susceptible to field fluctuations caused by for example movement of the thorax during respiration. Since ΔB_{zc} is based on phase measurements, it is natural to assume that ΔB_{zc} measurements are also more susceptible to these noise sources. The effect of physiological noise on ΔB_{zc} measurements has to my knowledge not been studied previously.

Physiological noise correction was also performed to reduce the influence of respiration or cardiac induced noise. The physiological noise correction presented in figure 3.2 shows that the correction worked as expected, with the phase data being cor-

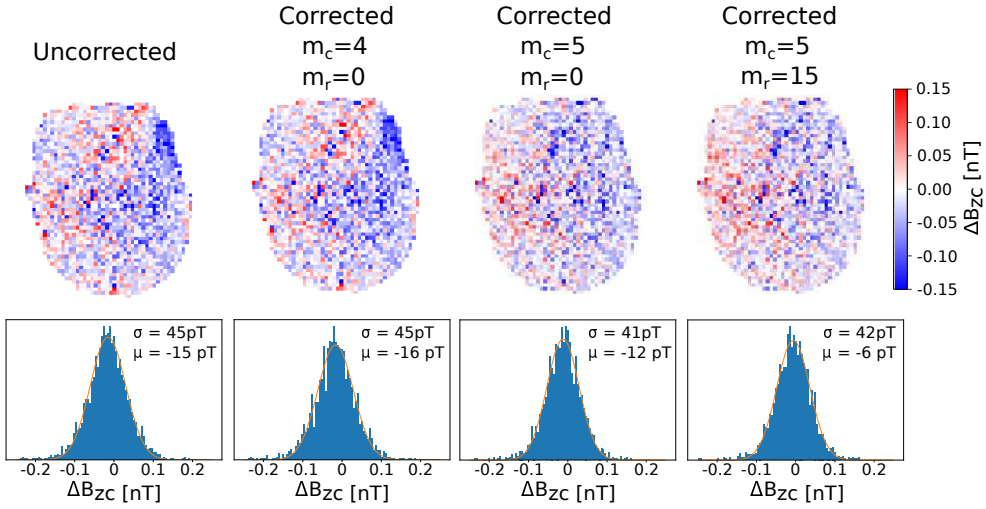

Figure 3.4. The first row shows the current free ΔB_{zc} images without correction (left) and with correction with cardiac regressors of 4th and 5th order (middle images) and after adding 15 respiration regressors (right). The second row shows the histograms of the voxel intensities and a Gaussian fit to the data.

rected more than the magnitude data. The magnitude data is mostly corrected in regions with CSF whereas the correction of the phase image is more global. The lack of correction in the frontal part of the phase image is most likely due to low T_2^* resulting in more random uncorrectable noise. From table 3.1 and the color bars in the first column of figure 3.2, it is clear that the noise in $\Delta\varphi$ is lower than in φ. This is due to the subtraction of consecutive data points acting as a high-pass filter with a cut-off frequency of approximately $1/(2T_R)$ or in this case around 5 Hz. This is the same as the frequency of the injected currents in MRCDI. Additional physiological noise correction still has a substantial influence on the noise in $\Delta\varphi$. Although physiological noise correction improves the stability of the phase data, SFNR_{φ} in the chosen ROI (see table 3.1) is not equal to SFNR in the magnitude image. This is most likely because of the very low-frequency fluctuations with a period of almost the full acquisition time of 100 seconds present in the ROI signal for the phase data in figure 3.2. This fluctuation is expected from hardware imperfections such as varying temperature of the gradients and cooling water.

Interestingly, even though physiological noise correction reduces the noise in φ and $\Delta\varphi$ it has very limited influence on ΔB_{zc}. In table 3.1, $\mathrm{SFNR}_{\Delta\varphi_{mean}}$ is almost unchanged before and after correction and is also close to SFNR, or the noise level expected for iid noise. In figure 3.3 the ratio of $\mathrm{SFNR}_{\Delta\varphi_{mean}}$ and SFNR was presented as an image. Assuming only iid noise the ratios should be one. However, the noise in $\Delta\varphi_{mean}$ is lower than in I_m in CSF regions, which is also where I_m has the lowest SNR. After correction, the ratio is closer to one, especially in the ventricles. The peak of the histogram is slightly higher than one, indicating that the noise in $\Delta\varphi_{mean}$ is lower than theoretically expected. However, this is not true since the noise in the magnitude data is not fully iid noise. From the magnitude ROI signal in figure 3.2 it is clear that low-frequency fluctuations are present in the magnitude data, which are not present in $\Delta\varphi$ data.

In fMRI, reducing the high-amplitude fluctuations is sufficiently achieved with a second-order Fourier series [39]. For MRCDI, the problem is different. The low-order high-amplitude fluctuations are filtered out when the phase images are subtracted (see figure 3.2). Higher frequency noise is further filtered out when the tem-

poral mean is performed to obtain $\Delta\varphi$, as long as the noise has zero mean. $\Delta\varphi$ is therefore only affected by noise at the same frequency as the injected current, which is synchronized with the MR sequence. Or in other words, noise is only significant if the current injection signal and noise are correlated. Therefore, if RETROICOR is used, a sufficiently high order has to be used to correct the right frequency content. This is demonstrated in figure 3.4, where 4th order cardiac correction has no influence on ΔB_{zc} but correction is observable when the 5th order is added to the correction. When TR is 100 ms the alternating current has a frequency of 5 Hz. The subject had a pulse very close to 1 Hz resulting in a 5th harmonic of the pules having the same frequency as the injected current. Following the same argument for respiration, a 15th order Fourier series has to be used when the respiration frequency is about 0.33 Hz. Adding a 15th order respiration correction had no visible effect on ΔB_{zc}.

It has to be noted that the data set used in this chapter has been cherry-picked to demonstrate that physiological correction can, in specific cases, have an influence on the noise in ΔB_{zc}. Other data sets have also be acquired, both with other subjects and other sequence parameters. No difference was observed for other data sets when analyzing the random noise in the $\Delta\varphi$ as presented in table 3.1 and figure 3.3. The only difference was that no spatial low-frequency noise that could be corrected with noise correction as shown in figure 3.4 was present in the other data sets.

In conclusion, with a sufficiently high temporal resolution where the current injection frequency is much higher than physiological noise, and preferably not an integer multiple of the heart rate, ΔB_{zc} is fairly insensitive to physiological noise, due to the measurement design.

Although physiological noise correction has proven not to be crucial for the noise in ΔB_{zc} when using EPI and when one slice is acquired, this analysis can assist in deciding how to acquire more than one slice to have a greater brain coverage. All slices can be acquired sequentially with one current direction and then again with the opposite direction, which would result in a reduction of the current injection frequency by the number of slices. For example, acquiring 5 slices where the excitation time between each slice is 100 ms the current injection frequency would be 1 Hz unless multi-band or other acceleration techniques are used. In that case, the physiological noise is ex-

pected to play a bigger role and noise correction would be necessary. Instead, one slice could also be acquired multiple times to reduce the noise, before moving on to the next slice. That way the current injection frequency would be the same as in the experiment presented in this chapter and physiological noise would not be a problem. Although the first option has the advantage that T_R becomes longer and therefore the net magnetization vector has more time to recover resulting in a larger SNR, the insensitivity to physiological noise presents a more desirable option. In the manuscript in Appendix A presented in the next chapter on EPI-based MRCDI five slices were acquired. Based on the analysis in this chapter it was deemed advantageous to fully acquire all measurements for each slice before moving on to the next slice to maintain robustness to physiological noise in ΔB_{zc}.

CHAPTER 4

Magnetic field measurements with EPI

One of the main aims of this PhD was to reduce the low frequency noise patterns in the magnetic field measurements usually present in previous human in-vivo brain experiments. In the previous chapter it was shown that EPI-based MRCDI is robust to physiological noise and that physiological noise correction has very limited impact. Based on this knowledge a study was designed to compare EPI-based MRCDI with a recently developed MGRE sequence with acquisition weighting [29].

A loop experiment was first performed to validate the magnetic field measurements obtained with the EPI sequence. The loop experiment has previously been used by Göksu et al. [28,29]. In the experiment a lead wire is placed around the subject's head and a current in passed through it in synchrony with the MR sequence, as normally done in MRCDI. The main difference is that no current is injected into the subject's head. Instead a current flowing through the wire gives rise to a stray magnetic field in the brain measurable by MRCDI. The loop experiment is a good way to validate the performance of the sequence since the ground truth of the magnetic field in the measured volume can be calculated with the Biot-Savart law when the position of the lead wire in known. The residuals left after subtracting the Biot-Savart simulated magnetic fields from the magnetic fields calculated from the phase images can reveal whether the phase sensitivity for the sequence is as expected. It could for example reveal improper spoiling of transverse magnetization in regions with long T_2^* as was studied by Göksu et al. [29]. The loop experiment revealed that the sequence is performing as expected. Although residuals above the noise levels were present, due to their nature they are most likely caused by improper wire tracking or subject motion. Instead of attempting to reconstruct the current density in the imaged slices, as pre-

viously done in most human in-vivo brain MRCDI studies [26–29], the recently suggested method, briefly discussed in chapter 2, of optimizing the conductivities in a subject-specific head model by minimizing the difference between the simulated and measured magnetic fields, was used [36]. First the influence of noise floors from both the EPI and MGRE sequence were compared by evaluating the performance of the optimization with simulated data and added noise floors. One brain slice with a total acquisition time of 8:40 min was acquired with the MGRE and the EPI sequence as well as 5 EPI slices with 2 min acquisition time per slice to increase the brain coverage. As discussed in the previous chapter, all measurements for each EPI brain slice were fully acquired before moving on to the next slice to maintain the robustness to physiological noise. It was found that the EPI sequences, especially when 5 slices were acquired performed much better in the simulation experiment.
In the last experiment, conductivities were optimized by using measurements with injected currents of 1 mA for the MGRE sequence as well as 1 and 5 slice EPI acquisition. A right-left (RL) and anterior-posterior (AP) electrode montage was used. Interestingly, the difference between measured and simulated magnetic fields were at the same level for all acquisition methods and larger for the RL montage than for the AP montage. The difference was also consistent between subjects. This suggests that current MRCDI methods produce reliable and repeatable results and are sensitive enough to reveal current inaccuracies in the computational head models.
The manuscript in preparation is presented in Appendix A.

CHAPTER 5
RF Safety of External Leads

The previous chapters in this thesis have revolved around MRCDI. Although still relevant for MRCDI, the topic of this chapter is theoretically and practically different. A requirement for MRCDI is that conductive lead wires have to be attached to the subject inside the MR scanner. Here, the topic of RF safety concerning external leads is discussed and the published safety study of new lead wires presented in Appendix B is introduced.

MRI is generally considered to be safer than other medical imaging modalities such as computed tomography (CT) or positron emission tomography (PET) due to the absence of ionizing radiation. However, MRI relies on magnetic fields in three different frequency ranges, all leading to different safety risks. These fields are the main magnetic field at DC, the imaging gradient fields in the kHz range, and the radio frequency (RF) field in the MHz range. The safety risk of the main magnetic field is the force exerted on ferromagnetic materials, while the gradient fields can stimulate the peripheral nerves or cause auditory damage due to the noise created when currents flow in the gradient coils inside a strong magnetic field. The safety risks of the main magnetic field and the gradient fields will not be discussed further in this thesis. The reader is instead referred to other literature on MR safety, such as the review by Panych et al. [42]. The safety aspect of MRI-TES experiments, including MRCDI, differ from other MRI experiments by introducing conductive leads attached to the subject into the scanner. Since the safety risks associated with external leads come from the RF field, this will be the focus here.

The RF field is used to excite the nuclear spins and oscillates at the resonance frequency of the nuclei of interest. The resonance frequency is a product of the gyromagnetic ratio of the nuclei and the strength of the main magnetic field. The gyromagnetic ratio of protons is 42.58 MHz/T leading to an RF frequency for proton imaging

at 3T and 7T of approximately 128 MHz and 298 MHz, respectively. The magnetic field created by the RF coils usually denoted $\boldsymbol{B}_1$ is responsible for exciting the nuclear spins. According to the Maxwell-Faraday equation any time-varying magnetic field ($\boldsymbol{B}$) also gives rise to an electric field ($\boldsymbol{E}$):

$$\oint_c \boldsymbol{E} \cdot d\boldsymbol{l} = -\iint_s \frac{\delta \boldsymbol{B}}{\delta t} \cdot d\boldsymbol{S}\,, \tag{5.1}$$

where c is a curve and s a surface. In a conductive medium, the electric field gives rise to a current flow, which in turn leads to a resistive power loss resulting in heating of the material. Since biological tissue is conductive, RF excitation leads to heating of the tissue. To ensure that no tissue damage occurs due to excessive heating during an MRI exam, the energy deposited in the tissue is limited according to the guidelines set by the International Electrotechnical Commission [43]. The limits are given in specific absorption rate (SAR), expressed as deposited power per kilo tissue

$$\mathrm{SAR} = \sigma |\boldsymbol{E}|^2 / 2\rho\,, \tag{5.2}$$

where σ is the conductivity of the medium, ρ is the density and $|\boldsymbol{E}|$ is the peak electric field in the medium.

In general, the operator of the scanner does not have to be concerned about exceeding SAR levels resulting in excessive heating of tissue, since the scanners have limits implemented and will not allow for too high RF energy deposition in the subject. However, with highly conductive materials in the scanner, either attached to or inside the subject, safety risks are a real problem. Interaction between the RF field and highly conductive materials, such as medical implants or external lead wires does not necessarily give rise to an increased global SAR but can cause severe localized heating due to the pick up of RF energy by the object. The interaction between the RF field and the object in the scanner can either be via inductive coupling causing currents to flow in conductive loops (eq. 5.1) or by the straight wires acting as receive antennas, the so-called antenna effect. The $\boldsymbol{B}_1$ field will induce currents in any conductive loop, but loops in resonance with the RF frequency are especially dangerous. The antenna effect arises from currents induced in lead wires by an incident electric field oriented

parallel to the wire. The worst-case effect occurs for specific resonance lengths where standing waves are created on the wire.

In this thesis, the focus is on the RF safety of combined MRI-TES experiments and we will therefore only be concerned with the safety risks that arise from external leads attached to the subject via surface electrodes and not medical implants. This also includes combined EEG-MRI since the RF safety risks are closely related. As introduced briefly in chapter one, safety resistors (normally 5 kΩ) are usually installed in the lead wires to reduce the chances of adverse heating for MRI-compatible TES and EEG equipment. This is done to break high conductive paths, both for loops, where the tissue forms part of it, and for extended leads to reduce the chances of antenna effect. It has been shown that very high voltages (up to 850 V) can occur across the resistor during RF excitation [44]. If a resistor is close to the subject, the high E field created across it can induce a current in the subject resulting in heating of the tissue. Additionally, if the voltage rating of the resistors is too low, they might break during scanning, rendering the cables unusable. MRI compatible TES devices are therefore often limited to only be used with fMRI sequences. To further reduce the chances of heating, the vendors usually require that the leads are placed in a strict position within the coil to avoid that the leads are close to locations of high electric field.

As mentioned in the introduction, the limitations for MR compatible TES equipment that arise from safety concerns also limit the usefulness of the equipment. The main impact of the limitations are restricted lead paths resulting in stray magnetic fields in MRCDI, limited stimulation current strength, and restrictions on field strength. The aim was therefore to design new lead wires to be used with existing TES equipment that circumvented all of the aforementioned restrictions while having safety in focus. We decided to use distributed resistance in form of very low conductivity materials instead of using high conductivity materials and localized resistance. The main benefit is that highly conductive sections of the leads where a lot of RF energy can be picked up are avoided, which greatly reduces the safety risk. This increases the flexibility of where the leads can be positioned. Additionally, the total impedance can be kept lower than for the original leads, allowing for higher stimulation currents. For higher field strengths the length needed to observe the antenna effect decreases proportion-

ally. This is a limiting factor for using copper leads at ultrahigh field strength and is avoided with distributed resistance.
New electrodes and leads were created from carbon-doped silicone rubber with a conductivity of 29.4 S/m. The safety study of the leads, with both RF simulations and temperature measurements, is described in the published article in Appendix B and the conference abstract in Appendix C.

CHAPTER 6
Discussion and Conclusion

The focus of the work presented in this thesis has been to improve systematic errors in MRCDI. The two main topics were to create new MRI compatible current injection lead wires optimized for MRCDI and to reduce the influence of physiological noise in human brain experiments. A discussion on the safety issue of external leads wires attached to the subject inside the MR scanner as well as the new lead wires and the corresponding safety study was presented in chapter 5, in the published manuscript in Appendix B and in the abstract in Appendix C. The efforts to reduce physiological noise in MRCDI data can further be split up into two topics. One was to use an EPI sequence to decrease the acquisition time per measurement to increase the robustness to physiological noise, while the other was to further reduce the effect of physiological noise by using physiological noise correction methods. The physiological noise correction was discussed in chapter 3 while a study comparing EPI-based MRCDI to previously used MGRE-based MRCDI methods was presented in chapter 4 and in the manuscript in preparation in Appendix A

6.1 Physiological noise correction in MRCDI

The impact of physiological noise was shown to be negligible in EPI-based MRCDI when one slice was acquired. The robustness to physiological noise is a result of the measurement design. With sufficiently high temporal resolution and alternating current directions, the subtraction of two consecutive images acts as a high-pass filter removing any slowly varying signal changes from either physiological noise or scanner instability. Further averaging multiple measurements reduces any noise not correlated with the injected current.

Although physiological noise correction has proven not to be necessary when all measurements in one slice are fully acquired before moving on to the next slice, the anal-

ysis of the influence of physiological noise on EPI-based MRCDI data given in this thesis can still be valuable if other acquisition schemes are of interest.

6.2 EPI-based MRCDI

Low-frequency noise present in previously published MGRE-based MRCDI is not present in EPI-based MRCDI. This is evident from the data presented in the manuscript in Appendix A. A simulation study with added noise from the EPI and MGRE sequences revealed that EPI outperforms the MRGE sequence when it comes to optimization of conductivities based on the magnetic fields. However in the simulation study the systematic difference between the head model and the subject's actual head is not present. Therefore the simulation study only reveals the error in the relative conductivity estimates caused by the noise in the measurement data, and not due to differences in the model and the real head. In the experiment with injected currents the difference between measured and simulated magnetic fields was interestingly larger than the difference between measurements with different MR sequences. The error was for all subjects consistently larger for the RL montage than for the AP.
Although the final aim of MRCDI in relation to computational head models is to estimate subject-specific conductivities, the difference between measurements and simulation of magnetic fields is still too large to be caused by wrong conductivities only. This has proven that MRCDI is capable of providing valuable insight into how computational volume conductors of the human head can be improved to be closer to reality.

6.3 Low-conductivity lead wires

Stray magnetic fields from the lead wires were identified as a predominant source of errors in MRCDI by Göksu et al. [28]. They proposed to use a stray field correction method by tracking the leads and estimating the resulting fields using Biot-Savart law. To reduce errors in the correction caused by inaccurate lead tracking or subject motion it is preferable to align the leads away from the subjects' brain in the z direction of the MR scanner. However, due to safety reasons when copper leads are used in the scanner, some manufacturers of MR compatible neurostimulators have strict

requirements on the positioning of the leads, which makes optimal lead placement for MRCDI problematic. Additionally, safety resistors used in the copper leads limit the maximum injection current during MRI. Low-conductivity silicone rubber was used to create lead wires to reduce the safety risk in the scanner. The leads can be more freely positioned in the MR scanner without concerns for safety. Additionally the total impedance of the leads was lower than the impedance of the safety resistors allowing for higher stimulation currents.

6.4 Future perspectives

To expand the usefulness of MRCDI, increasing volume coverage is desirable. MRCDI suffers from low SNR of the magnetic field measurements requiring long scan times. Simultaneous multi-band (MB) [45] is a good candidate to increase volume coverage without increasing measurement time and noise level. In MB multiple slices are excited and acquired simultaneously and separated in post processing. To avoid increase in the noise when using MB, the acquired slices have to be sufficiently far apart. MB has been attempted for MRCDI with a MGRE sequence where 8 slices were simultaneously acquired [30]. The conference abstract presented no noise analysis to validate that MB was beneficial in the given case. Additionally measured magnetic fields were far from expected, most likely due to excessive noise in the measurements. To ensure that MB is beneficial, a systematic analysis of the noise in a single slice experiment compared to the noise in a MB experiments with varying amount of slices and distances between slices should be performed.

A GRE-EPI sequence was used in the thesis. The choice to use a GRE-EPI sequence instead of a SE-EPI sequence was based on the study by Göksu et al. [21] where they demonstrated that SE sequences are less efficient for MRCDI due to the long dead time required for the longitudinal magnetization to recover. The dead time can be used beneficially to acquire additional slices and thereby increase volume coverage. However, the increase in T_R might make the SE-EPI less robust to physiological noise. The optimal EPI sequence for volume coverage, both in terms of efficiency and robustness to physiological noise should therefore be systematically studied.

The manuscript in Appendix A presents sufficient evidence that current MRCDI meth-

ods can provide useful insight about the systematic errors in the computational head models. However, fitting all tissue conductivities blindly as done in the manuscript is not the optimal way to identify the errors. A more systematic approach analysing how each tissue conductivity changes the magnetic fields in a desired way is a more appropriate method to identify possible improvements.

Bibliography

[1] M. A. Nitsche and W. Paulus, "Excitability changes induced in the human motor cortex by weak transcranial direct current stimulation," *The Journal of Physiology*, vol. 527, pp. 633–639, 9 2000.

[2] A. Brunoni, M. A. Nitsche, and C. Loo, *Transcranial Direct Current Stimulation in Psychiatric Disorders*. Springe Nature, 2 ed., 2021.

[3] J. C. Horvath, J. D. Forte, and O. Carter, "Evidence that transcranial direct current stimulation (tDCS) generates little-to-no reliable neurophysiologic effect beyond MEP amplitude modulation in healthy human subjects: A systematic review," *Neuropsychologia*, vol. 66, pp. 213–236, 2015.

[4] A. N. Karabanov, G. B. Saturnino, A. Thielscher, and H. R. Siebner, "Can transcranial electrical stimulation localize brain function?," *Frontiers in Psychology*, vol. 10, no. FEB, 2019.

[5] A. Thielscher, A. Antunes, and G. B. Saturnino, "Field modeling for transcranial magnetic stimulation: A useful tool to understand the physiological effects of TMS?," *Proceedings of the Annual International Conference of the IEEE Engineering in Medicine and Biology Society, EMBS*, vol. 2015-Novem, pp. 222–225, 2015.

[6] G. B. Saturnino, A. Thielscher, K. H. Madsen, T. R. Knösche, and K. Weise, "A principled approach to conductivity uncertainty analysis in electric field calculations," *NeuroImage*, vol. 188, pp. 821–834, 3 2019.

[7] R. P. Henderson and J. G. Webster, "An Impedance Camera for Spatially Specific Measurements of the Thorax," *IEEE Transactions on Biomedical Engineering*, vol. 25, no. 3, pp. 250–254, 1978.

[8] M. Joy, G. Scott, and M. Henkelman, "In vivo detection of applied electric currents by magnetic resonance imaging," *Magnetic Resonance Imaging*, vol. 7, no. 1, pp. 89–94, 1989.

[9] N. Zhang, "Electrical impedance tomography based on current density imaging," Master's thesis, MSc Thesis University of Toronto, Toronto, Sept. 1992.

[10] D. G. Beetner, S. Kapoor, S. Manjunath, X. Zhou, and W. V. Stoecker, "Differentiation among basal cell carcinoma, benign lesions, and normal skin using electric impedance," *IEEE Transactions on Biomedical Engineering*, vol. 50, no. 8, pp. 1020–1025, 2003.

[11] M. Kranjc, F. Bajd, I. Serša, and D. Miklavčič, "Magnetic resonance electrical impedance tomography for measuring electrical conductivity during electroporation," *Physiological Measurement*, vol. 35, no. 6, pp. 985–996, 2014.

[12] R. J. Sadleir, F. Fu, C. Falgas, S. Holland, M. Boggess, S. C. Grant, and E. J. Woo, "Direct detection of neural activity in vitro using magnetic resonance electrical impedance tomography (MREIT)," *NeuroImage*, vol. 161, pp. 104–119, 2017.

[13] G. C. Scott, M. L. G. Joy, R. L. Armstrong, and A. M. Henkelman, "Sensitivity of Magnetic-Resonance Current-Density Imaging," *Journal of Magnetic Resonance*, vol. 97, p. 235254, 1992.

[14] C. Park, B. I. Lee, O. Kwon, and E. J. Woo, "Measurement of induced magnetic flux density using injection current nonlinear encoding (ICNE) in MREIT," *Physiological Measurement*, vol. 28, no. 2, pp. 117–127, 2007.

[15] Y. Q. Han, Z. J. Meng, W. C. Jeong, Y. T. Kim, A. S. Minhas, H. J. Kim, H. S. Nam, O. Kwon, and E. J. Woo, "MREIT conductivity imaging of canine head us-

ing multi-echo pulse sequence," *Journal of Physics: Conference Series*, vol. 224, no. 1, 2010.

[16] H. S. Nam and O. I. Kwon, "Optimization of multiply acquired magnetic flux density Bz using ICNE-Multiecho train in MREIT," *Physics in Medicine and Biology*, vol. 55, no. 9, pp. 2743–2759, 2010.

[17] S. H. Oh, B. I. Lee, E. J. Woo, S. Yeol Lee, K. Tae Seong, K. Ohin, and J. K. Seo, "Electrical conductivity images of biological tissue phantoms in MREIT," *Physiological Measurement*, vol. 26, no. 2, 2005.

[18] M. N. Kim, T. Y. Ha, E. J. Woo, and O. I. Kwon, "Improved conductivity reconstruction from multi-echo MREIT utilizing weighted voxel-specific signal-to-noise ratios," *Physics in Medicine and Biology*, vol. 57, no. 11, pp. 3643–3659, 2012.

[19] A. S. Minhas, E. J. Woo, and S. Y. Lee, "Magnetic flux density measurement with balanced steady state free precession pulse sequence for MREIT: A simulation study," *Proceedings of the 31st Annual International Conference of the IEEE Engineering in Medicine and Biology Society: Engineering the Future of Biomedicine, EMBC 2009*, pp. 2276–2278, 2009.

[20] H. Lee, W. C. Jeong, H. J. Kim, E. J. Woo, and J. Park, "Alternating steady state free precession for estimation of current-induced magnetic flux density: A feasibility study," *Magnetic Resonance in Medicine*, vol. 75, pp. 2009–2019, 5 2016.

[21] C. Göksu, K. Scheffler, P. Ehses, L. G. Hanson, and A. Thielscher, "Sensitivity analysis of magnetic field measurements for magnetic resonance electrical impedance tomography (MREIT)," *Magnetic Resonance in Medicine*, vol. 79, no. 2, pp. 748–760, 2018.

[22] M. J. Hamamura and L. T. Muftuler, "Fast imaging for magnetic resonance electrical impedance tomography," *Magnetic Resonance Imaging*, vol. 26, no. 6, pp. 739–745, 2008.

[23] J. K. Seo, D. H. Kim, J. Lee, O. I. Kwon, S. Z. Sajib, and E. J. Woo, "Electrical tissue property imaging using MRI at dc and Larmor frequency," *Inverse Problems*, vol. 28, no. 8, 2012.

[24] M. V. Jog, R. X. Smith, K. Jann, W. Dunn, B. Lafon, D. Truong, A. Wu, L. Parra, M. Bikson, and D. J. J. Wang, "In-vivo Imaging of Magnetic Fields Induced by Transcranial Direct Current Stimulation (tDCS) in Human Brain using MRI," *Scientific Reports*, vol. 6, p. 34385, 12 2016.

[25] M. Jog, K. Jann, L. Yan, Y. Huang, L. Parra, K. Narr, M. Bikson, and D. J. Wang, "Concurrent Imaging of Markers of Current Flow and Neurophysiological Changes During tDCS," *Frontiers in Neuroscience*, vol. 14, 4 2020.

[26] A. K. Kasinadhuni, A. Indahlastari, M. Chauhan, M. Schär, T. H. Mareci, and R. J. Sadleir, "Imaging of current flow in the human head during transcranial electrical therapy," *Brain Stimulation*, vol. 10, no. 4, pp. 764–772, 2017.

[27] M. Chauhan, A. Indahlastari, A. K. Kasinadhuni, M. Schar, T. H. Mareci, and R. J. Sadleir, "Low-Frequency Conductivity Tensor Imaging of the Human Head In Vivo Using DT-MREIT: First Study," *IEEE Transactions on Medical Imaging*, vol. 37, no. 4, pp. 966–976, 2018.

[28] C. Göksu, L. G. Hanson, H. R. Siebner, P. Ehses, K. Scheffler, and A. Thielscher, "Human in-vivo brain magnetic resonance current density imaging (MRCDI)," *NeuroImage*, vol. 171, no. December 2017, pp. 26–39, 2018.

[29] C. Göksu, K. Scheffler, F. Gregersen, H. H. Eroğlu, R. Heule, H. R. Siebner, L. G. Hanson, and A. Thielscher, "Sensitivity and resolution improvement for in vivo magnetic resonance current-density imaging of the human brain," *Magnetic Resonance in Medicine*, no. March, pp. 1–16, 2021.

[30] M. Chauhan, S. Sahu, S. Zaman, K. Sajib, E. Boakye, M. Schär, and R. J. Sadleir, "Current Density Measurements in the Human Brain in-vivo during TES treatment , using Multi- Band methods," *ISMRM 28th Annual Meeting & Exhibition*, 2020.

[31] C. Göksu, K. Scheffler, H. R. Siebner, A. Thielscher, and L. G. Hanson, "The stray magnetic fields in Magnetic Resonance Current Density Imaging (MR-CDI)," *Physica Medica*, vol. 59, no. February, pp. 142–150, 2019.

[32] R. W. Brown, Y. C. N. Cheng, M. E. Haacke, M. R. Thompson, and R. Venkatesan, *Magnetic Resonance Imaging: Physical Principles and Sequence Design*. John Wiley & Sons, Inc., second ed., 2014.

[33] H. Gudbjartsson and S. Patz, "The Rician distribution of noisy MRI data (vol 34, pg 910, 1995)," *Magnetic Resonance in Medicine*, vol. 36, no. 2, p. 332, 1996.

[34] E. J. Woo and J. K. Seo, "Magnetic resonance electrical impedance tomography (MREIT) for high-resolution conductivity imaging," *Physiological Measurement*, vol. 29, no. 10, 2008.

[35] J. K. Seo and E. J. Woo, "Magnetic Resonance Electrical Impedance Tomography (MREIT)," *SIAM Review*, vol. 53, no. 1, pp. 40–68, 2011.

[36] H. H. Eroğlu, O. Puonti, C. Göksu, F. Gregersen, H. R. Siebner, L. G. Hanson, and A. Thielscher, "On the Reconstruction of Magnetic Resonance Current Density Images of the Human Brain: Pitfalls and Perspectives," *NeuroImage*, vol. 243, no. July, 2021.

[37] G. E. Hagberg, M. Bianciardi, V. Brainovich, A. M. Cassarà, and B. Maraviglia, "The effect of physiological noise in phase functional magnetic resonance imaging: from blood oxygen level-dependent effects to direct detection of neuronal currents," *Magnetic Resonance Imaging*, vol. 26, no. 7, pp. 1026–1040, 2008.

[38] X. Hu, T. H. Le, T. Parrish, and P. Erhard, "Retrospective estimation and correction of physiological fluctuation in functional MRI," *Magnetic Resonance in Medicine*, vol. 34, pp. 201–212, 8 1995.

[39] G. H. Glover, T.-Q. Li, and D. Ress, "Image-based method for retrospective correction of physiological motion effects in fMRI: RETROICOR," *Magnetic Resonance in Medicine*, vol. 44, pp. 162–167, 7 2000.

[40] C. Caballero-Gaudes and R. C. Reynolds, "Methods for cleaning the BOLD fMRI signal," *NeuroImage*, vol. 154, pp. 128–149, 7 2017.

[41] G. E. Hagberg, M. Bianciardi, V. Brainovich, A. M. Cassara, and B. Maraviglia, "Phase stability in fMRI time series: Effect of noise regression, off-resonance correction and spatial filtering techniques," *NeuroImage*, vol. 59, pp. 3748–3761, 2 2012.

[42] L. P. Panych and B. Madore, "The physics of MRI safety," *Journal of Magnetic Resonance Imaging*, vol. 47, pp. 28–43, 1 2018.

[43] IEC, "Particular requirements for the basic safety and essential performance of magnetic resonance equipment for medical diagnosis. IEC 60601-2-33," 2010.

[44] M. Kozlov, R. Müller, A. Pampel, B. Kalloch, N. Weiskopf, and H. E. Möller, "RF Safety of Transcranial Direct Current Stimulation Equipment during MRI," *Poster presented at Joint Annual Meeting ISMRM-ESMRMB 2018, Paris, France*, 2018.

[45] D. J. Larkman, J. V. Hajnal, A. H. Herlihy, G. A. Coutts, I. R. Young, and G. Ehnholm, "Use of multicoil arrays for separation of signal from multiple slices simultaneously excited," *Journal of Magnetic Resonance Imaging*, vol. 13, no. 2, pp. 313–317, 2001.

Appendices

APPENDIX A

Noise reduction in human in-vivo magnetic resonance current density imaging (MRCDI) using echo planar imaging

The following manuscript is in preparation.

Noise reduction in human in-vivo magnetic resonance current density imaging (MRCDI) using echo planar imaging

Fróði Gregersen[a,b,c,d], Hasan H. Eroğlu[a,b], Cihan Göksu[b,e], Oula Puonti[b], Rong Xue[c,f,g], Axel Thielscher[a,b,1], and Lars G. Hanson[a,b,1]✉

[a]Section for Magnetic Resonance, DTU Health Tech, Technical University of Denmark, Kgs Lyngby, Denmark
[b]Danish Research Centre for Magnetic Resonance, Centre for Functional and Diagnostic Imaging and Research, Copenhagen University Hospital Amager and Hvidovre, Copenhagen, Denmark
[c]Sino-Danish Center for Education and Research, Aarhus, Denmark
[d]University of Chinese Academic of Sciences, Beijing, 100049, China
[e]High-Field Magnetic Resonance Center, Max-Planck-Institute for Biological Cybernetics, Tübingen, Germany
[f]State Key Laboratory of Brain and Cognitive Science, Beijing MRI Center for Brain Research, Institute of Biophysics, Chinese Academy of Sciences, Beijing, 100101, China
[g]Beijing Institute for Brain Disorders, Beijing, 100053, China

Volume conductor models of the human head are frequently used to estimate the electric fields in non-invasive brain stimulation or for source localization in electro- and magnetoencephalography. Validation of the models is important to provide reliable results. Magnetic resonance current density imaging (MRCDI) has the potential to act as a non-invasive validation method. However, spatial low-frequency noise in previously reported human in-vivo MRCDI experiments impedes the accuracy of the measurements. An EPI sequence was used for fast imaging of the current-induced magnetic field measurements to increase the robustness to physiological noise. Noise floor measurements from the previously used multi-echo gradient echo (MGRE) and the EPI sequence were used in simulation to evaluate the effect the noise has on current density estimation in the head model. Conductivity optimization based on simulated and measured magnetic fields was performed for both sequence types. It was shown that noise floor measurements with the MGRE sequence has larger impact on the simulation than the EPI sequence. However, differences between simulations and measurements were greater than differences between measurements with the two sequences, suggesting that current MRCDI methods can be used to improve computational head models.

magnetic resonance current density imaging (MRCDI) | echo planar imaging (EPI) | head modelling | transcranial Electric Stimulation (TES)

Correspondence: ***larsh@drcmr.dk (L.G. Hanson)***
[1] These authors contributed equally to this work

Introduction

Computational models of the human head used to estimate current density ($\boldsymbol{J}$) or electric fields distributions in the brain serve as an important tool for target localization in transcranial brain stimulation or source localization in electro- and magnetoencephalography. However, the accuracy of the head models have to be verified to produce reliable results. Recently, the possibility to non-invasively measure the current-induced magnetic fields in the human brain by MRI has been demonstrated (1–4). The technique termed magnetic resonance current density imaging (MRCDI) (5) measures phase perturbations of the MR images caused by the current-induced magnetic fields. MRCDI has great potential to serve as a safe and non-invasive method to validate the accuracy of computational head models. Although the recent studies can reliably detect current-induced magnetic fields in the human brain, spatial low-frequency noise is present in the reconstructed magnetic field measurements. All of the previous studies used multi-echo gradient echo (MGRE) sequences.
In this study, we demonstrate the possibility to use echo planar imaging (EPI) to resolve the issue of low-frequency noise in the magnetic field measurements. We use a recently suggested method for conductivity optimization based on measured and simulated magnetic fields (6). We evaluate the performance of the EPI method by using conductivity optimization and compare to our previously developed acquisition weighted (MGRE) sequence (4).

Methods

Data acquisitions

Four healthy volunteers were scanned in a 3T MR scanner (MAGNETOM Prisma, Siemens Healthcare, Erlangen, Germany). Written informed consent was obtained from the participants prior to the scans and they were screened for contraindications to MRI and transcranial electric stimulation (TES). The study complied with the Helsinki declaration on human experimentation and was approved by the Ethics Committee of the Capital Region of Denmark.
MRCDI data was acquired with both an MGRE sequence (4) and with an EPI sequence provided by the Center for Magnetic Resonance Research (CMRR, Minneapolis, Minnesota, USA). The imaging parameters for the MGRE sequence were T_R = 80 ms, T_E = 5.6, 14.4, 23.2, 32, 40.8, 49.6, 58.4, 67.2 ms, Flip angle 30°, FOV 224 × 183 mm^2, matrix size 176 × 144, acquisition time 4:20 min. The same slice was scanned twice, resulting in a total acquisition time of 8:40 min. For the EPI sequence the imaging parameters were T_R = 120 ms, T_E = 25.6, 63.48 ms, Flip angle 30°, FOV 225 × 190 mm^2, matrix size 76 × 64. Two k-space transversals were performed per excitation to reduce geometric distortion due to low bandwidth in the phase encoding direction in EPI. B_0 field maps were also acquired prior to EPI to perform distortion correction on the measured magnetic field images (7).

The FUGUE toolbox in FSL was used to perform the distortion correction.

A neurostimulator (DC-STIMULATOR MR, neuroCare Group GmbH, München, Germany) and low-conductivity silicon rubber leads and surface electrodes (8) optimized for MRCDI were used for current injection. The neurostimulator was controlled by a signal generator reading trigger pulses from the MR scanner to synchronize the current injection with the MR pulse sequences. Alternating current injection direction was used for each consecutive EPI measurement. The current-induced magnetic fields (B_z) were then calculated from the difference in the phase images divided by the phase sensitivity of the sequence as $B_z = (\varphi^+ - \varphi^-)/(2\gamma T_E)$, where gamma is the gyromagnetic ratio of protons. B_z from separate echoes were combined based on the variance of B_z for each echo estimated from the SNR in the magnitude image (9).

One slice with 4334 measurements resulting in an acquisition time of 8:40 min was acquired with the EPI sequence to time-match it to the MGRE acquisition. Additionally, 5 slices with 1000 measurements (2 min acquisition time per slice) were acquired to obtain a larger brain coverage. The slices were 1 cm apart. Each slice was fully acquired separately instead of performing interleaved acquisition to maintain the robustness to physiological noise. For more details on the acquisition weighted MGRE sequence see (4). Apart from using the FSL tool BET (10) to mask B_z measurements a $T2^*$ mask calculated from the dual-echo EPI measurements with 30 ms threshold was also used to exclude low signal areas in the EPI images.

A 3D structural image was acquired with the pointwise encoding time reduction with radial acquisition (PETRA) sequence (11) prior to MRCDI acquisition. The PETRA sequence is an ultra short echo time sequence capable of imaging the silicone rubber lead wires. The leads were manually tracked and the Biot-Savart law was used to calculate lead stray fields. The stray fields were then subtracted from the MRCDI measurements (12).

Computational head models and FEM simulation

Automatic head segmentation using T1- and T2-weighted MR images was performed to create individual volume conductor models of the subjects' heads (13). The Finite Element Method (FEM) implemented in SimNIBS 3.1 (14) was used to calculate the current density in the head for a given electrode montage and injection current strength. The magnetic flux density $\boldsymbol{B}$ is calculated from the current density using a fast Fourier transform-based method of solving the Biot-Savart integral (15).

Optimization of conductivities

To optimize the tissue conductivities in the simulation, a constrained optimization problem was formulated with the aim of minimizing the difference between the simulated (B_z^s) and measured (B_z^m) magnetic flux densities. The optimization problem was formulated as

$$\min_{\sigma} \quad \delta_{B_z} = \sqrt{\frac{\sum_{i=1}^{N}(B_z^s(\sigma,i) - B_z^m(i))^2}{\sum_{i=1}^{N}(B_z^m(i))^2}} \times 100\% \qquad \textbf{(1)}$$
$$\text{s.t.} \quad \sigma_{low} \leq \sigma \leq \sigma_{high} \quad \text{and} \quad \sigma_{WM} \leq \sigma_{GM}\,,$$

with the tissue types being white matter (WM), gray matter (GM), cerebrospinal fluid (CSF), scalp, compact bone (CB) and spongy bone (SB). The bounds (σ_{low} and σ_{high}) are [$0.1 < \sigma_{WM} < 0.4$ S/m, $0.1 < \sigma_{GM} < 0.6$ S/m, $1.2 < \sigma_{CSF} < 1.8$ S/m, $0.2 < \sigma_{Scalp} < 1$ S/m, $0.004 < \sigma_{CB} < 0.012$ S/m, $0.015 < \sigma_{SB} < 0.04$ S/m]. For a fast evaluation of B_z^s for each new set on conductivities a non-intrusive general polynomial chaos (gPC) expansion was used. For a detailed description on the optimization and the gPC, please refer to (6) and (16).

Experiment 1: Verifying EPI sequence with a wire loop

The first experiment was performed to verify that the phase sensitivity to the current-induced magnetic field was as expected with the employed EPI sequence. A wire loop was placed around the subjects head. 2 mA currents were passed through the loop generating a magnetic field in the brain detectable by MRCDI. The lead wire was imaged with the PETRA sequence. After manual tracking, the Biot-Savart law was used to estimate the field created in the imaged brain slices. The simulated field was subtracted from the measured field, and the residuals were used to asses the quality and accuracy of the measurements.

One subject was used for this experiment. Five 3 mm thick slices with 1 cm distance between each slice were acquired. Each slice took 2 minutes to acquire resulting in a total acquisition time of 10 minutes.

Experiment 2: Optimization of conductivities with added noise floors

In this experiment, we tested how much the noise in the MRCDI measurements impacts the optimization of conductivities. This was done by simulating B_z^s with a right-left electrode montage and with conductivities slightly different from the standard conductivities in SimNIBS. Noise floors from measurements were then added to the simulated B_z^s before conductivity optimization. In this method, the ground truth of the conductivities is known, and therefore the final error in the optimization can be calculated. However, when the electric potential at the electrodes is unknown, the conductivities can be scaled with the same constant and still give rise to the same current density and magnetic field in the brain. Therefore the errors are more reliably estimated by taking the difference between the true ($\boldsymbol{J}^{true}$) and reconstructed ($\boldsymbol{J}^{rec}$) current density. The error is defined as the relative root mean square error

$$\delta_{\boldsymbol{J}} = \sqrt{\frac{\sum_{i=1}^{N}\left|\boldsymbol{J}^{rec}(i) - \boldsymbol{J}^{true}(i)\right|^2}{\sum_{i=1}^{N}\left|\boldsymbol{J}^{true}(i)\right|^2}} \times 100\%\,, \qquad \textbf{(2)}$$

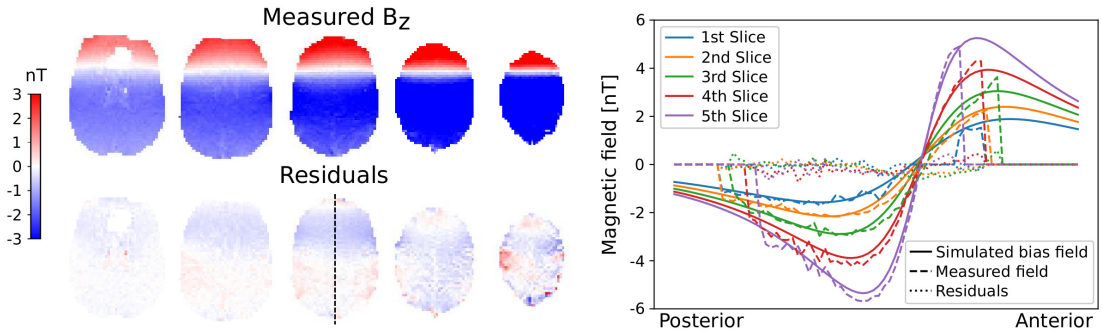

Fig. 1. Results from experiment 1 with a current carrying loop around the subjects head. The brain slices in the top show the measured magnetic field and the slices at the bottom show the stray field corrected data. The figure on the right is a projection through the center of each slice from anterior to posterior showing the simulated bias field (solid lines), measured field (dashed lines) and the residuals (dotted lines).

where i indicates each voxel. The conductivities used to create B_z^s were [$\sigma_{WM} = 0.11$ S/m, $\sigma_{GM} = 0.23$ S/m, $\sigma_{CSF} = 1.6$ S/m, $\sigma_{Scalp} = 0.3$ S/m, $\sigma_{CB} = 0.01$ S/m, $\sigma_{SB} = 0.03$ S/m], while the standard conductivities in SimNIBS were used as the initial conductivities in the optimization [$\sigma_{WM} = 0.126$ S/m, $\sigma_{GM} = 0.275$ S/m, $\sigma_{CSF} = 1.654$ S/m, $\sigma_{Scalp} = 0.465$ S/m, $\sigma_{CB} = 0.008$ S/m, $\sigma_{SB} = 0.025$ S/m]. The conductivity optimization was performed with the resolution of the used noise floor measurements, which was different for EPI and MGRE. However, the current densities ($\boldsymbol{J}^{true}$ and $\boldsymbol{J}^{rec}$) were calculated with the same resolution after obtaining the conductivity estimates. The current density error was calculated for all tissue types with the lowest slice in the 5 slice EPI data acting as the lower bound since the current density in the lower part of the head model is of less interest. No upper bound was used.

The noise floors from both the EPI and MGRE sequence were added to the simulation. One brain slice was measured with the MGRE sequence with a total acquisition time of 8:40 min. A time-matched EPI measurement was performed where the same slice was measured. Additionally, to get a larger brain coverage 5 slices were also measured with the EPI sequence where the acquisition time was 2 min per slice.

Experiment 3: Optimization of conductivities with injected current measurements

For the third experiment, we performed MRCDI measurements with 1mA currents injected in synchrony with the MR sequence using a right-left (RL) and an anterior-posterior (AP) electrode montage. As in the previous experiment three measurements were performed, namely one brain slice with the MGRE sequence, one time-matched slice with EPI and 5 slices with EPI with 2 min acquisition time per slice. The measured data (B_z^m) was used in the optimization of conductivities according to equation 1, where the initial conductivities are the same as given in the previous experiment. In this case, the ground truth is unknown, and δ_{B_z} indicates a difference between measured and simulated B_z. The difference was evaluated before ($\delta_{B_z^{lit}}$) and after ($\delta_{B_z^{opt}}$) optimization, where the standard conductivities in SimNIBS were used to calculate the magnetic field before optimization.

Result

Experiment 1: Verifying EPI sequence with a wire loop

The results from the loop experiment are presented in figure 1. The residuals reveal that there is a good correspondence between the B_z^m calculated from phase difference images and the estimated stray field calculated with Biot-Savart law. However, some remaining residuals still exist, which can have multiple causes, such as error in the cable tracking or subject movement during scanning. Sulci regions, especially in the upper slices, are also slightly visible, which can be caused by flow of the CSF.

Experiment 2: Optimization of conductivities with added noise floors

The results from experiment 2 are presented in figure 2. Although the noise floor images for EPI and MGRE cannot be directly compared due to the different voxel size and unknown point spread functions, it is clear that the MGRE sequence has stronger low-frequency noise patterns that do not exist in the EPI images. On the other hand, the simulation domain for the EPI sequence is lower, which could result in loss of high-frequency structures in the magnetic field result in larger errors. However, it is clear from the calculated current density error that the optimization with noise from the EPI data outperforms the optimization with noise from the MGRE data. Even when the optimization is performed for single slices with noise added from the 2 min EPI data (last box in the box plot), EPI outperforms MGRE. The best result is obtained when the optimization is done for 5 slices simultaneously.

Experiment 3: Optimization of conductivities with injected current measurements

The data from experiment 3 with current injection is presented in figure 3 and 4. In figure 3 one dataset with 5

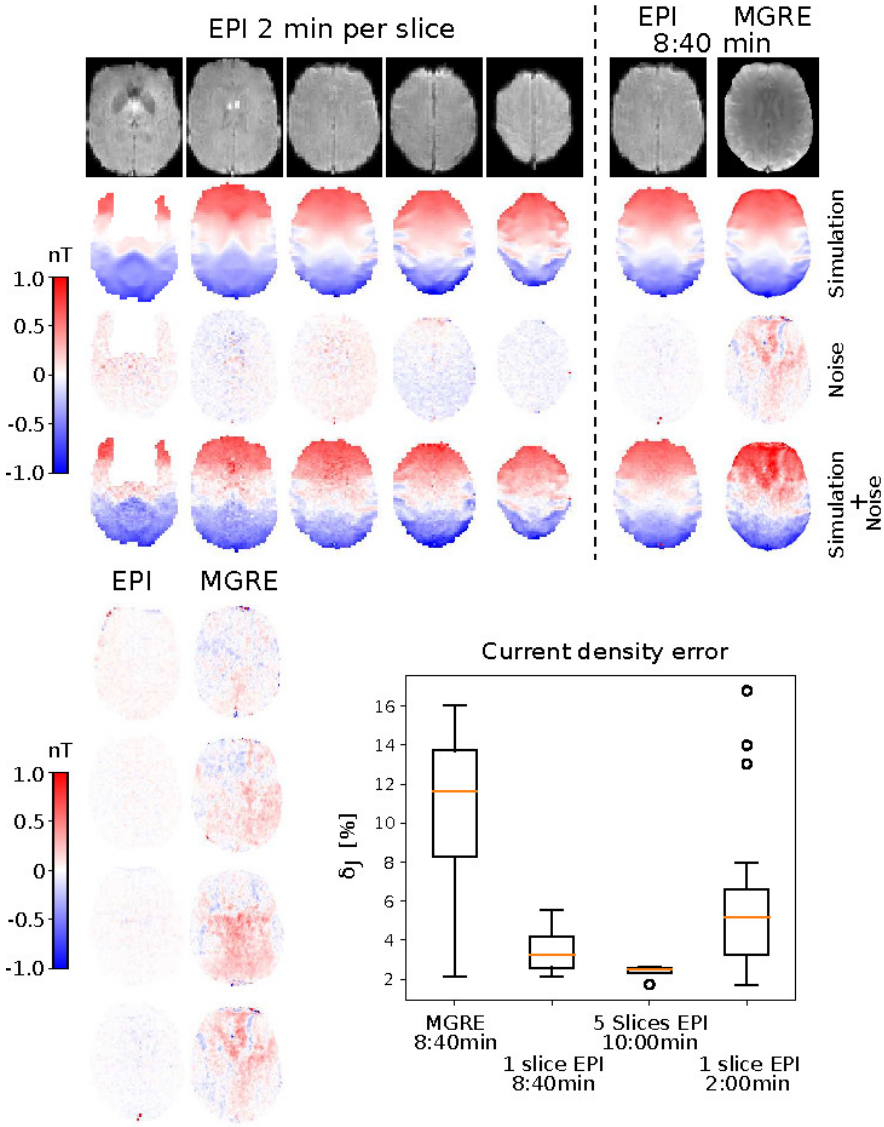

Fig. 2. Results from experiment 2 with noise floor from measurements added to the simulation. The top rows are the magnitude images, simulated magnetic fields, noise in the measurements, and the simulated data with added measurement noise for EPI and MGRE from one subject. The EPI data to the right is time-matched to the MGRE data. The noise measurements at the bottom are from all four subjects for MGRE (right) and time-matched EPI (left). The box plot shows the error in current density after optimizing the conductivities with the noisy simulations.

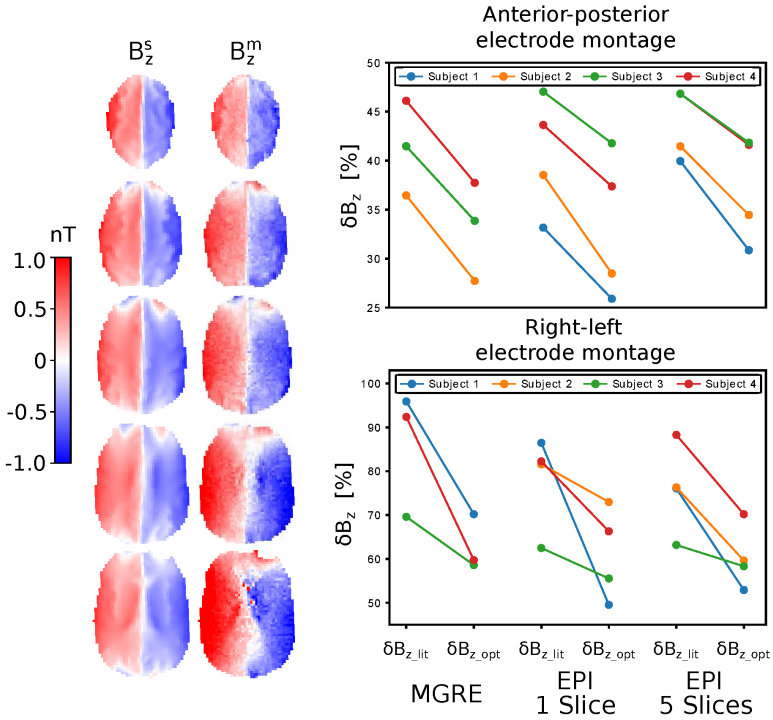

Fig. 3. Measured magnetic fields for a 5 slice EPI experiment are presented together with the corresponding simulated magnetic field on the left. The top slices show extraordinary similarities between simulation and measurement. The plots on the right show the relative difference between simulated and measured magnetic fields before ($\delta_{B_z^{lit}}$) and after ($\delta_{B_z^{opt}}$) optimization (see equation 1) with AP and RL electrode montages. (AP data is missing for subject 1 and RL data is missing for subject 2 for the MGRE sequence)

slices acquired with the EPI sequence is presented together with the corresponding simulations. Extraordinary similarity between the simulation and measurement is present in the top slices. The larger differences for the lower slices can be caused by inaccuracies in the measurements, such as insufficient lead wire correction, since these slices are closer to the leads. However, it can also be caused by systematic differences between the lower part of the head model and reality. The plots on the right in figure 3 shows that there is a very consistent difference between the errors for the RL and AP montage. Optimizing the conductivities has more influence on the RL data. Furthermore, there is very little difference between the magnetic field measurements acquired with the MGRE and the EPI sequence. The difference between RL and AP is also clear in the data shown to the right in figure 4. After optimization, the magnetic field for the RL montage changes a lot more than for the AP montage. The final conductivities after optimization are presented in figure 4. Even though the conductivities cannot be quantified, as they can be scaled with a common scaling factor leading to the same magnetic field, the final conductivity values still hold useful information about the discrepancy between simulated and measured magnetic fields.

Discussion

Two previous studies have attempted to measure current-induced magnetic fields with EPI (17, 18). However, lead stray field correction was not performed, leading to large differences between simulated and measured magnetic fields. Additionally, with the aim of mapping direct currents constant over a period of minutes, the method is not robust to physiological noise or hardware instabilities. We have demonstrated, with the first reliable human in-vivo EPI-based MRCDI measurements, that EPI is a good alternative to MGRE, if low-frequency noise patterns in the magnetic field measurements are an issue. Due to the rapid sampling of the images, physiological noise has less effect on the EPI acquired magnetic fields. However, a well known problem for EPI is susceptibility induced signal loss, especially for lower slices close to the paranasal sinuses. This is also a problem for MRCDI, where a long current injection and readout time is necessary. We masked out regions with low $T2^*$ (see figure 2) to avoid excessive noise in the magnetic field measurements. Geometrical distortion is also a well know issue for EPI sequences. We used a double-echo EPI sequence to increase the bandwidth per pixel in the phase encoding direction, resulting in less geometrical distortions. Additionally, EPI has lower resolution than MGRE. However, since

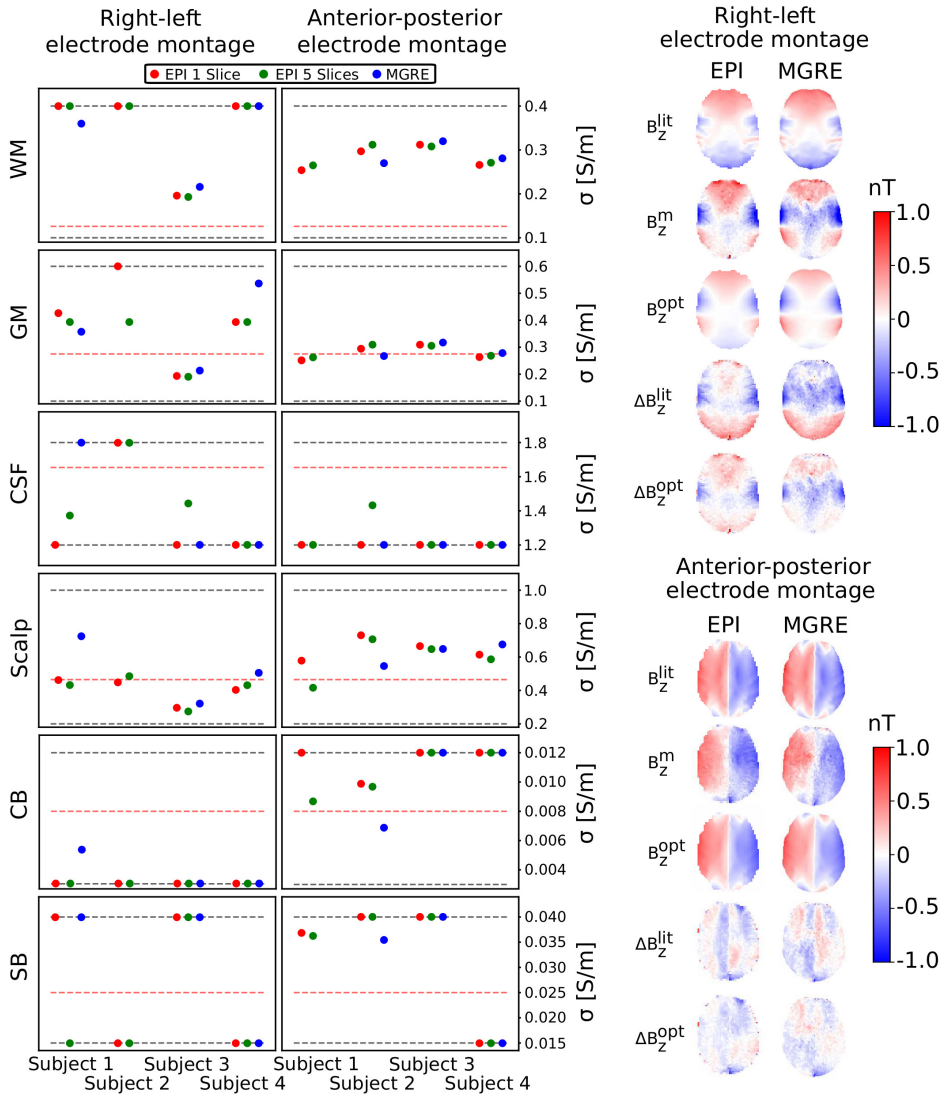

Fig. 4. The plots on the left show the final conductivity after optimization from the 1 slice EPI (red), 5 slices EPI (green), and MGRE (blue) for both the RL and AP electrode montage. The Black dotted lines are the upper and lower bounds used in the optimization algorithm, and the red dotted lines is the standard value in SimNIBS. An example dataset is shown on the right with both the 1 slice EPI sequence and MGRE, for both electrode montages. (AP data is missing for subject 1 and RL data is missing for subject 2 for the MGRE sequence)

the magnetic fields in the brain caused by injected currents are mainly low-frequency, the resolution is not a big issue for the method of optimizing conductivities based on the magnetic fields, as used in the article. This has been verified in preliminary assessment of the gPC components, as well as with simulations with varying resolution not provided here. This notion is also strengthened by our simulation experiments with added noise floors from measurements (figure 2). With the error in the current density estimation being largest for the MGRE sequence, it suggests that reducing the noise level, especially the low-frequency noise, is more important than having a high resolution.

In the experiments with injected currents, the agreement between simulation and measurements is much better for an AP montage than for the RL montage. This is consistent for all subjects and all measurements. The high discrepancy for the RL montage can provide valuable insight into how the head models can be improved to increase the accuracy of the current flow estimation in the brain, for example by adding more tissue types to mitigate the difference. This discrepancy is most likely caused by imperfections in the head model, since no systematic difference is expected for measurements with different electrode montages.

The errors between simulations and measurements are at the same level for all measurements with a given electrode montage, suggesting that the difference between simulation and measurements is greater than the error caused by noise in the measurements. This demonstrates that current MRCDI methods are sensitive enough to improve the computational head models, not only by optimizing the conductivities but more importantly by providing valuable information on how the head models can be improved.

Although the final conductivities presented in figure 4 cannot be taken at face value, they can be used as indicators for how the head models are different from reality and guide their improvements. For example, the conductivities for CSF reaching the lower bounds, especially consistent for the AP montage, is in agreement with a recently published study (19) suggesting that CSF should be simulated with a lower conductivity (0.85 S/m) to emulate the meningeal layers present in the CSF. However, a more systematic approach has to be adapted to study why the measured and simulated magnetic fields are more similar for the AP montage than the RL montage and how the head models can be improved to reduce the error.

Conclusions

We have shown that low-frequency noise floors that are usually present in MGRE-based MRCDI data can be avoided by using EPI acquisition instead. The higher noise floors in MGRE have a negative impact on conductivity optimization where the difference between measured and simulated magnetic fields are minimized. However, we also showed that the difference between simulated and measured magnetic fields is comparable with EPI and MGRE acquired MRCDI data and consistent between subjects, indicating that MRCDI has great potential to improve computational head models.

ACKNOWLEDGEMENTS

This study was supported by the Lundbeck Foundation (grants R313-2019-622 and R244-2017-196 to AT and R288-2018-236 to CG), the Chinese National Major Scientific Equipment R&D Project (grant ZDYZ2010-2) and a PhD stipend of the Sino-Danish Center for Education and Research to FG.

Bibliography

1. A. K. Kasinadhuni, A. Indahlastari, M. Chauhan, Michael Schär, T. H. Mareci, and R. J. Sadleir. Imaging of current flow in the human head during transcranial electrical therapy. *Brain Stimulation*, 10(4):764–772, 2017. ISSN 18764754. doi: 10.1016/j.brs.2017.04.125.
2. Munish Chauhan, Aprinda Indahlastari, Aditya K. Kasinadhuni, Michael Schar, Thomas H. Mareci, and Rosalind J. Sadleir. Low-Frequency Conductivity Tensor Imaging of the Human Head In Vivo Using DT-MREIT: First Study. *IEEE Transactions on Medical Imaging*, 37(4): 966–976, 2018. ISSN 1558254X. doi: 10.1109/TMI.2017.2783348.
3. Cihan Göksu, Lars G. Hanson, Hartwig R. Siebner, Philipp Ehses, Klaus Scheffler, and Axel Thielscher. Human in-vivo brain magnetic resonance current density imaging (MRCDI). *NeuroImage*, 171(December 2017):26–39, 2018. ISSN 10959572. doi: 10.1016/j.neuroimage.2017.12.075.
4. Cihan Göksu, Klaus Scheffler, Fróði Gregersen, Hasan H. Eroğlu, Rahel Heule, Hartwig R. Siebner, Lars G. Hanson, and Axel Thielscher. Sensitivity and resolution improvement for in vivo magnetic resonance current-density imaging of the human brain. *Magnetic Resonance in Medicine*, (March):1–16, 2021. ISSN 0740-3194. doi: 10.1002/mrm.28944.
5. M Joy, G Scott, and M Henkelman. In vivo detection of applied electric currents by magnetic resonance imaging. *Magnetic Resonance Imaging*, 7(1):89–94, 1989. ISSN 0730725X. doi: 10.1016/0730-725X(89)90328-7.
6. Hasan H. Eroğlu, Oula Puonti, Cihan Göksu, Fróði Gregersen, Hartwig R. Siebner, Lars G. Hanson, and Axel Thielscher. On the Reconstruction of Magnetic Resonance Current Density Images of the Human Brain: Pitfalls and Perspectives. *NeuroImage*, 243(July), 2021. ISSN 1053-8119. doi: 10.1016/j.neuroimage.2021.118517.
7. Peter Jezzard and Robert S. Balaban. Correction for geometric distortion in echo planar images from B0 field variations. *Magnetic Resonance in Medicine*, 34(1):65–73, 1995. ISSN 15222594. doi: 10.1002/mrm.1910340111.
8. Fróði Gregersen, Cihan Göksu, Gregor Schaefers, Rong Xue, Axel Thielscher, and Lars G Hanson. Safety evaluation of a new setup for transcranial electric stimulation during magnetic resonance imaging. *Brain Stimulation*, 14(3):488–497, 5 2021. ISSN 1935861X. doi: 10.1016/j.brs.2021.02.019.
9. Hyun Soo Nam and Oh In Kwon. Optimization of multiply acquired magnetic flux density Bz using ICNE-Multiecho train in MREIT. *Physics in Medicine and Biology*, 55(9):2743–2759, 2010. ISSN 00319155. doi: 10.1088/0031-9155/55/9/021.
10. Stephen M. Smith. Fast robust automated brain extraction. *Human Brain Mapping*, 17(3): 143–155, 2002. ISSN 10659471. doi: 10.1002/hbm.10062.
11. David M Grodzki, Peter M Jakob, and Bjoern Heismann. Ultrashort Echo Time Imaging Using Pointwise Encoding Time Reduction With Radial Acquisition (PETRA). 518:510–518, 2012. doi: 10.1002/mrm.23017.
12. Cihan Göksu, Klaus Scheffler, Hartwig R. Siebner, Axel Thielscher, and Lars G. Hanson. The stray magnetic fields in Magnetic Resonance Current Density Imaging (MRCDI). *Physica Medica*, 59(February):142–150, 2019. ISSN 1724191X. doi: 10.1016/j.ejmp.2019.02.022.
13. Jesper D. Nielsen, Kristoffer H. Madsen, Oula Puonti, Hartwig R. Siebner, Christian Bauer, Camilla Gøbel Madsen, Guilherme B. Saturnino, and Axel Thielscher. Automatic skull segmentation from MR images for realistic volume conductor models of the head: Assessment of the state-of-the-art. *NeuroImage*, 174(August 2017):587–598, 2018. ISSN 10959572. doi: 10.1016/j.neuroimage.2018.03.001.
14. Axel Thielscher, Andre Antunes, and Guilherme B. Saturnino. Field modeling for transcranial magnetic stimulation: A useful tool to understand the physiological effects of TMS? *Proceedings of the Annual International Conference of the IEEE Engineering in Medicine and Biology Society, EMBS*, 2015-Novem:222–225, 2015. ISSN 1557170X. doi: 10.1109/EMBC.2015.7318340.
15. Hassan Yazdanian, Guilherme B. Saturnino, Axel Thielscher, and Kim Knudsen. Fast evaluation of the Biot-Savart integral using FFT for electrical conductivity imaging. *Journal of Computational Physics*, 411:109408, 2020. ISSN 10902716. doi: 10.1016/j.jcp.2020.109408.
16. Guilherme B. Saturnino, Axel Thielscher, Kristoffer H. Madsen, Thomas R. Knösche, and Konstantin Weise. A principled approach to conductivity uncertainty analysis in electric field calculations. *NeuroImage*, 188:821–834, 3 2019. ISSN 10959572. doi: 10.1016/j.neuroimage.2018.12.053.
17. Mayank V. Jog, Robert X. Smith, Kay Jann, Walter Dunn, Belen Lafon, Dennis Truong, Allan Wu, Lucas Parra, Marom Bikson, and Danny J. J. Wang. In-vivo Imaging of Magnetic Fields Induced by Transcranial Direct Current Stimulation (tDCS) in Human Brain using MRI. *Scientific Reports*, 6(1):34385, 12 2016. ISSN 2045-2322. doi: 10.1038/srep34385.
18. Mayank Jog, Kay Jann, Lirong Yan, Yu Huang, Lucas Parra, Katherine Narr, Marom Bikson, and Danny J.J. Wang. Concurrent Imaging of Markers of Current Flow and Neurophysiological Changes During tDCS. *Frontiers in Neuroscience*, 14, 4 2020. ISSN 1662453X. doi: 10.3389/fnins.2020.00374.
19. Jimmy Jiang, Dennis Q. Truong, Zeinab Esmaeilpour, Yu Huang, Bashar W. Badran, and Marom Bikson. Enhanced tES and tDCS computational models by meninges emulation. *Journal of Neural Engineering*, 17(1), 2020. ISSN 17412552. doi: 10.1088/1741-2552/ab549d.

APPENDIX B

Safety evaluation of a new setup for transcranial electric stimulation during magnetic resonance imaging

The following paper has been published in Brain Stimulation.

Brain Stimulation 14 (2021) 488–497

Contents lists available at ScienceDirect

Brain Stimulation

journal homepage: http://www.journals.elsevier.com/brain-stimulation

Safety evaluation of a new setup for transcranial electric stimulation during magnetic resonance imaging

Fróði Gregersen [a, b, c, h], Cihan Göksu [b, d], Gregor Schaefers [e, f], Rong Xue [g, h, i], Axel Thielscher [a, b, 1], Lars G. Hanson [a, b, *, 1]

[a] Section for Magnetic Resonance, DTU Health Tech, Technical University of Denmark, Kgs Lyngby, Denmark
[b] Danish Research Centre for Magnetic Resonance, Centre for Functional and Diagnostic Imaging and Research, Copenhagen University Hospital Amager and Hvidovre, Hvidovre, Denmark
[c] Sino-Danish Center for Education and Research, Aarhus, Denmark
[d] High-Field Magnetic Resonance Center, Max-Planck-Institute for Biological Cybernetics, Tübingen, Germany
[e] MRI-STaR-Magnetic Resonance Institute for Safety, Technology and Research GmbH, Gelsenkirchen, Germany
[f] MR:comp GmbH, MR Safety Testing Laboratory, Gelsenkirchen, Germany
[g] State Key Laboratory of Brain and Cognitive Science, Beijing MRI Center for Brain Research, Institute of Biophysics, Chinese Academy of Sciences, Beijing, 100101, China
[h] University of Chinese Academic of Sciences, Beijing, 100049, China
[i] Beijing Institute for Brain Disorders, Beijing, 100053, China

ARTICLE INFO

Article history:
Received 20 August 2020
Received in revised form
7 January 2021
Accepted 26 February 2021
Available online 9 March 2021

Keywords:
MR current Density imaging
MR electrical Impedance tomography
Transcranial electric stimulation
Safety

ABSTRACT

Background: Transcranial electric stimulation during MR imaging can introduce safety issues due to coupling of the RF field with the stimulation electrodes and leads.
Objective: To optimize the stimulation setup for MR current density imaging (MRCDI) and increase maximum stimulation current, a new low-conductivity ($\sigma = 29.4$ S/m) lead wire is designed and tested.
Method: The antenna effect was simulated to investigate the effect of lead conductivity. Subsequently, specific absorption rate (SAR) simulations for realistic lead configurations with low-conductivity leads and two electrode types were performed at 128 MHz and 298 MHz being the Larmor frequencies of protons at 3T and 7T. Temperature measurements were performed during MRI using high power deposition sequences to ensure that the electrodes comply with MRI temperature regulations.
Results: The antenna effect was found for copper leads at ¼ RF wavelength and could be reliably eliminated using low-conductivity leads. Realistic lead configurations increased the head SAR and the local head SAR at the electrodes only minimally. The highest temperatures were measured on the rings of center-surround electrodes, while circular electrodes showed little heating. No temperature increase above the safety limit of 39 °C was observed.
Conclusion: Coupling to the RF field can be reliably prevented by low-conductivity leads, enabling cable paths optimal for MRCDI. Compared to commercial copper leads with safety resistors, the low-conductivity leads had lower total impedance, enabling the application of higher currents without changing stimulator design. Attention must be paid to electrode pads.

Introduction

Roughly two decades ago, Nitsche and Paulus showed that human motor cortex excitability could be non-invasively modulated by weak electric currents applied through the intact skull by surface electrodes [1]. Since then, the use of transcranial electric stimulation (TES) techniques in neuroscience applications has grown tremendously. There is also increasing interest to apply TES inside magnetic resonance imaging (MRI) scanners. This is

* Corresponding author. Danish Research Centre for Magnetic Resonance, Centre for Functional and Diagnostic Imaging and Research, Copenhagen University Hospital Hvidovre, Section 714, Kettegaard Allé 30, 2650, Hvidovre, Denmark.
E-mail address: larsh@drcmr.dk (L.G. Hanson).
[1] These authors contributed equally to this work.

https://doi.org/10.1016/j.brs.2021.02.019

motivated by the wish to use functional MRI (fMRI) for characterizing the physiological stimulation effects. More recently, MRI is also applied to shed light on the physical current flow inside the brain. Simulation of the current flow using forward models of the head anatomy [2,3] is feasible, but the accuracies and reliabilities of the results are challenged by a number of factors. For example, the ohmic conductivities of the head tissues at low frequencies are quite uncertain, highlighting the need to validate the simulated fields [4].

MR current density imaging (MRCDI) [5] and MR electrical impedance tomography (MREIT) [6] are two emerging modalities that can indirectly measure the current flow in the brain and the conductivity of the tissue, respectively. These techniques have the potential to improve the accuracy of electric field simulations for TES, as well as for source localization in electro- and magnetoencephalography (EEG and MEG) [7], and can aid in the characterization of pathological tissue [8]. Similar to TES, MRCDI and MREIT use weak currents applied via surface electrodes. The current-induced changes of the static magnetic field are measured and used to determine the current flow or tissue conductivities at low frequency.

The current flow inside the brain changes the magnetic field only slightly, resulting in a low signal-to-noise ratio (SNR) of the measurements and making them prone to artifacts. The effect of the stray fields from the cable currents has previously been studied [9]. Unless the leads are aligned fully parallel to the main magnetic field, the induced stray fields will strongly influence the current-induced magnetic field changes measured in the brain, and therefore the current density and conductivity reconstruction. This can be corrected for by tracking the cables in MR images and using the Biot-Savart law to subtract induced stray fields [10]. Although the correction method significantly improves the current density reconstruction results, it would be preferable to orient the leads parallel to the main magnetic field to reduce residual errors and increase the robustness of the measurement approach.

For TES, MRCDI and MREIT, the currents are applied through lead wires connected to the subject's scalp via surface electrodes. Extra safety measures have to be taken when conductive materials are used in an MR scanner, especially when in contact with tissue. Many incidences of patient burns caused by coupling between the RF field and lead wires have been reported [11]. However, no burn incidents have been reported for TES-MRI. Heating of leads can be caused by direct electromagnetic induction in wire loops [12] and highly conductive loops must be avoided during MRI. Another important origin of heating is the antenna effect that occurs when wires or other conductors of appropriate length act as "receive antennas" for the RF field. For increasing field strengths, the antenna effect becomes an increasing problem due to the shorter wavelength of the RF field. Half a wavelength is typically found to be the critical length for heating [13,14], but it has been shown experimentally that the length of the lead required to observe the effect also depends on the boundary conditions on each end of the lead [15]. For high impedance at one end (open or connected to a safety resistor or high impedance amplifier) and relatively low impedance at the other end (connected to tissue) ¼ RF wavelength can be critical as well. Therefore, the design of lead wires that reliably prevent the occurrence of electromagnetic induction and antenna effects despite varying boundary conditions is important, but challenging.

Conventional TES devices use highly conductive leads (usually copper) between the stimulator and surface electrodes. For the TES device that is most commonly used in combination with MRI (DC-STIMULATOR MR, neuroCare Group GmbH, München, Germany), most of the cable is realized as twisted pair cable and 5 kΩ safety resistors are added to each of the two leads to limit the length of highly conductive material near the scanned subject (Fig. 1a). This design improves safety but prevents an optimal cable orientation for MRCDI and MREIT experiments. Because the device supplies a maximal output voltage of 30 V, the safety resistors also limit the maximum possible stimulation current to around 2 mA. Most TES studies so far have used currents up to 2 mA, but there is recent interest to explore higher current strength of up to 4 mA to increase efficacy [16–20]. The safety resistors limit the use of TES-fMRI studies to characterize the physiological effect of higher TES currents.

The aim of this work is to redesign the leads for combined MR and current injection experiments to remove the above restrictions. Specifically, the goal was to develop leads that would allow long straight wire paths parallel to the static magnetic fields and support stimulation currents up to 4 mA with the existing stimulator while not compromising safety. Instead of using highly conductive materials and local safety resistors, we propose to use a distributed resistance by having leads with much lower conductivity, while also having an overall lower total impedance. Carbon fiber leads are routinely used for EEG-MRI and are reported to decrease specific absorption rate (SAR) compared to copper leads [21]. Here, we extend this approach to TES and further minimize the risk for the occurrence of antenna effects by using an even less conductive silicone rubber material ($\sigma = 29.4$ S/m) for the lead wires. Numerical methods have previously been used to estimate SAR for combined EEG-MRI studies [21–23], as well as for TES-MRI experiments [24,25].

In this study, we use both numerical simulations to estimate SAR as well as experimental temperature measurement. We first simulate a worst-case antenna effect at 298 MHz to investigate the relationship between the antenna effect and conductivity. Secondly, we simulate two electrode types with various lead configurations to ensure safety at both 128 MHz and 298 MHz, corresponding to the proton Larmor frequencies at 3T and 7T magnetic field strength. Lastly, temperature measurements are performed on the electrodes and leads made in-house during in vivo MRI at both field strengths.

Methods

Electrode and lead design

We constructed two commonly used TES electrode types in-house: 1) The circular electrode commonly used for non-focal stimulation in TES or for MRCDI and MREIT (Fig. 1b) and 2) the center-surround electrode used for focal stimulation in TES experiments [26] (Fig. 1c). Both types are 3 mm thick. The circular electrodes are 5 cm in diameter. The center-surround electrodes have an outer ring with an inner and outer diameter of 10 cm and 8 cm, respectively. The diameter of the center electrode is 3 cm. For all electrodes, a 90 cm silicone rubber strip with a cross-sectional area of 10 mm^2 was cut out and used as the lead wire. Both electrodes and leads are made from silicone rubber (ELASTOSIL® R 570/60 RUSS, Wacker, Munich, Germany). The resistance of each of the lead wires is 2 kΩ ± 200 Ω. To ensure proper electrical connection and mechanical strength, the rubber leads are sewed on to the electrodes. The other ends of the leads are connected to copper leads with cable crimps. Medical grade touch-proof safety connectors are connected to the copper leads (MS1525-B, Stäubli, Pfäffikon, Switzerland). A glass-fiber braided sleeving (GSS6, HellermannTyton, Crawley, Germany) is used for thermal and electrical insulation. The glass-fiber sleeving is also sewed on to the electrode and connected to the copper wire to relieve the silicone rubber lead of any strain. Ten20 conductive EEG paste (D.O. Weaver and Co.,

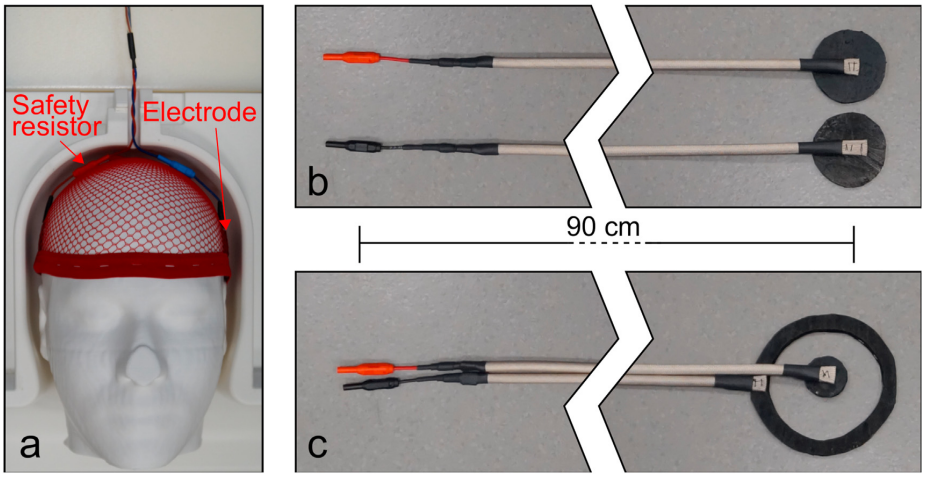

Fig. 1. a) Commercially available TES-MRI setup (DC-STIMULATOR MR, neuroCare Group GmbH, München, Germany) with copper lead wires and 5 kΩ safety resistors. Leading the wires in the superior direction through the opening in the coil and using twisted pair cables restricts the lead configuration and causes stray fields compromising MRCDI experiments. b) and c) show the proposed circular and center-surround electrode and the lead design, respectively. Low-conductivity silicone rubber ($\sigma = 29.4$ S/m) is used for electrodes and leads (black) thermally and electrically shielded with a glass fiber sleeving (gray). Medical grade touch-proof MC connectors are used to connect the electrodes to copper lead wires 90 cm away from the subject's head.

Aurora, CO, USA) is used between the electrodes and abraded skin to ensure proper connection.

Simulations

Finite-difference time-domain (FDTD) simulations were performed in Sim4Life (ZMT, Zurich, Switzerland) to obtain specific absorption rate (SAR) results. Simulations were performed with 128 MHz and 298 MHz harmonic excitations. All simulations ran until convergence at −30 dB, tested for steady-state on the lumped elements and sources on the RF coils.

Phantom

The heterogeneous male body model Duke from the IT'IS foundation was used in the simulations [27]. The head was positioned at the centers of the birdcage coils in all simulations. 2 mm isotropic resolution was used for Duke's head and shoulders and 4 mm for the torso. The rest of the body was segmented according to the automatic gridding produced by Sim4Life. This was done to reduce simulation time while still allowing sufficient current flow to obtain accurate simulation results [28].

RF coils

For 128 MHz simulations, a generic body coil was used (Fig. 3). Although the proton Larmor frequency of the scanner used in the experiments is 123 MHz the small difference in frequency will have minimal influence on the results. The 298 MHz coil (Fig. 2a) is a model of a transmit head coil [29] (7T volume T/R, Nova Medical, Wilmington, MA). Both coils are 16 rung high-pass birdcage coils. The dimensions are given in Table 1. The coils have two input ports on the superior end-ring 90° apart shifted 45° relative to the body model. The coils were iteratively tuned to the respective frequencies loaded with Duke with the head placed in the centers of the coils. The coils were driven in quadrature mode with equal input power on both ports. For coil model validation, see S2 in supplementary materials.

SAR evaluation

SAR is a measure of the RF power absorbed by the tissue and is given by

$$SAR = \frac{\sigma}{2\rho}\left|\vec{E}\right|^2, \tag{1}$$

where σ is the tissue conductivity, ρ is the density of tissue end $\left|\vec{E}\right|$ is the peak electric field inside the tissue.

According to international guidelines IEC 60601-2-33 [30], SAR is limited during MRI to avoid excessive heating of a subject due to absorbed RF power. The two relevant limitations for head MRI are head SAR (SAR averaged over the mass of the head) and local head SAR given as the peak spatial average SAR over 1 g or 10 g of tissue. To evaluate the influence that the electrodes and leads have on SAR, we compare head SAR and 1 g local head SAR for a reference simulation to simulations that include electrodes. The head SAR and 1 g local head SAR ratios are expressed as

$$R_m = \frac{HeadSAR}{HeadSAR_{ref}},\ R_{1g} = \frac{SAR_{1g}}{SAR_{1g_{ref}}}. \tag{2}$$

SAR is compared for 1 W radiated power as well as for a calibrated B_1 field. The input power P for each simulation is scaled such that the average amplitude of B_1 in the center slice of the coil is the same for all simulations. This is done the following way:

$$P = P_{ref}\left(\frac{B_{1,ref}}{B_1}\right)^2. \tag{3}$$

P_{ref} is the input power for the reference simulation, set to 1 W, $B_{1,ref}$ is the average B_1 amplitude for the center slice of the reference simulations, and B_1 is the average B_1 amplitude for the corresponding simulation before normalization.

The electrodes, leads, and gel are excluded when R_m and R_{1g} are calculated to include only tissue SAR when averaging is performed. By excluding the electrodes from R_m and R_{1g} calculations, these

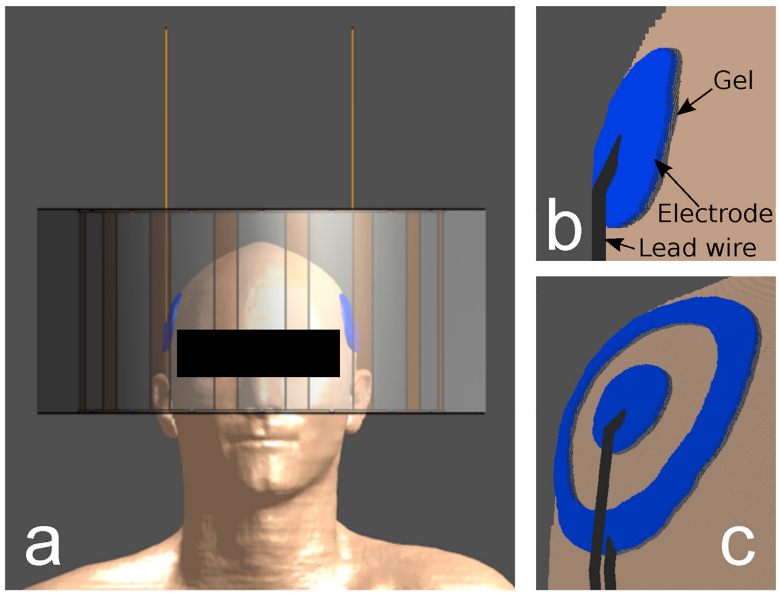

Fig. 2. a) Coil model for 298 MHz simulations with electrodes and straight leads to investigate the relationship between the antenna effect and conductivity. Circular (b) and center-surround electrode (c) montages including leads, electrodes and gel connected to the scalp, modeled with an isotropic grid with 0.5 mm resolution.

values only express the changes in SAR on the tissue caused by adding electrodes and not the power loss in the electrodes and the gel. Temperature measurements are used to ensure that the heating caused by the power loss in the electrodes and gel is within regulation limits [30].

Antenna effect simulations

To examine the relationship between the antenna effect and the conductivity of the lead wires, a worst-case simulation was performed with the lead wires parallel to the z-direction with one end connected to the circular electrodes and one end in free space as seen in Fig. 2a. This simulation was only performed at 298 MHz as the antenna effect becomes an increasing problem for higher frequencies. The simulations were performed with varying lead lengths from 0 to 100 cm with 10 cm increments including 25 cm and 75 cm as they are approximately ¼ and ¾ wavelength in air at the proton Larmor frequency 298 MHz. Two conductivities were used for all the incremental lengths of the lead wires, namely $5.8 \cdot 10^7$ S/m for copper and 29.4 S/m for silicone rubber with constant cross-sectional area. For 25 cm (the worst-case length), multiple conductivities were simulated with logarithmic increments from 10^2 S/m to 10^7 S/m. The average power dissipation on the electrodes is used as a measure of the severity of the antenna effect.

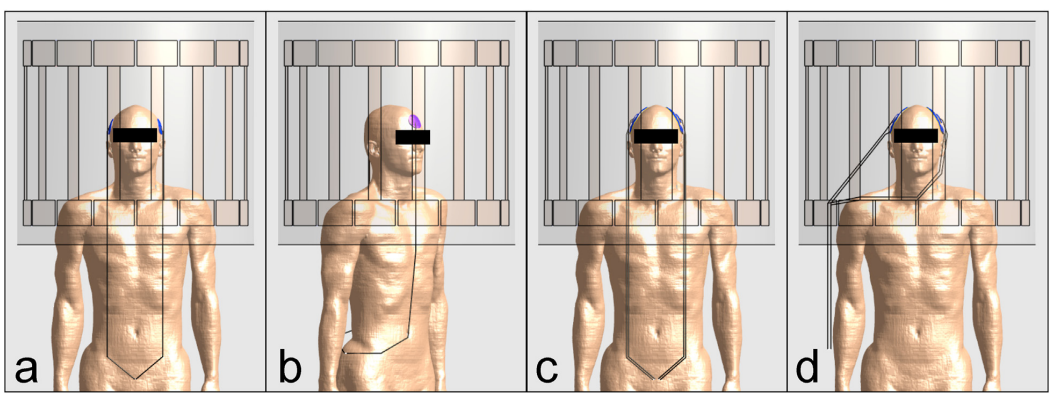

Fig. 3. Four lead configurations were simulated for both field strengths. Although only shown for the 128 MHz body coil here, the simulations were also performed for the 298 MHz head coil seen in Fig. 2a. Right-left (a) and anterior-posterior (b) montages for the circular electrodes were simulated with intended lead configurations as central as possible in the coil and with straight leads to reduce stray fields for MRCDI. For the center-surround electrodes, right-left montage with the intended lead configuration (c) was simulated as well as a worst case with leads closer to the coil (d), where the E-field is higher.

Table 1
Dimensions for the coil models used in the simulations.

	128 MHz (3T)	298 MHz (7T)
No. of Legs	16	16
Coil Radius	352 mm	155 mm
Leg Length	420 mm	168 mm
Leg Width	40 mm	20 mm
Endring Width	80 mm	2.5 mm
Shield Radius	371.5 mm	190 mm
Shield Length	700 mm	173 mm

Realistic lead configuration simulations

For the realistic lead configurations, simulations were performed for the center-surround and circular electrodes at 128 MHz and 298 MHz, respectively. Four lead configurations were simulated as seen in Fig. 3. A right-left and an anterior-posterior montage were simulated for the circular electrodes (Fig. 3a and b). The center-surround electrodes were only simulated for a right-left montage (Fig. 3c). The lead configurations in Fig. 3a–c show the intended use cases. In addition, the lead configuration in Fig. 3d was also simulated to ensure that misplacing the leads will not have critical consequences due to higher E-field close to the RF coil. All three electrode montages were also simulated without leads for both magnetic field strengths. The electrodes and gel are shown in Fig. 2b and c. The add-on subgrid feature using the Acceleware GPU solver (Acceleware, Calgary, Canada) in Sim4Life was used to obtain a fine resolution for electrode, gel and leads while keeping the same grid size in the rest of the simulation space. An isotropic grid size of 0.5 mm was used for electrodes, gel and leads. With this resolution, the smallest structure in any direction is minimum 4 times the grid size.

The conductivity σ and the relative permittivity ε_r for both the silicone rubber and the conductive gel, used between the electrodes and the skin, were measured with an ENA Series Network Analyzer E5071C and an open-ended probe 85070A (Agilent Technologies, Santa Clara, CA) at relevant frequencies to ensure more accurate simulations. For silicone rubber $\sigma = 29.4$ S/m and $\varepsilon_r = 6$ were used for both frequencies. For the Ten20 gel $\sigma = 0.86$ S/m and $\varepsilon_r = 36.61$ were used at 128 MHz and $\sigma = 0.95$ S/m and $\varepsilon_r = 32.55$ at 298 MHz.

The leads were terminated with an equivalent resistor representing the output impedance of the combined copper cable, filter, and stimulator (DC-STIMULATOR MR, neuroCare Group GmbH, München, Germany). The output impedances at the relevant simulation frequencies were found with a vector network analyzer (VNA). Since the leads are 90 cm long, the equivalent resistors are far outside the effective exposure volume of the coils as seen in Fig. 3.

Experimental setup

Experiments were performed on 3T (MAGNETOM Prisma; Siemens Healthcare, Erlangen, Germany) and 7T (Achieva; Philips Healthcare, Best, The Netherlands) whole-body MRI scanners. Two senior researchers involved in the project were scanned in the experiments. Informed consent was obtained from the participants prior to the MR scans. The touch-proof safety connectors on the electrode leads were connected via a Biopac MECMRI-1 cable to the Biopac MRIRFIF pi filter (BIOPAC Systems, Goleta, USA). The filter reduces noise from the outside and is located in a panel between the scanner room and the control room. For stimulation, a neurostimulator will be connected to the filter on the control room side. The neurostimulator was not used in the experiments as the output impedance of the copper cable and filter remained the same independent of the stimulator. For safety assessment of electrodes and leads, temperature measurements were performed in the 3T and 7T scanners. Image quality assessment and imaging of the leads for stray field correction in MRCDI was performed at 3T. See S1 in the supplementary material for further details and results.

Temperature measurements

For temperature measurements at 3T, the built-in birdcage body coil was used as the transmit coil while at 7T, a birdcage head coil was used for excitation (7T volume T/R, Nova Medical, Wilmington, MA). Fiber-optic probes (Opsens Solutions, Quebec City, Canada) were used to measure the temperature. Four probes were available. The probes were placed in the gel between the electrode and the scalp at various locations indicated in Table 3 and Fig. 6a and b. When a reference probe was used, it was taped to the top of the head of the subject and insulated with a pad to better imitate the scenario of the other probes.

A Rapid Acquisition with Relaxation Enhancement (RARE) sequence was used for both field strengths to obtain a high SAR for the temperature measurements. The sequence parameters were adjusted to obtain approximately 100% reported SAR by the scanner relative to the SAR limit. At 3T, the RARE sequence parameters were repetition time $T_R = 175$ ms, echo time $T_E = 100$ ms, refocusing tip angle $= 180°$, echo train length $= 15$, image matrix $512 \times 512 \times 27$ and resolution $0.43 \times 0.43 \times 5.2$ mm^3. And at 7T, $T_R = 3584$ ms, $T_E = 47.54$ ms, echo train length $= 9$, image matrix $768 \times 768 \times 33$, resolution $0.28 \times 0.28 \times 3$ mm^3 and a varying refocusing tip angle. A Pseudo Continuous Arterial Spin Labeling (pCASL) sequence ($T_R = 4100$ ms, $T_E = 18$ ms, excitation tip angle $= 90°$, image matrix $73 \times 73 \times 60$, resolution $3 \times 3 \times 4$ mm^3, tag duration/tag delay $= 1500/1800$ ms, tag pulse angle $= 24°$ and tag gradient strength $= 7$ mT/m) was also used at 3T, as it is a relatively high SAR sequence that will potentially be used for TES-MRI studies. About 50% SAR was reported for the pCASL sequence. The sequences ran for 20 min to achieve sufficient data to accurately model the temperature increase and find the steady-state temperature. The model used is

$$T(t) = T_{ss} - \Delta T \cdot e^{-\frac{t}{t_c}}, \quad (4)$$

where $T(t)$ is the temperature at time t, T_{ss} is the steady-state temperature, ΔT is the difference between the start and steady-state temperature, and t_C is the time constant of the exponential term.

Stray field comparison

An MRCDI experiment with 1 mA current injection was performed to illustrate the change of stray fields from the leads when the improved lead configuration is used. Lead configurations seen in Fig. 1a and our proposed use as seen in Fig. 3a were compared. See Göksu et al. [10] for further details on the used MRCDI method. The imaging of silicone rubber used for cable tracking is presented in supplementary material S1.

Results

Antenna effect

Simulations with varying copper lead lengths showed that the antenna effect occurs at odd multiples of ¼ RF wavelength with ¼ being worse than ¾ (Fig. 4a). The same simulations but with low-conductivity silicone rubber showed that the antenna effect is eliminated with this material (Fig. 4a). Further investigation of the relationship between the antenna effect and conductivity at the worst-case length (25 cm) is shown in Fig. 4b. Carbon fiber leads

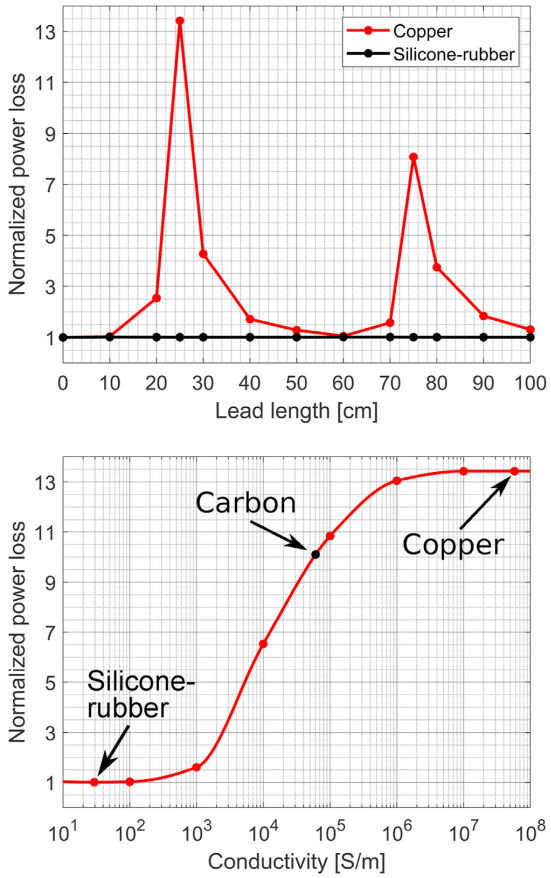

Fig. 4. a) Power loss on electrodes vs lead length for antenna effect simulations seen in Fig. 2a for copper and silicone rubber, respectively. b) Power loss on electrodes vs conductivity of 25 cm long leads shown to be the worst case. Power loss is normalized to average power loss on both electrodes without attached leads.

with a conductivity of $6.1 \cdot 10^4$ S/m [31] only reduces the severity of the antenna effect by about 25%, while low-conductivity silicone rubber robustly prevents the occurrence of an antenna effect.

SAR for realistic lead configurations

SAR simulation results for realistic lead configurations are presented in Fig. 5 and Table 2. In Fig. 5, 1 g local head SAR for all three electrode montages with center leads (see Fig. 3a–c) are shown. Adding electrodes, gel, and leads to Duke, changes the spatial variation of SAR, especially around the electrodes, but 1 g local head SAR is for all simulations in the same location as for the reference simulation. For 128 MHz simulations, 1 g local head SAR occurs on the skin on the left side of the neck while for 298 MHz it is in the cerebrospinal fluid. As seen in Table 2, only minimal changes to the B_1 field and SAR occur for 128 MHz and 298 MHz with circular electrodes, while the center-surround electrodes have more influence on the B_1 field, and therefore higher SAR after normalization.

Temperature measurements

One of the temperature measurements (indicated in Table 3) including the fitted model is shown in Fig. 6c. The modeled steady-state temperatures for all the measurements are listed in Table 3. Probe positions indicated in Table 3 are presented in Fig. 6a and b for the center-surround and circular electrodes, respectively.

For the circular electrodes at 3T, the highest temperature was observed on the posterior electrode for the anterior-posterior montage, with a temperature of 37.6 °C compared to 35 °C for the reference probe. For the right-left montage, the maximum temperature on the electrodes was only 1 °C higher than for the reference probe.

The center-surround electrodes at 3T showed the highest temperature increase (max 38.5 °C), with no observable difference between electrode pads with and without leads. Off-center leads also did not give rise to higher temperatures. For the pCASL sequence, the steady-state temperature was about 1 °C lower than for the RARE sequence in the same session, marked with an asterisk in Table 3.

Very limited increase was found for all measurements at 7T. The highest measured difference between the reference probe and a probe on the electrodes was 0.6 °C.

Stray field comparison

Fig. 7b and e show the fields from the leads calculated with Biot-Savart law using the tracked lead location seen in Fig. 7a and d. Fig. 7c and f are the measured current-induced fields in the MR scanner. The measured fields are both from currents flowing in the leads and in the subject's tissue. It is clear from comparing Fig. 7b and c that ΔB_{zc} is dominated by stray fields from the leads. With our optimized lead configuration with the silicone rubber leads as seen in Figs. 3a and 7d, where the leads are aligned in the z-direction, the stray field from the leads are greatly reduced (Fig. 7e) and therefore there is no relationship between lead stray field and ΔB_{zc} that is dominated by tissue currents.

Discussion

TES electrodes with copper leads pose a potential danger to the subject when used during an MRI session. Due to the coupling between the RF field of the scanner and the highly conductive leads, burns of the subject's scalp can occur unless appropriate measures are taken, such as adding safety resistors in a well-considered way. To minimize coupling between the RF field and the leads in general, we propose to use leads made with a low-conductivity material. By that, we gain flexibility to optimize the leads for the intended applications while ensuring safety. Additionally, this makes it easier to safely design more complex electrode configurations with multiple leads, such as the 4x1 montage [2] used for focal stimulation in TES-fMRI experiments. These electrodes and leads can relatively easily be constructed in-house from sheets of conductive silicone rubber.

In simulations, the antenna effect was found for odd multiples of ¼ RF wavelength (Fig. 4a), which is in agreement with previously reported experimental results [15] with the same boundary conditions. The antenna effect is often believed to occur at ½ RF wavelength only, but as pointed out by Balasubramanian et al. [15], this depends on the boundary condition of the leads. With low impedance at one end and high at the other, it occurs at ¼ RF wavelength, whereas with the same boundary condition at each end, e.g. immersed in tissue, antenna effect occurs at ½ RF wavelength.

Simulation results with varying lead conductivity at worst-case length (Fig. 4b) prove that the antenna effect will not occur for

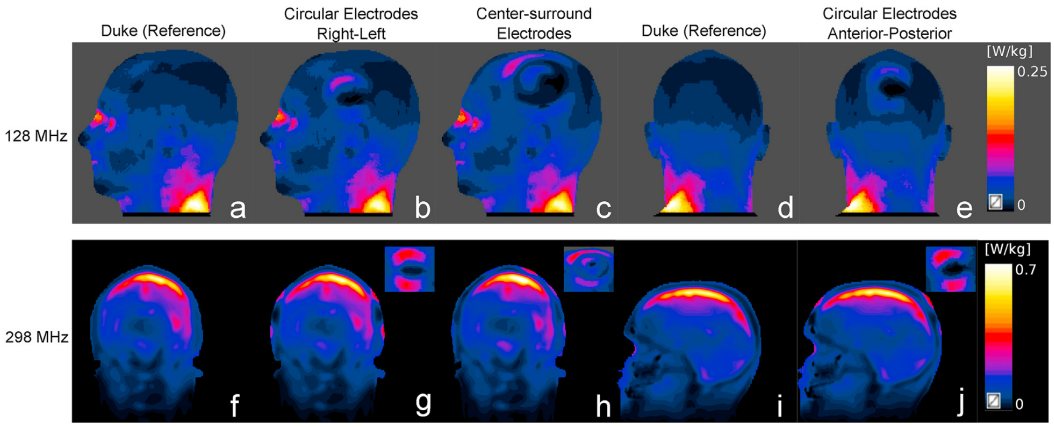

Fig. 5. 1 g average SAR for normalized B_1 for simulations at 128 MHz (top) and 298 MHz (bottom). Peak SAR for 128 MHz occurs on the skin of the left side of the neck, while it is in CSF for the 298 MHz simulations. A reference simulation of Duke without electrodes is shown in a), d), f), and i). The rest of the results are from simulations with electrodes and intended lead configurations (see Fig. 3a–c). Insets in the corner for g), h) and j) show the surface SAR around the electrodes.

silicone rubber with lead conductivity at 29.4 S/m. This increases the flexibility of the lead configuration and improves the experimental setup for MRCDI experiments. Additionally, no safety resistors are needed, which decreases the overall resistance of the leads compared to the conventional setup and allows for higher stimulation currents. This enables the use of increased stimulation current to study immediate and after-effects on BOLD activity using a standard stimulator. Also, safety resistors enforce nodes in electromagnetic waves, which may cause high local fields causing heating in nearby material and even resistor damage [24]. Careful design is needed to limit these effects and ensure appropriate distance from tissue. The simulations also show that carbon leads, which are often used as a safer alternative to copper leads, only reduce the severity of the antenna effect in our simulations by about 25%. Therefore, using carbon leads can provide a false sense of safety and has to be considered carefully for each specific case. Previous simulation work on a 256-electrode EEG cap has shown consistent results by comparing peak local SAR for varying lead conductivities [22]. The authors reported a 6-fold increase in peak 1 g local head SAR for high conductivities (including carbon) and no increase for conductivities below 100 S/m. The study was not for a specific resonance condition as in our case. Our results may therefore also be relevant for the EEG-MRI community.

Only very limited changes were observed for R_m and R_{1g} for all simulations with realistic lead configurations as seen in Table 2. In most cases the B_1 was slightly lower than $B_{1,ref}$ due to the additional load on the coil when electrodes and leads were included. For 1 W input power, this is also reflected in the slightly lower SAR for some simulations, especially with leads. For the same reason, all simulations with leads have lower SAR and more influence on B_1 than simulation without leads for 1 W input power. Slight changes to the spatial distribution of the RF field caused by electrodes and leads can also influence R_m and especially R_{1g}.

Overall, a very small change and mostly reduction in SAR is seen before B_1 normalization, while some increase in SAR is reported after normalizing. This is not seen as a problem since, if the scanner increases the input power, then the calculated SAR will be adjusted accordingly and the SAR safety limits will be reached earlier. In worst case, this will have an influence on the available ranges of sequence parameters, but not on safety.

Although the electrodes have an influence on local SAR values in the proximity to the electrodes as seen in Fig. 5, the 1 g local head SAR close to the electrodes does not exceed peak 1 g local head SAR already present in the reference simulation. The peak 1 g local head SAR was also in all simulations at the same location as for the reference simulations. Therefore, the local head SAR limits imposed by the scanner will still ensure conformance with the safety regulations. Additionally, in the 298 MHz simulations, the center-surround electrodes are located close to the locations of peak local head SAR without negative effect.

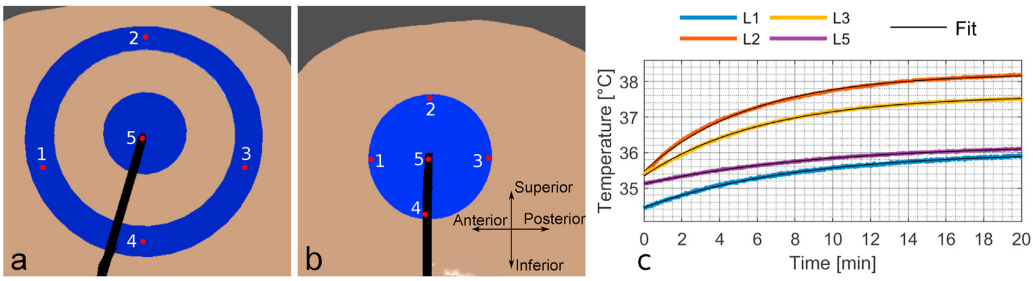

Fig. 6. In a) and b) the numbers on the electrodes indicate the probe position referred to in Fig. 6c and Table 3 c) Temperature measurement for center-surround electrodes with center leads (Fig. 3c). L in the legend indicates that it is a measurement on the left electrode. The black curves are the fitted models (Eqn (4)).

Table 2
Head SAR and local head SAR (1 g average) ratios (R_m and R_{1g}) for both field strengths and all simulated electrode montages compared to reference simulations. SAR is given for 1 W input power as well as normalized for the B_1 field in the center slice of the coil. The ratio between $B_{1,ref}$ and B_1 for the corresponding simulation is used for normalization. All local head SAR maxima were at the same location as for the reference simulation.

Frequency	Electrodes	Setup	Normalized to 1 W input			Normalized to B_1	
			R_m	R_{1g}	B_1^{ref}/B_1	R_m	R_{1g}
128 MHz	Circular	Without leads	1.02	0.96	0.99	0.99	0.94
	Right-left	With leads	0.99	0.94	0.99	0.97	0.93
	Circular	Without leads	1.02	1.00	0.99	1.00	0.98
	Anterior-posterior	With leads	0.96	0.93	1.02	1.01	0.98
	Center-surround	Without leads	1.01	0.94	1.01	1.02	0.95
		Center leads	0.97	0.86	1.02	1.01	0.90
		Off-center leads	0.94	0.91	1.06	1.04	1.01
298 MHz	Circular	Without leads	1.00	1.00	1.01	1.03	1.02
	Right-left	With leads	0.98	1.00	1.02	1.02	1.04
	Circular	Without leads	1.00	0.97	1.00	1.00	0.98
	Anterior-posterior	With leads	0.98	0.98	1.01	1.00	0.99
	Center-surround	Without leads	0.93	0.96	1.09	1.10	1.13
		Center leads	0.90	0.96	1.09	1.07	1.14
		Off-center leads	0.89	0.95	1.10	1.07	1.15

The highest measured temperature for the circular electrodes was on the posterior electrode. This is most likely not due to higher power dissipation on the electrode, but rather better thermal insulation as the head rests on the electrode and cushions.

At 3T, more heating was observed for the center-surround electrodes than the circular electrode. The heating was independent of lead position as well as whether leads were attached or not. In agreement with a previous study by Kozlov et al. [25], this indicates that the shape and size of the electrodes have high influence on heating. Therefore, care must be taken when designing new electrodes for TES-MRI experiments. The impedance around the ring of the center-surround electrode is about 300 Ω. Higher impedance would cause less heating, but it is a tradeoff between heating and homogeneous stimulation currents for focal stimulation. It has to be pointed out that the heating observed is with a high-SAR RARE sequence, which is not a recommended sequence for TES-MRI experiments. Usually, low-SAR echo planar imaging (EPI) or gradient-echo sequences will be used or in worst-case the pCASL sequence also tested in the temperature experiments. The pCASL sequence showed about 1 °C less heating than the RARE sequence. In contrast to our findings at 3T, a previous study reported much less heating on the center-surround electrodes [32]. The unspecified conductivity of the electrode material has high influence on the heating, but more importantly only an EPI sequence was used for the heat test. Since EPI used for fMRI experiments is usually a very low-SAR sequence at 3T, insignificant heating would be expected.

At 7T no considerable heating was observed. This is attributed to the fact that SAR is already higher at 7T for similar sequences, and the input power is therefore more restricted compared to 3T.

Although noticeable heating was measured on the center-surround electrodes at 3T, the temperatures were always lower than limits imposed by the international guidelines IEC 60601-2-33 [30] stating that the maximum tissue temperature has to be limited to 39 °C.

To further ensure safety and reduce the risk of resistor damage, the conventional electrodes and leads used in this work are limited to use with EPI sequences. The manufacturer requires removal of the cables when other sequences are used. Under the conditions evaluated, this is not necessary with low conductivity silicone rubber leads since no safety resistors are used and safety tests have been performed for high SAR sequences.

Table 3
Modeled steady state temperature from all measurements with various setups and probe positions. The numbers for the positions are indicated in Fig. 6a–b and L, R, A and P refer to electrode position (left, right, anterior and posterior). Ref is the reference probe on top of the head away from the electrodes. For the RARE sequence, the SAR was approximately 100% and for ASL, it was approximately 50%, varying slightly with subjects. The asterisks (*) indicate the same scan sessions for a RARE and pCASL sequence with electrodes and temperature probes in the same location. The double asterisks (**) indicate the data shown in Fig. 6c.

B_0	Electrodes	Setup	Sequence	Probe positions	Steady state temperature
3T	Circular	Right-left	RARE	[Ref L1 R3 L5]	[35.2 35.4 35.8 36.2]
		Anterior-posterior	RARE	[Ref A4 P2 P4]	[35.0 36.3 37.2 37.6]
	Center-surround	Without leads	RARE	[Ref L4 R2 L2]	[35.6 35.7 36.3 36.6]
				[L1 L5 L3 L2]	[35.9 36.4 37.2 38.4]
				[L1 L5 L3 L2]	[35.5 35.8 37.7 38.5]
		On-center leads	RARE	[Ref L4 L2 R2]	[35.6 36.2 37.2 37.2]
				[Ref L2 R2 L4]	[34.8 36.4 37.0 37.9]*
				[L1 L5 L3 L2]	[36.4 36.7 37.5 37.6]
				[L1 L5 L3 L2]	[36.0 36.2 37.6 38.2]**
		On-center leads	pCASL	[Ref L2 R2 L4]	[34.6 35.8 36.2 36.8]*
		Off-center leads	RARE	[Ref L4 L2 R2]	[35.4 36.2 37.0 37.3]
7T	Circular	Anterior-posterior	RARE	[A4 Ref P4 P2]	[34.9 35.3 35.7 35.9]
	Center-surround	On-center leads	RARE	[R2 L2 Ref L4]	[34.3 35.1 35.4 36.0]

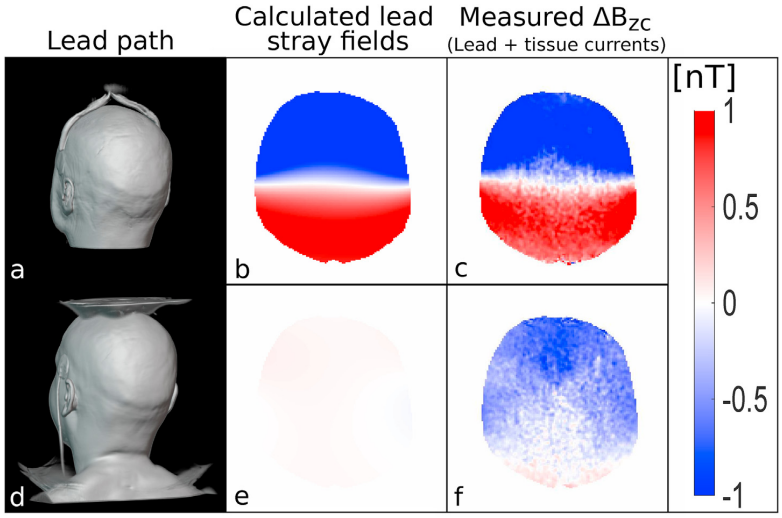

Fig. 7. a) and d) 3D ultra-short T_E images used to track the leads to calculate stray fields (See supplementary material S1). b) and e) are calculated stray fields from the two lead configurations. c) and f) are measured current-induced magnetic field changes. Image c) is clearly dominated by stray fields seen in image b), whereas the stray fields from leads in image e) are greatly reduced, so f) is dominated by tissue currents.

The rubber leads being visible on MR recordings without adding additional material is a practical benefit when doing stray field correction in MRCDI [9] (see supplementary material S1). Conventional copper leads and insulation are not visible on MRI, and therefore additional material needs to be attached around the leads before use. Attention must be paid to image distortions caused by chemical shift, gradient non-linearity, and concomitant fields, however.

The effect of the stray field on the measured ΔB_{zc} demonstrated in our MRCDI experiment necessitates correction by applying the Biot-Savart-Law [9,10]. However, any errors and inaccuracies of lead position estimation will have far less influence for the optimized cable configuration made possible by using silicone rubber leads. Additionally, the lead location cannot be tracked during ΔB_{zc} measurements. Therefore, any movements during the experiment will have detrimental effect on the stray field correction for the non-optimized setup.

The electrodes and leads have very limited and only superficial influence on B_1 and B_0 maps. However, when calculating the signal-to-fluctuation-noise ratio for an EPI time series, image artifacts having long ranging effects (centimeters) were found when copper leads and safety resistors were used. These artifacts were not found with silicone rubber leads. (see supplementary material S1).

Conclusion

We have proposed to use low-conductivity silicone rubber as leads for current injection electrodes in the MR scanner. This eliminates the potential safety hazard that comes with the coupling between high-conductivity materials and the RF field, such as the antenna effect that is not necessarily eliminated with carbon cables or safety resistors. For our setup, the simulations showed no increase in head SAR and head local SAR for both field strengths. Additionally, no temperature above the safety limits was recorded. Due to the increased flexibility of lead configurations, these electrodes offer an advantage for MRCDI experiments due to the reduction of compromising stray fields. For TES-MRI experiments, the maximum stimulation currents can be increased for voltage-limited stimulation devices due to lower overall resistance.

CRediT authorship contribution statement

Fróði Gregersen: Conceptualization, Methodology, Software, Validation, Formal analysis, Investigation, Writing – original draft, Visualization, Funding acquisition. **Cihan Göksu:** Software, Investigation, Writing – review & editing. **Gregor Schaefers:** Validation, Writing – review & editing, Supervision. **Rong Xue:** Resources, Writing – review & editing, Supervision, Funding acquisition. **Axel Thielscher:** Conceptualization, Methodology, Investigation, Writing – review & editing, Supervision, Funding acquisition. **Lars G. Hanson:** Conceptualization, Methodology, Investigation, Writing – review & editing, Supervision, Funding acquisition.

Declaration of competing interest

There are no known conflicts of interest associated with this publication and there has been no significant financial support for this work that could have influenced its outcome.

Acknowledgment

This study was supported by the Lundbeck Foundation (grants R313-2019-622 and R244-2017-196 to AT and R288-2018-236 to CG), the Chinese National Major Scientific Equipment R&D Project (grant ZDYZ2010-2) and a PhD stipend of the Sino-Danish Center for Education and Research to FG. The authors thank Zuo Zhentao, Hasan Hüseyin Eroğlu, Vincent Boer, and Esben Thade Petersen for kind technical help.

Appendix. A Supplementary data

Supplementary data related to this article can be found at https://doi.org/10.1016/j.brs.2021.02.019.

References

[1] Nitsche MA, Paulus W. Excitability changes induced in the human motor cortex by weak transcranial direct current stimulation. J Physiol 2000;527:633–9. https://doi.org/10.1111/j.1469-7793.2000.t01-1-00633.x.

[2] Datta A, Bansal V, Diaz J, Patel J, Reato D, Bikson M. Gyri-precise head model of transcranial direct current stimulation: improved spatial focality using a ring electrode versus conventional rectangular pad. Brain Stimul. 2009;2. https://doi.org/10.1016/j.brs.2009.03.005. 201–7, 207.e1.

[3] Opitz A, Paulus W, Will S, Antunes A, Thielscher A. Determinants of the electric field during transcranial direct current stimulation. Neuroimage 2015;109:140–50. https://doi.org/10.1016/J.NEUROIMAGE.2015.01.033.

[4] Saturnino GB, Thielscher A, Madsen KH, Knösche TR, Weise K. A principled approach to conductivity uncertainty analysis in electric field calculations. Neuroimage 2019;188:821–34. https://doi.org/10.1016/j.neuroimage.2018.12.053.

[5] Joy M, Scott G, Henkelman M. In vivo detection of applied currents by magnetic resonance imaging, vol. 7; 1989.

[6] Ider YZ, Birgül Ö. Use of the magnetic field generated by the internal distribution of injected currents for electrical impedance tomography (MR-EIT). Turk J Electr Eng Comput Sci 1998;6:215–26.

[7] Mosher JC, Leahy RM, Lewis PS. EEG and MEG : forward Solutions for inverse. Methods 1999;46:245–59.

[8] Fear EC, Hagness SC, Meaney PM, Okoniewski M, Stuchly MA. Enhancing breast tumor detection with near-field imaging. IEEE Microw Mag 2002;3:48–56. https://doi.org/10.1109/6668.990683.

[9] Göksu C, Scheffler K, Siebner HR, Thielscher A, Hanson LG. The stray magnetic fields in magnetic resonance current density imaging (MRCDI). Phys Med 2019;59:142–50. https://doi.org/10.1016/j.ejmp.2019.02.022.

[10] Göksu C, Hanson LG, Siebner HR, Ehses P, Scheffler K, Thielscher A. Human in-vivo brain magnetic resonance current density imaging (MRCDI). Neuroimage 2018;171:26–39. https://doi.org/10.1016/j.neuroimage.2017.12.075.

[11] Dempsey MF, Condon B. Review thermal injuries associated with MRI. Clin Radiol 2001;56:457–65. https://doi.org/10.1053/crad.2000.0688.

[12] Lemieux L. Recording of EEG during fMRI experiments: patient safety. MRM; 1997.

[13] Dempsey MF, Condon B, Hadley DM. Investigation of the factors responsible for burns during MRI. J Magn Reson Imag 2001;13:627–31. https://doi.org/10.1002/jmri.1088.

[14] Panych LP, Madore B. The physics of MRI safety. J Magn Reson Imag 2018;47:28–43. https://doi.org/10.1002/jmri.25761.

[15] Balasubramanian M, Wells WM, Ives JR, Britz P, Mulkern RV, Orbach DB. RF heating of gold cup and conductive plastic electrodes during simultaneous EEG and MRI. Neurodiagn J 2017;57:69–83. https://doi.org/10.1080/21646821.2017.1256722.

[16] Mosayebi Samani M, Agboada D, Jamil A, Kuo MF, Nitsche MA. Titrating the neuroplastic effects of cathodal transcranial direct current stimulation (tDCS) over the primary motor cortex. Cortex 2019;119:350–61. https://doi.org/10.1016/j.cortex.2019.04.016.

[17] Workman CD, Fietsam AC, Rudroff T. Different effects of 2 mA and 4 mA transcranial direct current stimulation on muscle activity and torque in a maximal isokinetic fatigue task. Front Hum Neurosci 2020;14:1–11. https://doi.org/10.3389/fnhum.2020.00240.

[18] Chhatbar PY, Chen R, Deardorff R, Dellenbach B, Kautz SA, George MS, et al. Safety and tolerability of transcranial direct current stimulation to stroke patients – A phase I current escalation study. Brain Stimul. 2017;10:553–9. https://doi.org/10.1016/j.brs.2017.02.007.

[19] Workman CD, Fietsam AC, Uc EY, Rudroff T. Cerebellar transcranial direct current stimulation in people with Parkinson's disease: a pilot study. Brain Sci 2020;10. https://doi.org/10.3390/brainsci10020096.

[20] Nitsche MA, Bikson M. Extending the parameter range for tDCS: safety and tolerability of 4 mA stimulation. Brain Stimul. 2017;10:541–2. https://doi.org/10.1016/j.brs.2017.03.002.

[21] Angelone LM, Vasios CE, Wiggins G, Purdon PL, Bonmassar G. On the effect of resistive EEG electrodes and leads during 7 T MRI: simulation and temperature measurement studies. Magn Reson Imaging 2006;24:801–12. https://doi.org/10.1016/j.mri.2006.01.006.

[22] Atefi SR, Serano P, Poulsen C, Angelone LM, Bonmassar G. Numerical and experimental analysis of radiofrequency-induced heating versus lead conductivity during EEG-MRI at 3 T. IEEE Trans Electromagn C 2019;61:852–9. https://doi.org/10.1109/TEMC.2018.2840050.

[23] Jorge J, Grouiller F, Ipek Ö, Stoermer R, Michel CM, Figueiredo P, et al. Simultaneous EEG-fMRI at ultra-high field: artifact prevention and safety assessment. Neuroimage 2015. https://doi.org/10.1016/j.neuroimage.2014.10.055.

[24] Kozlov M, Müller R, Pampel A, Kalloch B, Weiskopf N, Möller HE. RF safety of transcranial direct current stimulation equipment during MRI. 2018. Poster Present Jt Annu Meet ISMRM-ESMRMB 2018, Paris, Fr.

[25] Kozlov M, Horner M, Kainz W, Weiskopf N, Möller HE. Modeling radio-frequency energy-induced heating due to the presence of transcranial electric stimulation setup at 3T. Magn Reson Mater Phys Biol Med 2020. https://doi.org/10.1007/s10334-020-00853-5.

[26] Datta A, Elwassif M, Battaglia F, Bikson M. Transcranial current stimulation focality using disc and ring electrode configurations: FEM analysis. J Neural Eng 2008;5:163–74. https://doi.org/10.1088/1741-2560/5/2/007.

[27] Gosselin MC, Neufeld E, Moser H, Huber E, Farcito S, Gerber L, et al. Development of a new generation of high-resolution anatomical models for medical device evaluation: the Virtual Population 3.0. Phys Med Biol 2014;59:5287–303. https://doi.org/10.1088/0031-9155/59/18/5287.

[28] Wolf S, Diehl D, Gebhardt M, Mallow J, Speck O. SAR simulations for high-field MRI: how much detail, effort, and accuracy is needed? Magn Reson Med 2013;69:1157–68. https://doi.org/10.1002/mrm.24329.

[29] van Lier ALHMW, Kotte ANTJ, Raaymakers BW, Lagendijk JJW, van den Berg CAT. Radiofrequency heating induced by 7T head MRI: thermal assessment using discrete vasculature or pennes' bioheat equation. J Magn Reson Imag 2012;35:795–803. https://doi.org/10.1002/jmri.22878.

[30] IEC. Particular requirements for the basic safety and essential performance of magnetic resonance equipment for medical diagnosis. 2010. IEC 60601-2-33.

[31] Barbalace K. Periodic table of elements: sorted by electrical conductivity. EnvironmentalChemistry.com; 1995. https://environmentalchemistry.com/yogi/periodic/electrical.html. accessed October 14, 2019.

[32] Gbadeyan O, Steinhauser M, Mcmahon K, Meinzer M. Safety, tolerability, blinding efficacy and behavioural effects of a novel MRI-compatible, high-definition tDCS set-up. Brain Stimul. 2016. https://doi.org/10.1016/j.brs.2016.03.018.

Safety Evaluation of a New Setup for Transcranial Electric Stimulation during Magnetic Resonance Imaging

Fróði Gregersen, Cihan Göksu, Gregor Schaefers, Rong Xue, Axel Thielscher and Lars G. Hanson

Supplementary material

S1. Imaging of leads for field correction and image quality assessment

Imaging of leads

For an MRCDI experiment, it is crucial to track the lead wires to perform stray field correction before reconstructing the current flow from measured current-induced magnetic field changes [1]. We explore the effect of the improved cable configuration made possible by distributing the impedance, which ensures safety under the conditions evaluated. Imaging of the leads was done at 3T. A high-resolution structural Pointwise Encoding Time Reduction with Radial Acquisition (PETRA) sequence [2] with image matrix 320×320×320, isotropic resolution of 0.94×0.94×0.94 mm^3, excitation tip angle = 6°, repetition time T_R = 3.6 ms and echo time T_E = 0.07 ms.

A 3D rendering of the PETRA image using MRIcron [3] is shown in Figure S1.1a. Leads, electrodes and gel are clearly visible in the image.

Effect of electrodes on magnetic fields

The electrode's influence on in-vivo images was evaluated with B_0 and B_1^+ maps at 3T. Electrodes with silicone-rubber leads were used. The B_0 field map was acquired with a dual-echo time sequence with T_R = 592 ms, T_E = [4.92 ms 7.38 ms], excitation tip angle = 60°, image matrix 64×64×54 and isotropic resolution of 3×3×3 mm^3. An ultra-fast spoiled gradient echo sequence with a preconditioning RF pulse [4] was used for B_1^+ mapping with T_R = 5000 ms, T_E = 1.83 ms, excitation tip angle = 8°, image matrix

64×64×18 and resolution of 4×4×8 mm^3. Images with electrodes were qualitatively compared to reference images of the same subject without electrodes.

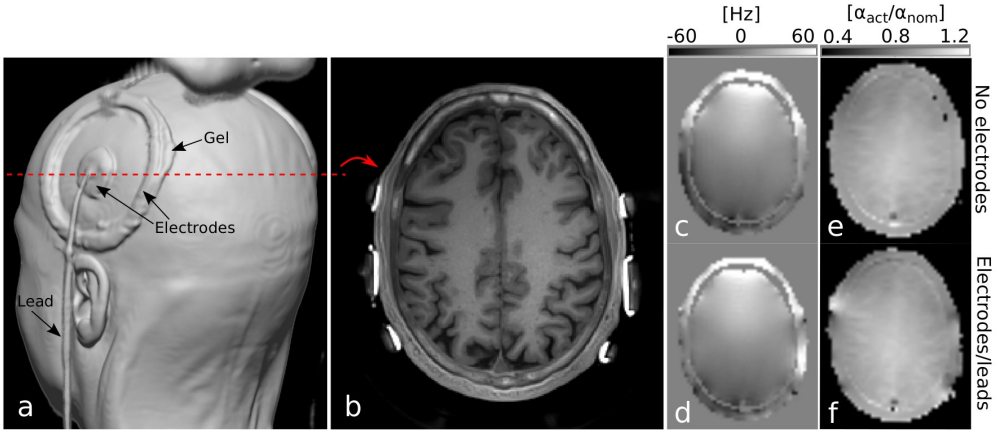

Figure S1.1: a) 3D ultra-short TE recording (PETRA) rendered to image electrodes and leads for stray field correction. Weak tissue aliasing artifacts affect the top. b) Coronal slice of the PETRA image showing the slice position with electrodes used in Figure c-f. B_0 (c and d) and B_1^+ (e and f) field maps without and with electrodes show the influence of the electrodes.

Field map results are presented in Figure S1.1c-S1.1f. Figure S1.1b shows an axial slice through the center of the center-surround electrodes with the PETRA image. Images in Figure S1.1c-S1.1f are at the same location as image Figure S1.1b, which is where the electrodes were found to have most influence. Only center-surround electrodes are shown as they have more influence on the images than circular electrodes. A slight difference can be observed close to the electrodes on the B_0 (Figure S1.1d) and B_1^+ (Figure S1.1f) maps, but it is superficial and does not affect the brain tissue considerably.

B_0 inhomogeneity caused by magnetic susceptibility differences between tissues, gel and electrodes scales linearly with field strength. The influence on B_0 homogeneity at 7T is therefore expected to be slightly worse, but not to a degree where image quality is problematic. The influence of electrodes and gel on the B_1^+ distribution depends on the interaction between the material and the RF field and will vary between specific conditions. From the RF simulations at 298 MHz, it is expected that the electrodes can be used at 7T without any signal loss in brain tissue due to reduced B_1^+ field.

fMRI image quality assessment

To assess the effect of the electrodes and leads on image quality for fMRI studies, where the temporal stability is important, we used two measures; the voxel wise temporal mean signal and signal-to-fluctuation-noise ratio (SFNR). SFNR is the ratio between the temporal mean signal and the temporal standard deviation in each voxel. This was done with a phantom to exclude scan-to-scan variability that can occur for in-vivo scans. The agar gel phantom [5] has relaxation times and conductivity close to human gray matter. This was done at 3T with an echo planar imaging (EPI) sequence with the same parameters as in a proposed fMRI quality assurance protocol [6] (T_R = 2000 ms, T_E = 30 ms, FA = 77°, resolution = 3.44×3.44×4 mm^3 and time points = 100). We did measurements with no electrodes/leads, silicone-rubber leads, and copper leads with 5 kΩ resistors. The silicone-rubber leads were directed out of the scanner in the inferior direction as suggested for MRCDI experiments and seen in figure 3a. The copper leads were positioned as seen in figure 1a.

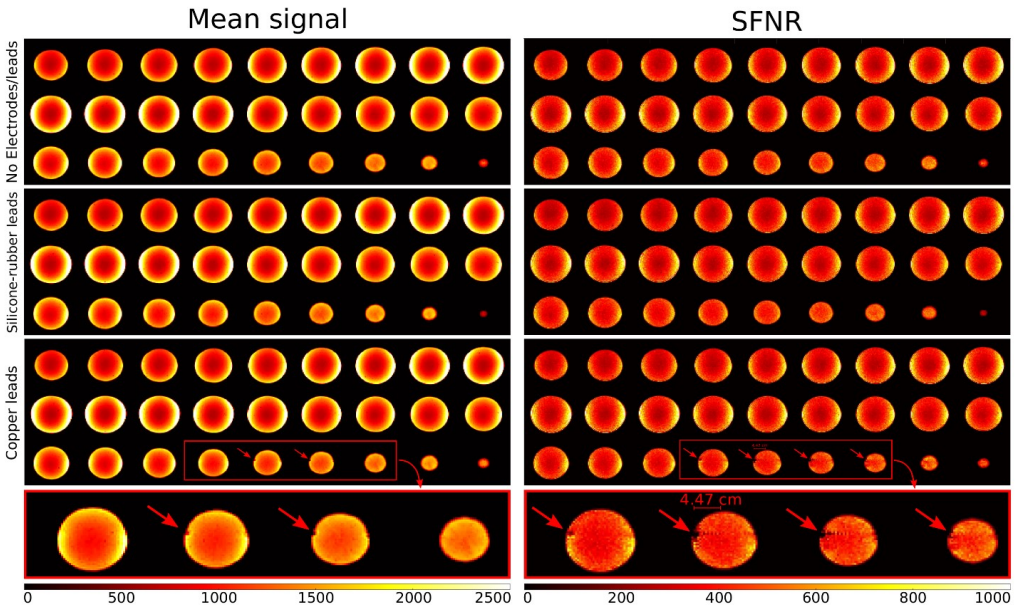

Figure S1.2: Temporal mean signal (left) and SFNR (right) for no electrodes/leads (top), silicone-rubber leads (middle), and copper leads with safety resistors (bottom). The cutout at the bottom shows the slices where the copper leads have negative effect on the measured data.

The results are presented in figure S1.2. There is no difference between mean signal and SFNR for silicone rubber leads and no electrodes/leads. For the copper leads, there are a few slices where a small signal loss can be seen in the mean signal. The artifact is much clearer in the SFNR images and extends considerably into the phantom. The 4.47 cm indicated at the bottom left is only the size of the artifact. The distance to the lead/resistor is about 0.5 cm further due to the shell of the phantom.

S2. Coil model validation

The coil models used for the RF simulations have been validated by comparing simulated B_1^+ fields to measured B_1^+ fields [7]. The sequence and parameters used for B_1^+ mapping at 3T are the same as in section S1. A 3D gradient echo dual TR B_1^+ mapping sequence was used at 7T [8] with 5.3×5.3 mm^2 in-plane resolution.

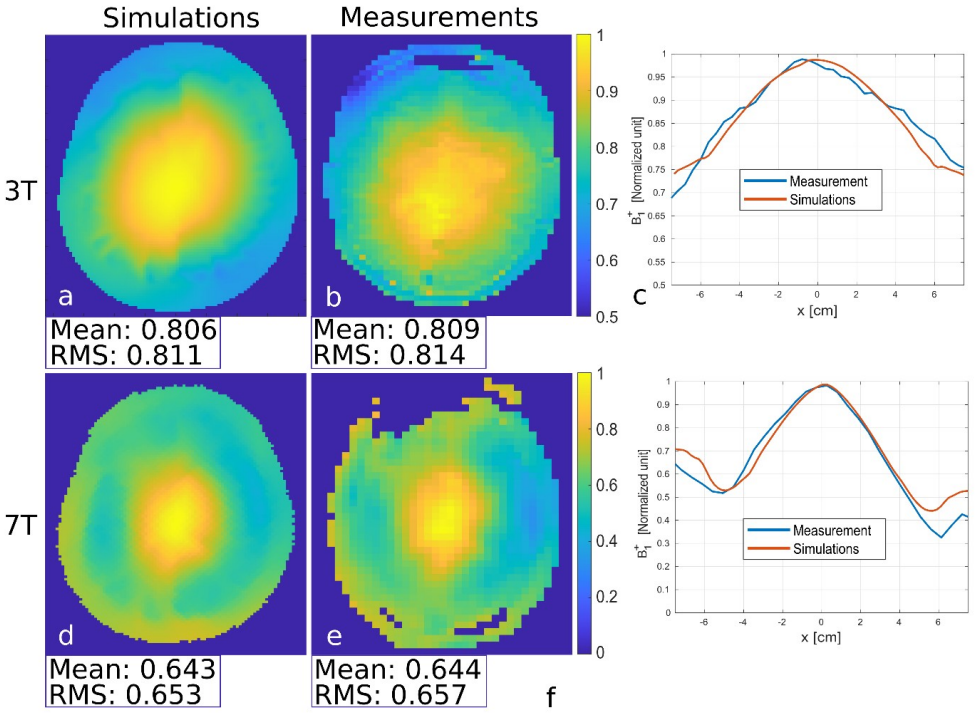

Figure S2: Simulated (a,d) and measured (b,e) B_1^+ at 3T and 7T, respectively. c,f) Right-left projection through the centre of the B_1^+ maps. The mean and RMS values shown in the figure are used as a quantitative measure of the similarities of the B_1^+ maps.

Qualitatively the simulated and measured fields have the same spatial distributions including slight right-left asymmetries (Figure S2), despite the subjects not being identical (the circularly polarized RF field breaks the symmetry). Figure S2c and S2f are projections through the center of the images. There is also a good agreement for the quantitative comparisons of mean and RMS values of the B_1^+ maps as displayed in Figure S2.

References

[1] Göksu C, Scheffler K, Siebner HR, Thielscher A, Hanson LG. The stray magnetic fields in Magnetic Resonance Current Density Imaging (MRCDI). Phys Medica 2019;59:142–50. https://doi.org/10.1016/j.ejmp.2019.02.022.

[2] Grodzki DM, Jakob PM, Heismann B. Ultrashort Echo Time Imaging Using Pointwise Encoding Time Reduction With Radial Acquisition (PETRA) 2012;518:510–8. https://doi.org/10.1002/mrm.23017.

[3] Rorden C, Brett M. Stereotaxic display of brain lesions. Behav Neurol 2000;12:191–200. https://doi.org/10.1155/2000/421719.

[4] Chung S, Kim D, Breton E, Axel L. Rapid B1+ mapping using a preconditioning RF pulse with turboFLASH readout. Magn Reson Med 2010;64:439–46. https://doi.org/10.1002/mrm.22423.

[5] Friedman L, Glover GH. Report on a multicenter fMRI quality assurance protocol. J Magn Reson Imaging 2006;23:827–39. https://doi.org/10.1002/jmri.20583.

[6] Glover GH, Mueller BA, Turner JA, Van Erp TGM, Liu TT, Greve DN, et al. Function biomedical informatics research network recommendations for prospective multicenter functional MRI studies. J Magn Reson Imaging 2012;36:39–54. https://doi.org/10.1002/jmri.23572.

[7] Van Den Berg CAT, Bartels LW, Van Den Bergen B, Kroeze H, De Leeuw AAC, Van De Kamer JB, et al. The use of MR B1+ imaging for validation of FDTD electromagnetic simulations of

human anatomies. Phys Med Biol 2006;51:4735–46. https://doi.org/10.1088/0031-9155/51/19/001.

[8] Yarnykh VL. Actual flip-angle imaging in the pulsed steady state: A method for rapid three-dimensional mapping of the transmitted radiofrequency field. Magn Reson Med 2007;57:192–200. https://doi.org/10.1002/mrm.21120.

APPENDIX C

Safety evaluation with respect to RF-induced heating of a new setup for transcranial electric stimulation during MRI

The following abstract was presented at ISMRM & SMRT Annual Meeting & Exhibition, 2021.

Safety evaluation with respect to RF-induced heating of a new setup for transcranial electric stimulation during MRI

Fróði Gregersen[1,2,3,8], Cihan Göksu[2,4], Gregor Schaefers[5,6], Rong Xue[7,8,9], Axel Thielscher[1,2] and Lars G. Hanson[1,2]

[1] Section for Magnetic Resonance, DTU Health Tech, Technical University of Denmark, Kgs Lyngby, Denmark
[2] Danish Research Centre for Magnetic Resonance, Centre for Functional and Diagnostic Imaging and Research, Copenhagen University Hospital, Amager and Hvidovre, Denmark
[3] Sino-Danish Center for Education and Research, Aarhus, Denmark
[4] High-Field Magnetic Resonance Center, Max-Planck-Institute for Biological Cybernetics, Tübingen, Germany
[5] MRI-STaR-Magnetic Resonance Institute for Safety, Technology and Research GmbH, Gelsenkirchen, Germany
[6] MR:comp GmbH, MR Safety Testing Laboratory, Gelsenkirchen, Germany
[7] State Key Laboratory of Brain and Cognitive Science, Beijing MRI Center for Brain Research, Institute of Biophysics, Chinese Academy of Sciences, Beijing 100101, China
[8] University of Chinese Academic of Sciences, Beijing 100049, China
[9] Beijing Institute for Brain Disorders, Beijing 100053, China

Synopsis (100 words):

Combining transcranial electrical stimulation (TES) with MRI offers various interesting research opportunities, but also introduces safety concerns. Coupling between the RF field and highly conductive TES leads can lead to skin burns. These safety issues are usually mitigated with the use of safety resistors and controlled lead paths that reduce the power absorbed by the leads. However, these methods introduce practical limitations for combined TES/MRI experiments, such as limited stimulation currents and cable stray fields corrupting MR current density imaging. We overcome these limitations by using low-conductivity silicone-rubber as TES leads. Simulations and temperature measurements are used for safety assessment.

Abstract (850 words)

Introduction: In recent years, there has been a growing interest in combined MRI and transcranial electric stimulation (TES) experiments such as TES/fMRI studies for neuroscientific research and MR current density imaging (MRCDI) to map the injected currents with MRI. Extra safety measures have to be taken when introducing high-conductivity lead wires into the MR environment[1]. For specific resonance conditions, coupling between the RF field of the scanner and the current injection setup can result in burns of the subject's scalp. For the TES device most commonly used in combination with MRI (DC-STIMULATOR MR, neuroCare Group GmbH, München, Germany) the safety issues are addressed by using 5 kΩ safety resistors to shorten the highly conductive path of the leads near the head. With 30 V supply, the stimulation current is limited to under 3 mA. Additionally, the twisted leads have to exit the head coil as seen in fig. 1a. This restricts lead configuration, which is a problem for MRCDI experiments as stray magnetic fields from the leads are detrimental when measuring fields from currents inside the brain[2].

The aim of this work was to design new lead wires with flexible lead configurations and higher maximum currents while focusing on MR safety. Additionally, we wanted the leads to be safe at both 3T and 7T, whereas the currently available systems are not approved for 7T.

Methods: To avoid the possibility of high-amplitude standing waves we constructed new leads from carbon-doped silicone-rubber with a conductivity of 29.4 S/m (ELASTOSIL® R 570/60 RUSS, Wacker, Munich, Germany). The silicone-rubber is routinely used in the MR environment as surface electrodes for TES. We constructed two electrode types, namely circular and center-surround as seen in fig. 1b-c. The leads are 90 cm long and their cross-sectional area is 10 mm^2. The resistance of each lead wire is 2 kΩ ± 200 Ω.

Finite-difference time-domain (FDTD) simulations were performed in Sim4Life (ZMT, Zurich, Switzerland) for safety evaluations of the electrode and leads. The body model Duke from the IT'IS foundation was used in the simulations[3]. We first investigated the relationship between the conductivity of the leads and the severity of the resonant 'antenna effect', where standing waves caused by the RF field are formed on leads with specific lengths. These simulations were performed at 298 MHz (proton Larmor frequency at 7T). The setup is shown in fig. 2a with the high-pass birdcage head coil used for 298 MHz simulations (7T volume T/R, Nova Medical, Wilmington, MA). To find the resonance length, the lead length was varied from 0 cm to 100 cm with 10 cm increments including 25 cm and 75 cm. Simulations were also performed with the worst-case length (25 cm) with varying lead conductivity. The severity of the 'antenna effect' was assessed by evaluating the power loss on the electrodes.

We also simulated the realistic lead configurations as shown in fig. 2b-e. This was both done at 298 MHz and 128 MHz (proton Larmor frequency at 3T). A generic body coil was used for simulations at 128 MHz (shown in fig. 2d-e). The specific absorption rate (SAR) was obtained from the FDTD simulations. Following the international guidelines IEC 60601-2-33[4] we evaluated the influence the electrodes and leads have on SAR by comparing head SAR and 1 g local head SAR for a reference simulation with simulations including electrodes and leads. We also performed temperature measurements with high SAR sequences to ensure compliance with international guidelines[4].

Results and discussions: The worst-case 'antenna effect' was found for ¼ RF wavelength corresponding to 25 cm in air for 298 MHz simulations (fig. 3a). This is in agreement with previous experimental data[5]. The antenna effect is often believed to occur at integer multiples of ½ RF wavelength, but this depends on the boundary condition of the leads[5]. In fig 3b for varying conductivities at the worst-case length, it is clear that the antenna effect is eliminated for silicone-rubber.

The electrodes/leads have some influence on the distribution of local SAR levels (fig. 3c), but the peak 1 g local head SAR is always in the same location as for the reference simulations. The results for each electrode type and lead configuration as shown in fig. 2b-

e is presented in table 1. R_m and R_{1g} are the ratios of head SAR and peak 1 g local head SAR for a given simulation to reference simulation. Only minimal SAR changes are observed both before and after normalization of the B_1 fields.

Results from temperature measurements are shown in table 2 with one example shown in fig. 3d. The numbers on the electrodes in fig. 3d indicate the positions given in table 2. More heating was observed for the center-surround electrodes, although there was no difference when the leads were attached. No heating above the guidelines of 39 °C was observed[4].

Conclusion: We have overcome the limitations of the commercial TES/MRI equipment by using low-conductive silicone-rubber. The elimination of the antenna effect allows for more flexible lead configurations and the lower overall impedance increases the maximum allowed stimulation current. Additionally, we have shown that the setup can safely be used at both 3T and 7T.

Acknowledgments: This study was supported by the Lundbeck Foundation (grants R313-2019-622 and R244-2017-196 to AT), the Chinese National Major Scientific Equipment R&D Project (grant ZDYZ2010-2), and a PhD stipend of the Sino-Danish Center for Education and Research to FG. The authors thank Zuo Zhentao, Hasan Hüseyin Eroğlu, Vincent Boer, and Esben Thade Pedersen for kind technical help.

References:

1. Panych LP, Madore B. The physics of MRI safety. *J Magn Reson Imaging*. 2018;47(1):28-43. doi:10.1002/jmri.25761
2. Göksu C, Scheffler K, Siebner HR, Thielscher A, Hanson LG. The stray magnetic fields in Magnetic Resonance Current Density Imaging (MRCDI). *Phys Medica*. 2019;59(February):142-150. doi:10.1016/j.ejmp.2019.02.022
3. Gosselin MC, Neufeld E, Moser H, et al. Development of a new generation of high-resolution anatomical models for medical device evaluation: The Virtual Population 3.0. *Phys Med Biol*. 2014;59(18):5287-5303. doi:10.1088/0031-9155/59/18/5287
4. IEC. Particular requirements for the basic safety and essential performance of magnetic resonance equipment for medical diagnosis. IEC 60601-2-33. 2010.
5. Balasubramanian M, Wells WM, Ives JR, Britz P, Mulkern R V., Orbach DB. RF Heating of Gold Cup and Conductive Plastic Electrodes during Simultaneous EEG and MRI. *Neurodiagn J*. 2017;57(1):69-83. doi:10.1080/21646821.2017.1256722

Summary of main findings (250 Characters. Approx. 35 words):

Using low-conductive silicone rubber as TES leads inside the MR scanner reduces safety issues by eliminating the ‘antenna effect’. This allows for higher stimulation currents and lead configurations optimal for MRCDI.

Figures and tables

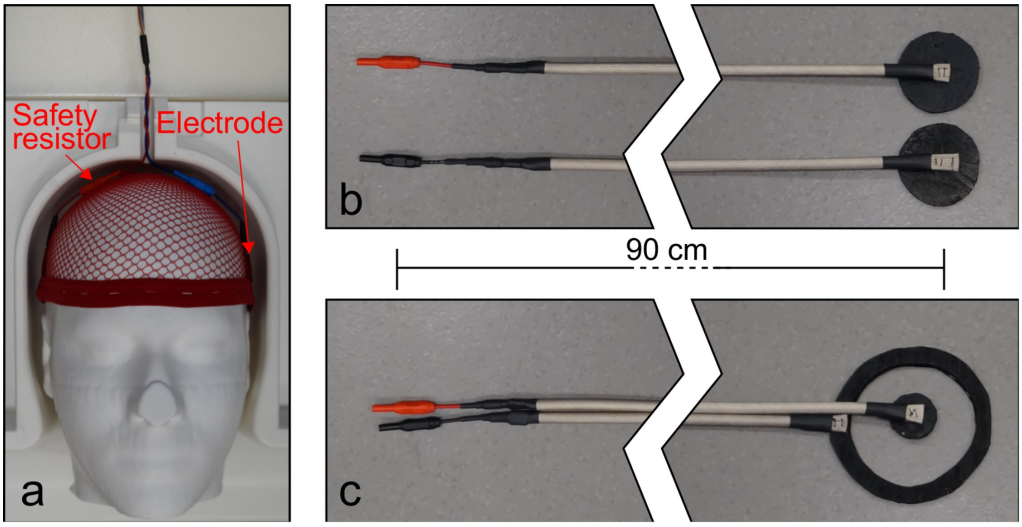

Figure 1: a) Commercially available TES/MRI setup with copper leads and 5 kΩ safety resistors. Leading the wires through the opening in the coil and using twisted pair cables restricts the lead configuration and causes stray fields compromising MRCDI experiments. b) and c) show the proposed electrodes and the lead design. Low-conductivity silicone-rubber is used for electrodes and leads thermally and electrically shielded with a glass fiber sleeving. Medical grade touch-proof MC connectors are used to connect the electrodes to copper lead wires 90 cm away from the subject's head.

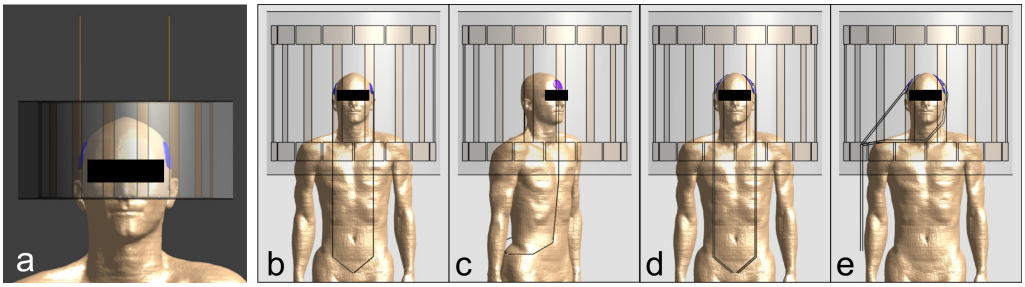

Figure 2: a) Coil model for 298 MHz simulations with electrodes and straight leads to investigate the relationship between the antenna effect and conductivity. b-e) Four lead configurations were simulated for both field strengths. Right-left (b) and anterior-posterior (c) montages for the circular electrodes were simulated with straight leads centered in the coil to reduce stray fields for MRCDI. For the center-surround electrodes, right-left montage with the intended lead configuration (d) was simulated as well as leads closer to the coil (e), where the E-field is higher.

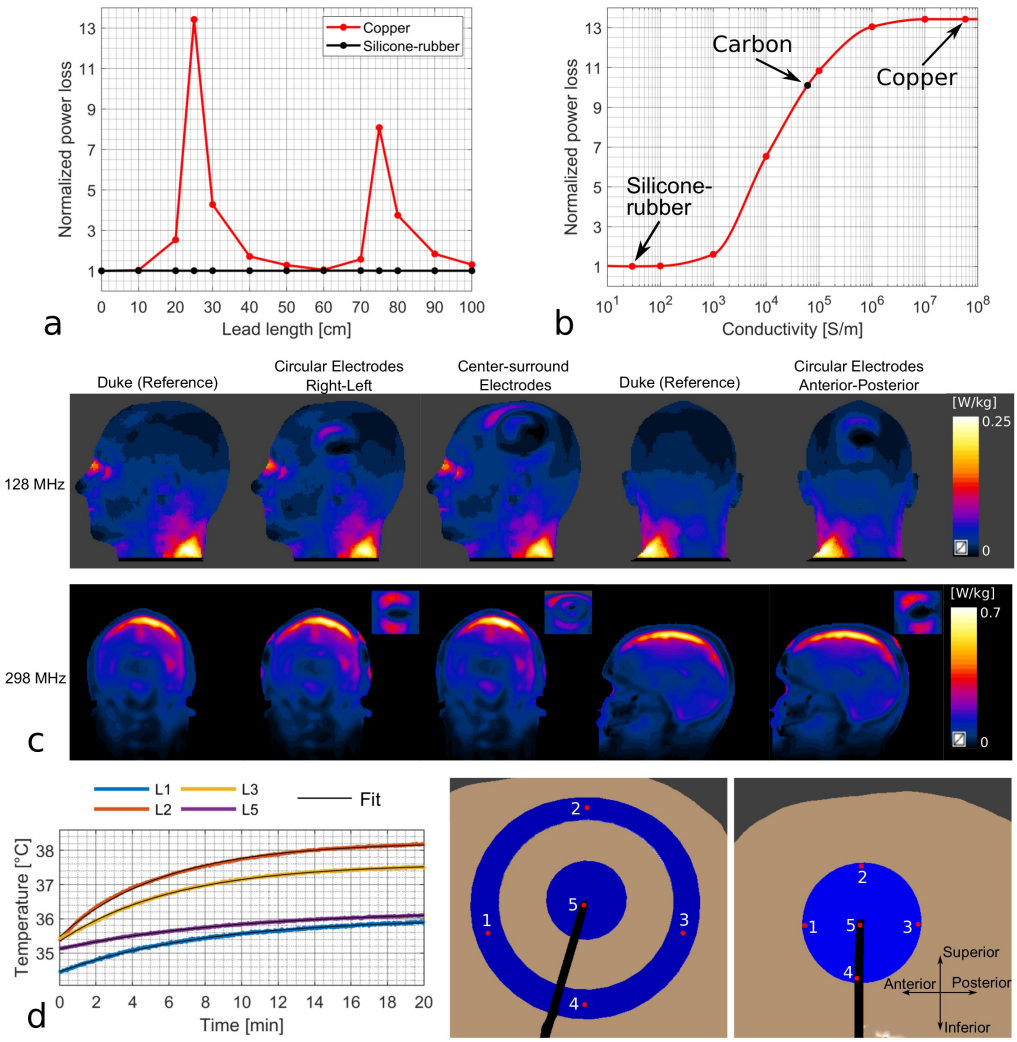

Figure 3: a) Power loss on electrodes vs lead length for antenna effect simulations seen in Figure 2a for copper and silicone-rubber, respectively. b) Power loss on electrodes vs conductivity at worst-case lead length. c) 1 g average local head SAR for simulations at 128 MHz (top) and 298 MHz (bottom). d) Temperature measurement for center-surround electrodes with center leads (Figure 3c). L in the legend indicates that it is a measurement on the left electrode. The numbers on the electrodes indicate the probe position referred to in table 2.

Frequency	Electrodes	Setup	Normalized to 1 W input			Normalized to $\|B_1\|$	
			R_m	R_{1g}	$\|B_1^{ref}\|/\|B_1\|$	R_m	R_{1g}
128 MHz	Circular	Without leads	1.02	0.96	0.99	0.99	0.94
	Right-left	With leads	0.99	0.94	0.99	0.97	0.93
	Circular	Without leads	1.02	1.00	0.99	1.00	0.98
	Anterior-posterior	With leads	0.96	0.93	1.02	1.01	0.98
	Center-surround	Without leads	1.01	0.94	1.01	1.02	0.95
		Center leads	0.97	0.86	1.02	1.01	0.90
		Off-center leads	0.94	0.91	1.06	1.04	1.01
298 MHz	Circular	Without leads	1.00	1.00	1.01	1.03	1.02
	Right-left	With leads	0.98	1.00	1.02	1.02	1.04
	Circular	Without leads	1.00	0.97	1.00	1.00	0.98
	Anterior-posterior	With leads	0.98	0.98	1.01	1.00	0.99
	Center-surround	Without leads	0.93	0.96	1.09	1.10	1.13
		Center leads	0.90	0.96	1.09	1.07	1.14
		Off-center leads	0.89	0.95	1.10	1.07	1.15

Table 1. Head SAR and local head SAR (1 g average) ratios (R_m and R_{1g}) for both field strengths and all simulated electrode montages compared to reference simulations. SAR is given for 1 W input power as well as normalized for the B_1 field in the center slice of the coil. The ratio between $|B_1^{ref}|$ and $|B_1|$ for the corresponding simulation is used for normalization. All local head SAR maxima were at the same location as for the reference simulation.

B_0	Electrodes	Setup	Sequence	Probe positions	Steady state temperature
3T	Circular	Right-left	RARE	[Ref L1 R3 L5]	[35.2 35.4 35.8 36.2]
		Anterior-posterior	RARE	[Ref A4 P2 P4]	[35.0 36.3 37.2 37.6]
	Center-surround	Without leads	RARE	[Ref L4 R2 L2]	[35.6 35.7 36.3 36.6]
				[L1 L5 L3 L2]	[35.9 36.4 37.2 38.4]
				[L1 L5 L3 L2]	[35.5 35.8 37.7 38.5]
		On-center leads	RARE	[Ref L4 L2 R2]	[35.6 36.2 37.2 37.2]
				[Ref L2 R2 L4]	[34.8 36.4 37.0 37.9]*
				[L1 L5 L3 L2]	[36.4 36.7 37.5 37.6]
				[L1 L5 L3 L2]	[36.0 36.2 37.6 38.2]**
		On-center leads	pCASL	[Ref L2 R2 L4]	[34.6 35.8 36.2 36.8]*
		Off-center leads	RARE	[Ref L4 L2 R2]	[35.4 36.2 37.0 37.3]
7T	Circular	Anterior-posterior	RARE	[A4 Ref P4 P2]	[34.9 35.3 35.7 35.9]
	Center-surround	On-center leads	RARE	[R2 L2 Ref L4]	[34.3 35.1 35.4 36.0]

Table 2. Modeled steady state temperature from all measurements. The numbers for the positions are indicated in fig. 3d and L, R, A and P refer to electrode position (left, right, anterior and posterior). Ref is the reference probe on top of the head. For the RARE sequence**,** the SAR was approximately 100% of the tolerable level reported by the scanner and for pCASL, it was approximately 50%, varying slightly with subjects. The asterisks (*) indicate the same scan sessions for a RARE and pCASL sequence. The double asterisks (**) indicate the data shown in fig. 3d.

{2.7182818284}ϑφέρτυθιοπσδφγηξκλ